Carnegie Mellon University
CARNEGIE INSTITUTE OF TECHNOLOGY

THESIS

Submitted in Partial Fulfillment of the Requirements
For the Degree of Doctor of Philosophy

TITLE

THERMAL TRANSPORT BY PHONONS ACROSS SEMICONDUCTOR INTERFACES, THIN FILMS, AND SUPERLATTICES

PRESENTED BY

ERIC SCOTT LANDRY

ACCEPTED BY THE DEPARTMENT OF MECHANICAL ENGINEERING

MAJOR PROFESSOR   DATE

DEPARTMENT HEAD   DATE

APPROVED BY THE COLLEGE COUNCIL

DEAN   DATE

THERMAL TRANSPORT BY PHONONS ACROSS SEMICONDUCTOR INTERFACES, THIN FILMS, AND SUPERLATTICES

by

Eric Scott Landry

A dissertation submitted in partial fulfillment
of the requirements for the degree of
Doctor of Philosophy
in Mechanical Engineering

Carnegie Mellon University
2009

Doctoral Committee:

Assistant Professor Alan McGaughey (Chair), Mechanical Engineering
Professor Shi-Chune Yao, Mechanical Engineering
Professor Sara Majetich, Physics
Dr. Marcela Madrid, Pittsburgh Supercomputing Center

ABSTRACT

THERMAL TRANSPORT BY PHONONS ACROSS SEMICONDUCTOR
INTERFACES, THIN FILMS, AND SUPERLATTICES

by
Eric Scott Landry

Chair: Alan McGaughey

Advanced technological devices often contain a high density of semiconductor interfaces. Phonon scattering at these interfaces impedes thermal transport through the device and can adversely affect performance and reliability. To improve device design, accurate phonon transport models are needed. Such models will also allow improvements in the design of semiconductor superlattices (periodic nanostructures containing thin films of alternating species) for thermoelectric energy conversion applications. In this thesis, thermal transport by phonons across silicon- and germanium-based interfaces, thin films, and superlattices is studied using molecular dynamics (MD) simulation and lattice dynamics (LD) calculations.

Insight into the phonon transport across interfaces and thin films is gained by comparing MD-predicted thermal resistances to values calculated theoretically using LD-predicted phonon properties. Using this approach, the phonon distributions on either side of an interface are inferred to deviate from their bulk values. For interfaces with large species mismatch, however, the phonon distributions are well-approximated

by the equilibrium distribution. Two regimes for the thickness-dependence of the thin film thermal resistance are identified. For films with thicknesses less than $\sim$2 nm, the thermal resistance is affected by changes in the allowed vibrational states in the film. For thicker films, the thermal resistance is affected by the presence of phonon-phonon scattering in the film.

The effect of interfacial species mixing on the thermal conductivity of semiconductor superlattices and the link between the superlattice unit cell design and the thermal conductivity are then explored. Adding species mixing to an otherwise perfectly periodic superlattice removes the phonon coherence, which reduces the thermal conductivity and alters its dependence on period length. For a model superlattice system, a new class of unit cell design is found to yield significant reductions (17%) in the thermal conductivity compared to the minimum value predicted for traditional designs containing two layers in the unit cell. The low thermal conductivities are attributed to reductions in both the phonon group velocities and mean free paths in the regime where the phonon transport has both coherent and incoherent qualities.

ACKNOWLEDGEMENTS

I have been blessed with a tremendous amount of love and support from my entire extended family over the past four years. My parents, however, have played the largest role in putting me on the path towards this goal. My father, who is also a mechanical engineer, certainly influenced me to pursue engineering. The little exercises he used to give me as a kid helped me develop a love of math and science, which is a good thing to have in this field. My mother instilled in me a sense of confidence and work ethic that has proved invaluable. I am also very appreciative for all the encouragement from my brother and sister, my grandparents, and my many aunts, uncles, and cousins back home.

I am also grateful for the support of my Maloney and UConn buddies. Not everyone is lucky enough to have a group of friends (and a brother) who will rent a van, drive the eight hours from Connecticut to Pittsburgh, and spend most of the weekend helping me and Lindsay move into a new apartment. I truly think of each of those guys as brothers. Thanks also to my Pittsburgh friends, most notably, Evan Mosier, for helping me wind down on the weekends.

My interest in nanoscale heat transfer was sparked by my thesis advisor, Professor Alan McGaughey. I am still thankful that he contacted me about becoming a member of his, at the time, nonexistent lab group. Despite being Alan's first graduate student, I did not suffer from any learning curve - he was an excellent advisor from day one.

In addition to teaching me a thing or two about phonons, Alan opened my eyes to some terrific Canadian rock music.

I have also benefitted from intellectually stimulating discussions with the other members of the, now larger, Nanoscale Transport Phenomena Laboratory, in particular: John Thomas, Minyoung Lee, and Joe Turney. Special thanks to John for always being a great person to chat about random news stories and share some laughs with over the years.

I would also like to thank Professor Shi-Chune Yao, Professor Sara Majetich, and Dr. Marcela Madrid for serving on my thesis committee and Professor Mahmoud Hussein for his guidance on the work presented in Chapter VII of this thesis.

Finally, Lindsay Hanna deserves more credit than anyone for helping me get to graduation with my sanity intact. I was fortunate enough to meet Lindsay, who is now my fiancée, in the first few weeks of graduate school. She is also finishing her Ph.D. in mechanical engineering this semester, and it's truly been wonderful having her to share the graduate school experience with. I look forward to the many years to come. Thanks are also due to Lindsay's awesome family for their continual support, and the late, great Dakota Hanna for listening to me practice so many presentations, always with a wagging tail.

TABLE OF CONTENTS

LIST OF TABLES

LIST OF FIGURES

NOMENCLATURE

a, $\mathbf{a}$	lattice constant, translational vector
A	constant, LJ species
B	constant, LJ species
c	cutoff
c_{ph}	volumetric specific heat per phonon mode
C_{11}, C_{44}	elastic constants
C_v	volumetric specific heat
D	interface thickness
$\mathbf{D}$, $\tilde{\mathbf{D}}$	dynamical matrix
e	atomic energy (kinetic and potential)
$\mathbf{e}$, $\tilde{\mathbf{e}}$	phonon polarization vector
E	total system energy (kinetic and potential)
ΔE_k	change in kinetic energy
f	phonon distribution function
f'	deviation from equilibrium phonon distribution function
$\mathbf{F}$	force vector
g_ω, g_θ	frequency- and angular-dependence of the thermal conductance
G	thermal conductance

$\hbar$	Planck constant divided by 2π
i	atomic index
$\mathbf{I}$	identity matrix
j	atomic index
k	thermal conductivity, atomic index, unit cell index
k_{B}	Boltzmann constant
l	direction, nondimensional length, atomic index
L	length, period length, layer thickness
$\mathcal{L}$	amplitude of excited mode in left lead
m	mass
m_R	mass ratio
n	number of atoms in unit cell
n_v	number density (N/V)
N	number of atoms in system, number of excited modes
N_{sim}	number of simulations
N_{uc}	number of unit cells
p	constant, junction unit cell index
$\mathbf{p}$	momentum vector
P	pressure
q	heat flux, constant
$\tilde{Q}, Q$	normal mode coordinate, normal mode amplitude
$\mathbf{r}, \mathbf{r}_o$	instantaneous position vector, equilibrium position vector
$\mathbf{r}^i_j, \mathbf{r}^i_{j,o}$	separation vectors $[\mathbf{r}^i_j = \mathbf{r}(i) - \mathbf{r}(j), \mathbf{r}^i_{j,o} = \mathbf{r}_o(i) - \mathbf{r}_o(j)]$
r^i_j	magnitude of $\mathbf{r}^i_j$

R	thermal boundary resistance, thin film thermal resistance
$\mathcal{R}$	amplitude of excited mode in right lead
S	Seebeck coefficient
$\mathbf{S}$, S_l	heat current vector, lth component of $\mathbf{S}$
Δt	time step
t	time, thickness
T, $\bar{T}$, ΔT	temperature, average temperature, temperature drop
$\mathbf{u}$	time-dependent displacement vector
$\boldsymbol{u}$	displacement vector
$\mathbf{U}$	displacement vector (relative to other atoms in the unit cell)
U_l	lth component of $\mathbf{U}$
$\mathbf{v}$	velocity vector
v_{ac}	representative acoustic phonon group velocity
$\mathbf{v}_g$, $v_{g,l}$	phonon group velocity vector, lth component of $\mathbf{v}_g$
v_2, v_3	two- and three-body terms in the SW potential
V	volume
x	fraction of Ge atoms or species B atoms in sample
y	normalized separation distance
ZT	thermoelectric figure of merit

Greek symbols

α	phonon transmission coefficient
β	Cartesian coordinate, fraction of heat carried by phonon mode
γ	constant
δ	Kronecker delta function

ϵ	energy scale
θ	dihedral angle, phonon incidence angle, inclination angle
$\boldsymbol{\kappa}$, κ, κ_l	phonon wave vector, wave number, lth component of $\boldsymbol{\kappa}$
λ	constant
λ_l	lth component of phonon mode-dependent mean free path
Λ	mode-averaged phonon mean free path
ν	phonon polarization
ρ	density, phonon reflection coefficient
ς	eigenvalue
σ	electrical conductivity, length scale
τ	phonon relaxation time, time period in MD simulation
ϕ	potential energy between two atoms in LJ potential, azimuth angle
Φ	total system potential energy
χ	function for the inverse of the thermal conductivity
$\boldsymbol{\Psi}$	second-order force constant matrix
ω, $\Delta\omega$	phonon frequency, width of frequency bin
Ω	primitive unit cell volume

Subscripts

ac	acoustic
BE	Bose-Einstein
$corr$	correlation
$crit$	critical
dc	data collection

eq	equilibrium
E	equilibrium
F	film
i	atomic index
j	atomic index
k	atomic index
L	left lead, longitudinal
NE	nonequilibrium
res	reservoir
R	right lead
ss	steady-state
S	sample
T	transverse
∞	bulk property
$\parallel$	parallel
$\perp$	perpendicular

Superscripts

DM	direct method
est	estimate
GK	Green-Kubo
I	property of incident mode
L	property of excited mode in left lead
max	maximum

R	property of excited mode in right lead
T	transpose
†	conjugate transpose

Abbreviations

AMM	acoustic mismatch model
BTE	Boltzmann transport equation
CMOS	complementary metal-oxide-semiconductor
CP	cross-plane
DL	diffusive limit
DMM	diffuse mismatch model
HCACF	heat current autocorrelation function
HS	high scatter limit
IP	in-plane
LA	longitudinal acoustic
LD	lattice dynamics
LJ	Lennard-Jones
MD	molecular dynamics
ML	monolayer
PDOS	phonon density of states
SL	superlattice
SW	Stillinger-Weber
TA	transverse acoustic
UC	conventional unit cell

CHAPTER I

Introduction

1.1   Motivation

Semiconductor interfaces and thin films are pervasive in advanced technological devices. For example, the active region in a quantum cascade laser or a light-emitting diode contains films of direct bandgap semiconductors such as GaAs, AlGaAs, and GaN with thicknesses of 1-10 nm [1–3]. The amorphous SiO_2 dielectric layer in a field effect transistor can be as thin as 1 nm [see Fig. 1.1(a)], and the gate length in a complementary metal-oxide-semiconductor (CMOS) transistor is $\sim$10 nm [4–6]. Because thermal transport in semiconductors is dominated by phonons (i.e., quantized lattice vibrations) with bulk mean free paths that exceed these film thicknesses, the phonon transport is significantly impeded due to scattering at the high density of material interfaces [5, 7, 8].[1] This impediment, which is quantified by the thermal boundary resistance, can lead to thermal management challenges due to its adverse effect on device performance and reliability [6, 9–12].

In some applications, however, the impediment of the thermal transport resulting from phonon scattering at semiconductor interfaces is desirable. This effect is used, for example, to improve the effectiveness of thermoelectric materials, and thus, increase the efficiency of thermoelectric energy conversion devices. The effectiveness of a

---

[1]The average phonon mean free path in bulk Si at room temperature has been estimated to be 300 nm [7].
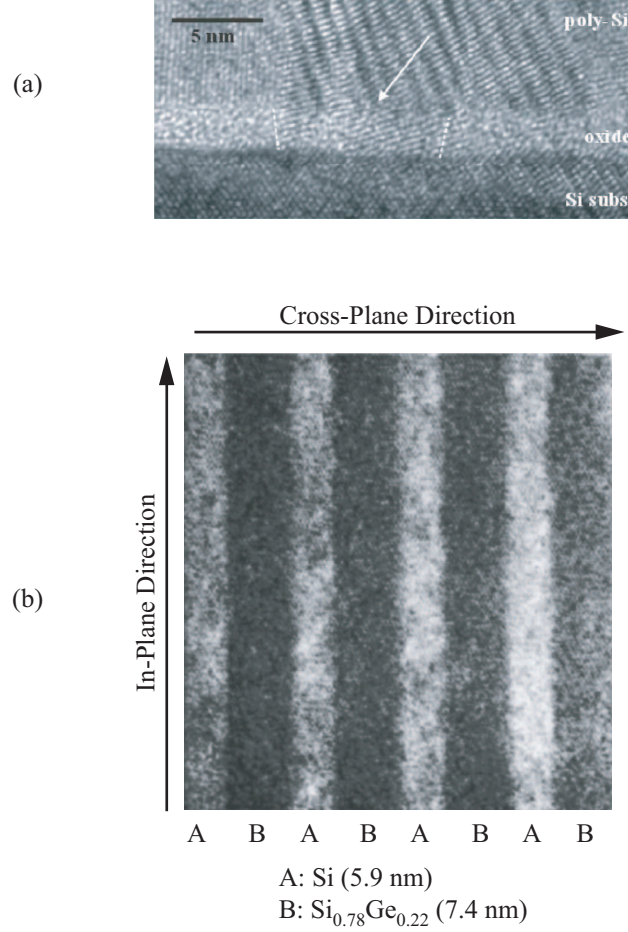
Figure 1.1: (a) Transmission electron microscope (TEM) image of a thin amorphous SiO_2 layer confined by polycrystalline Si and a Si substrate. Reprinted with permission from Ref. [4], Copyright 2005 American Institute of Physics. (b) TEM image of a $Si/Si_{0.78}Ge_{0.22}$ superlattice. Note the definitions of the in-plane and cross-plane directions. Reprinted with permission from Ref. [13], Copyright 2005 American Institute of Physics.

thermoelectric material is quantified by the thermoelectric figure of merit, ZT, which is defined as [14–18]

$$ZT = \frac{S^2 \sigma T}{k}, \tag{1.1}$$

where S, σ, T, and k are the Seebeck coefficient, electrical conductivity, temperature, and thermal conductivity. The best commercially available thermoelectric materials are heavily doped Bi_2Te_3 and $Si_{1-x}Ge_x$ alloys, which have $ZT \approx 1$ at their optimal operating temperature [14, 19]. Materials with $ZT > 4$, however, are required for the

efficiencies of thermoelectric energy conversion devices to be comparable to those associated with traditional energy conversion technologies [20]. As a result, these devices are only used in niche applications (e.g., temperature stabilization in semiconductor lasers and power generation in deep space satellites), despite their high reliability and efficiencies that do not degrade with decreasing device size [18]. Increases in ZT have been realized in semiconductor superlattices, which are periodic nanostructures that contain films of alternating species with thicknesses as small as 1 nm [see Fig. 1.1(b)]. Because the average mean free path of the phonons in a semiconductor exceeds that of the charge carriers, phonon scattering at the internal superlattice interfaces can lead to low cross-plane thermal conductivity without significantly degrading the power factor, $S^2\sigma$. In addition, wave interference between the phonons in a superlattice can lead to reductions in the average phonon group velocity, and thus, low thermal conductivity. These effects have increased the state of the art of ZT at room temperature to $ZT = 2.4$, which is observed for Bi_2Te_3/Sb_2Te_3 superlattices [21]. With further increases in ZT, thermoelectric energy conversion devices may see additional applications in waste heat recovery and solar energy conversion [14, 15, 22–24].

To aid engineers in both alleviating the thermal management challenges associated with high interface density and designing materials with high ZT, accurate models for thermal transport across semiconductor interfaces, thin films, and superlattices are needed. Standard modeling techniques based on the Fourier law of heat conduction assume that phonon transport is diffusive. This assumption is not valid, however, when the interface separation distance is on the same scale as the phonon mean free paths in the corresponding bulk material. When this is the case, phonons can travel ballistically (i.e., without scattering) between the interfaces, leading to non-negligible phonon-interface scattering [5]. Alternative approaches, such as those rooted in the

Boltzmann transport equation (BTE), can account for the effects of ballistic phonon transport. These approaches, however, require specification of the phonon transport properties (e.g., phonon group velocities, relaxation times, and transmission coefficients) *a priori*, limiting their predictive power.

1.2 Objective and outline of thesis

The objective of this thesis is to develop an understanding of thermal transport across semiconductor interfaces, thin films, and superlattices. This objective will be achieved using molecular dynamics (MD) simulations and lattice dynamics (LD) calculations, two methods that require no *a priori* specification of the phonon properties. The analysis focuses mainly on Si- and Ge-based materials. The emphasis is placed on this material system because Si-based materials with high ZT are especially attractive for application due to established industrial experience in fabricating Si-based devices [25]. The outline of the remainder of the thesis is as follows:

In Chapter II, details related to the MD simulations are discussed. The interatomic potential functions used to model the atomic interactions are defined. The Green-Kubo method and direct method for predicting thermal conductivity and thermal resistance using MD simulation are introduced and a quantitative comparison between superlattice thermal conductivities predicted using both methods is made.

In Chapter III, the theory underlying the LD calculations, which are performed under the harmonic approximation, is discussed. The methodology related to calculating phonon frequencies, polarization vectors, group velocities, and transmission coefficients is provided.

In Chapter IV, the accuracies of two theoretical expressions for thermal boundary resistance are assessed [26]. This assessment is needed because a robust model for

thermal boundary resistance is still unavailable, despite five decades of research. This slow progress is argued to be due to the many sources of uncertainty when comparing theoretical predictions to experimental measurements. The computational methods used in this work allow these uncertainties to be eliminated and an accurate assessment of the underlying theory to be made.

In Chapter V, thermal transport across confined semiconductor thin films is studied [27]. The effects of changes in the allowed vibrational states in the film and the presence of phonon-phonon scattering in the film on the thin film thermal resistance are examined. Previous modeling efforts have assumed that all of the phonons in the film have a mode-independent mean free path. This widely-invoked assumption is shown to lead to erroneous predictions concerning the transition from ballistic to diffusive phonon transport with increasing film thickness.

In Chapter VI, the effect of interfacial species mixing on the thermal conductivity of semiconductor superlattices is predicted [28]. This investigation is needed because models for predicting superlattice thermal conductivity must be able to account for deviations from perfect sample quality, as will be found in realistic superlattices.

In Chapter VII, the link between the superlattice unit cell design and the thermal conductivity is explored [29]. The goal of this exploration is to identify new design concepts with potential for low thermal conductivity, and thus, high ZT. To minimize the required simulation time, this exploration is performed for superlattices with atomic interactions modeled by the Lennard-Jones (LJ) potential. A new class of unit cell designs is found to yield significant thermal conductivity reductions (17%) compared to the thermal conductivities of more traditional superlattices.

In Chapter VIII, the major contributions of the work presented in this thesis and suggestions for future study are discussed.

CHAPTER II

Molecular dynamics simulations

2.1 Overview

Over the past few decades, MD simulation has emerged as powerful tool for modeling material properties and transport phenomena. A small subset of the large array of properties and phenomena that MD simulation has been used to study includes: the thermal conductivities of a variety of bulk and composite solids [30–32], the fracturing of semiconductor nanowires [33], protein folding [34], and supercritical phase change [35]. The main strength of MD simulation is that it allows the observation of a system with atomic-scale resolution, providing a level of detail that is either difficult or impossible to attain in an experiment. With this atomic-scale resolution, a researcher is provided with an opportunity to elucidate the physics underlying macroscopically observable properties and phenomena.

In an MD simulation, the positions and momenta of a set of atoms are allowed to evolve from an initial configuration by numerically integrating Newton's equations of motion, as discussed in Section 2.2. The only required input to an MD simulation is a suitable method for specifying the atomic interactions. Such specification is typically made using empirically-derived interatomic potential functions, which are element-specific and are valid only for a range of atomic configurations similar to those used

during the potential development. In recent years, *ab initio* (e.g., density functional theory)-based approaches have become an attractive alternative to empirical interatomic potential functions because they are valid for all atomic configurations and elements [36,37]. Due to computational expense, however, this approach is only practical for systems containing less than ~100 atoms and simulations with durations less than ~100 ps. Because of these limitations, empirical interatomic potential functions are used throughout this thesis. The interatomic potential functions used in this thesis are discussed in Section 2.4.

There are two limitations of MD simulation that should be noted. First, because the details of the electron positions and momenta are neglected, MD simulation is limited to materials in which the effects of electron transport are negligible. This condition is met in dielectrics and semiconductors because the thermal transport is dominated by phonons [38]. Second, because the system evolves according to Newtonian equations of motion, the atomic dynamics in an MD simulation are strictly classical. While some researchers have applied "quantum corrections" to MD-predicted thermal conductivities [39–42], this approach cannot be justified from a theoretical standpoint [43]. In this thesis, all of the comparisons between MD-predicted and experimentally measured thermal transport properties are thus made at temperatures near or above the Debye temperature, where quantum effects are minimal.

2.2 Integrating Newton's equations of motion

Several algorithms have been developed to numerically integrate the Newtonian equations of motion in an MD simulation, including the velocity Verlet, Verlet leapfrog, and Gear predictor-corrector algorithms [44]. The objective of each algorithm is to predict the atomic positions and momenta at time $t + \Delta t$ based on their values

at time t, while maximizing the value of the time step, Δt, and minimizing numerical error. Here, the velocity Verlet algorithm is used due to its ease of implementation and superior energy conservation compared to the Gear predictor-corrector algorithms with large time steps [44]. With this algorithm, the positions and momenta at time $t + \Delta t$ is found in four steps:

$$\text{Step 1:} \qquad \mathbf{p}(i, t + \Delta t/2) = \mathbf{p}(i, t) + \mathbf{F}(i, t)\Delta t/2 \tag{2.1}$$

$$\text{Step 2:} \qquad \mathbf{r}(i, t + \Delta t) = \mathbf{r}(i, t) + \mathbf{p}(i, t + \Delta t/2)\Delta t/m_i \tag{2.2}$$

$$\text{Step 3:} \qquad \text{Calculate } \mathbf{F}(i, t + \Delta t) \tag{2.3}$$

$$\text{Step 4:} \qquad \mathbf{p}(i, t + \Delta t) = \mathbf{p}(i, t + \Delta t/2) + \mathbf{F}(i, t + \Delta t)\Delta t/2. \tag{2.4}$$

Here, m_i is the mass of atom i, and $\mathbf{r}(i)$ and $\mathbf{p}(i)$ are the position and momentum vectors for atom i. The force acting on atom i, $\mathbf{F}(i)$, is the partial derivative of the total system potential energy, Φ, with respect to the atomic position [45], i.e.,

$$\mathbf{F}(i) = \frac{\partial \Phi}{\partial \mathbf{r}(i)}. \tag{2.5}$$

The derivative of the total system energy is taken analytically using the interatomic potential functions described in Section 2.4.

The value of the time step used in the numerical integration algorithm should be small enough so that the total energy (i.e., kinetic energy and potential energy) of the system, E, is conserved during the simulation to an acceptable level of accuracy. A general rule-of-thumb is to choose the time step such that $1/\Delta t$ is one to two orders-of-magnitude greater than the maximum vibrational frequency in the system. Between Si and Ge, Si has the maximum vibrational frequency of $\sim$20 THz, and a time step of 0.55 fs is used for the Si- and Ge-based materials. This time step leads to fluctuations of the total system energy that are less than 0.001% of the average

value. For the LJ superlattices, the maximum vibrational frequency is an order of magnitude smaller than the maximum frequency in Si, allowing a larger value of the time step of 4.2846 fs to be used.

2.3 NVE, NVT, and NPT ensembles

When the atomic positions and momenta evolve according to Newton's equations of motion, the system is said to be in the NVE ensemble. In this ensemble, the number of atoms, N, the system volume, V, and the total energy, E, are all fixed quantities, while the system temperature and pressure fluctuate about average values. In an MD simulation, it is sometimes desirable to set the average value of the temperature and/or pressure, P (e.g., for calculation of zero-pressure lattice constants). These parameters can be set through the application of thermostats and barostats. For MD simulations run with a thermostat and no barostat, the system is said to be in the NVT ensemble. When both a thermostat and a barostat are applied, the system is said to be in the NPT ensemble.[1] In this thesis, the Nose-Hoover thermostat and Berendsen barostat are used to run simulations in the NVT or NPT ensembles [46,47]. Application of a thermostat or barostat requires modification to the equations of motion. As a result, the total system energy is not conserved in the NVT or NPT ensembles and instead fluctuates about an average value.

2.4 Interatomic potentials

2.4.1 Stillinger-Weber potential

To obtain the force on each atom through Eq. (2.5), an interatomic potential function is required to calculate the total system potential energy. In this thesis, the atomic interactions in the Si- and Ge-based materials are modeled using the Stillinger-

---

[1]The NVE, NVT, and NPT ensembles are also known as the microcanonical, canonical, and grand canonical ensembles.

Table 2.1: Stillinger-Weber energy and length scales for Si-Si, Ge-Ge, and Si-Ge interactions [48–50].

	Si-Si	Ge-Ge	Si-Ge
ϵ_{SW}^{ij} (eV)	2.17000	1.93000	2.04270
σ_{SW}^{ij} (Å)	2.09510	2.18100	2.13805

Weber (SW) potential [48]. In this potential, the total system potential energy is the sum of two- and three-body terms and is given by

$$\Phi = \sum_i \sum_{j>i} v_2(i,j) + \sum_i \sum_j \sum_{k>j} v_3(i,j,k), \tag{2.6}$$

where v_2 and v_3 are functions of the positions and species of atoms i, j, and k [48]. The first term is a summation over all atom pairs, and the second term is a summation over all triplets with atom i at the vertex. The two-body term is

$$v_2(i,j) = \begin{cases} \epsilon_{SW}^{ij} A \left(\dfrac{B}{(y_j^i)^p} - \dfrac{1}{(y_j^i)^q} \right) \exp \left[\dfrac{1}{y_j^i - c} \right], & \text{if } y_j^i < c \\ 0 & \text{otherwise,} \end{cases} \tag{2.7}$$

where A, B, p, and q are constants and c is the nondimensional cutoff radius. The variable y_j^i is a dimensionless pair separation defined as r_j^i/σ_{SW}^{ij}, where $r_j^i = |\mathbf{r}_j^i| = |\mathbf{r}(i) - \mathbf{r}(j)|$. The parameters ϵ_{SW}^{ij} and σ_{SW}^{ij} are the SW energy and length scales for the atomic pair (i,j) and are provided in Table 2.1. The energy and length scales for Si-Si and Ge-Ge interactions were determined by the potential developers by fitting the potential to the crystal cohesive energy and density [48, 49]. Here, the mixing rules described by Laradji *et al.* are used to obtain the length and energy scales for the Si-Ge interactions [50]. The three-body term is

$$v_3(i,j,k) = (\epsilon_{ij}\epsilon_{ik})^{1/2}(\lambda_j \lambda_i^2 \lambda_k)^{1/4} \exp \left[\frac{\gamma}{y_j^i - c} + \frac{\gamma}{y_k^i - c} \right] \left(\cos\theta_{jik} + \frac{1}{3} \right)^2, \tag{2.8}$$

for both $y_j^i < c$ and $y_k^i < c$, and zero otherwise. In Eq. (2.8), θ_{jik} is the angle between atoms i, j, and k with atom i at the vertex, and λ and γ are constants. The constants

A, B, p, q, c, λ, and γ were parameterized for Si by fitting predictions of the radial distribution function and melting temperature to experimental data while ensuring that the crystal structure with the lowest energy is the diamond lattice [48]. For Ge, λ was parameterized by fitting the potential to the zero-temperature elastic constants while all of the other constants were chosen to be the same as the values for Si [49]. The constants in Eqs. (2.7) and (2.8) are $A = 7.049556277$, $B = 0.6022245584$, $p = 4$, $q = 0$, $a = 1.8$, $\gamma = 1.2$, $\lambda_{\text{Si}} = 21.0$, and $\lambda_{\text{Ge}} = 31.0$.

2.4.2 Lennard-Jones potential

For the LJ superlattices and alloys, a truncated LJ 12-6 potential is used to model the atomic interactions. In this potential, the total system energy is equal to a sum of two-body terms, given by

$$\Phi = \sum_i \sum_{j>i} \phi(i,j), \tag{2.9}$$

where

$$\phi(i,j) = \begin{cases} 4\epsilon_{\text{LJ}} \left[\left(\frac{\sigma_{\text{LJ}}}{r_j^i} \right)^{12} - \left(\frac{\sigma_{\text{LJ}}}{r_j^i} \right)^6 \right], & \text{if } r_j^i < 2.5\sigma_{\text{LJ}} \\ 0 & \text{otherwise.} \end{cases} \tag{2.10}$$

Here, ϵ_{LJ} and σ_{LJ} are the LJ energy and length scales, corresponding to the zero-energy pair-separation distance and the potential well depth. The first term in Eq. (2.10) models the strong repulsive interaction between atoms at small separation distances due to the Pauli exclusion principle. The second term models the attractive van der Waals interaction between electrically neutral molecules or atoms. The values of ϵ_{LJ} and σ_{LJ} are chosen to reproduce thermodynamic properties of the gas phase [51,52]. Here, the σ_{LJ} and ϵ_{LJ} values for Ar, 3.40×10^{-10} m and 1.67×10^{-21} J [52], are chosen. The LJ superlattices and alloys are comprised of two species, A and B, that differ

only is mass. The two species have a mass ratio, m_R, of

$$m_R \equiv \frac{m_B}{m_A}. \tag{2.11}$$

In all cases, m_A is equal to the mass of one Ar atom, 6.63×10^{-26} kg. The value of m_B is varied to obtain a desired m_R.

2.4.3 Accuracy of interatomic potentials

The accuracy of any MD-predicted property is limited by the accuracy of the inter-atomic potential function. While the SW potential has been widely used for modeling Si- and Ge-based materials [30, 40, 48, 49, 53–56], it has several deficiencies that will influence its quantitative accuracy for modeling thermal transport. For example, the slopes of the high-symmetry transverse acoustic phonon dispersion branches in SW Si and Ge are too high, leading to over predictions of the phonon group velocities [see Figs. 3.1(a) and 3.1(b)]. In addition, experimental Grüneisen parameters are not well reproduced by the SW potential [57]. These deficiencies are common amongst all of the available interatomic potentials for Si. In light of these deficiencies, in this thesis, MD predictions for the Si- and Ge-based materials are compared to experimental measurements on a qualitative basis. Any quantitative agreement would be fortuitous. The LJ potential is of high accuracy for modeling nobel elements such as Ar. No quantitative comparisons to experiment are made for the LJ superlattices, however, because they are an artificial material used solely to explore qualitative trends.

2.5 Green-Kubo method for predicting thermal conductivity

2.5.1 Definition of the heat current vector

From the time-histories of the atomic positions and momenta obtained from an MD simulation, predictions of material properties can be made. The two most common

MD methods for predicting thermal conductivity are the Green-Kubo and direct methods. In this section, the Green-Kubo method is described. One advantage that this method has over the direct method is that it predicts the full thermal conductivity tensor (e.g., for a superlattice, both the in-plane and cross-plane thermal conductivities) from one simulation. The direct method, which can also be used to predict the thermal resistance of an isolated interface or a thin film, is described in Section 2.6.

The Green-Kubo method is an equilibrium MD approach that relates the fluctuations of the heat current vector, $\mathbf{S}$, to the thermal conductivity via the fluctuation-dissipation theorem. The thermal conductivity in the l-th direction is given by [58]

$$k_l = \frac{1}{k_{\mathrm{B}} V T^2} \int_0^\infty \langle S_l(t) S_l(0) \rangle dt, \tag{2.12}$$

where S_l and $\langle S_l(t) S_l(0) \rangle$ are the l-th components of the heat current vector and the heat current autocorrelation function (HCACF).

There are multiple ways to define the heat current vector [59–61]. The most commonly used definition is

$$\mathbf{S}_1 = \frac{d}{dt} \sum_i \mathbf{r}(i) e_i, \tag{2.13}$$

where e_i is the total energy of atom i, and the summation is over all of the atoms in the system. In a solid, where there is no net atomic motion, the heat flux can also be written using the equilibrium positions $[\mathbf{r}_o(i)]$ as

$$\mathbf{S}_2 = \frac{d}{dt} \sum_i \mathbf{r}_o(i) e_i. \tag{2.14}$$

For the LJ potential, Eqs. (2.13) and (2.14) can be recast as

$$\mathbf{S}_1 = \sum_i e_i \mathbf{v}(i) + \frac{1}{2} \sum_i \sum_j [\mathbf{F}_{ij} \cdot \mathbf{v}(i)] \mathbf{r}_j^i, \tag{2.15}$$

$$\mathbf{S}_2 = \frac{1}{2} \sum_i \sum_j [\mathbf{F}_{ij} \cdot \mathbf{v}(i)] \mathbf{r}_{j,o}^i, \tag{2.16}$$

13

where $\mathbf{v}(i)$ is the velocity of atom i and

$$\mathbf{F}_{ij} = -\frac{\partial \phi(i,j)}{\partial \mathbf{r}(i)}. \qquad (2.17)$$

The two definitions of the heat current are compared in Fig. 2.1(a) in a plot of the HCACF normalized by its initial value and its integral (the converged value is proportional to the thermal conductivity) for the 10×10, $m_R = 2$ LJ superlattice in the cross-plane direction at a temperature of 40 K. A schematic diagram of this superlattice is provided in Fig. 2.1(b). While the integrals of the HCACFs converge to the same value, the instantaneous values of the integrals of the HCACFs are different due to the large oscillations in the HCACF obtained using the $\mathbf{S}_1$ heat current definition. Similar oscillations have been observed in the HCACFs of many different material systems [62–68]. As discussed in Appendix A, these oscillations are caused by specific zero-wavevector optical phonon modes and are related to the first summation in Eq. (2.15). The oscillations in the HCACF make accurate specification of the thermal conductivity difficult, and thus, $\mathbf{S}_2$ is used throughout the remainder of this work to predict the thermal conductivity. An added benefit of using this definition is that it does not require the calculation of the energy of each atom, reducing the computation time.

The development of an expression for $\mathbf{S}_2$ for the SW potential is complicated by the fact that there is no unique way to define e_i for many-body interatomic potentials. Schelling *et al.* examined two definitions of e_i (including the definition used here) and found that the predicted thermal conductivities agreed to within the prediction uncertainty [30]. While this result indicates that the specific definition of e_i is not critical, Chen argued that the best way to define e_i is [69]

$$e_i = \frac{1}{2} m_i |\mathbf{v}(i)|^2 + \frac{1}{2} \sum_j v_2(i,j) + \frac{1}{6} \sum_j \sum_k v_3(i,j,k), \qquad (2.18)$$

14

(a)

(b)
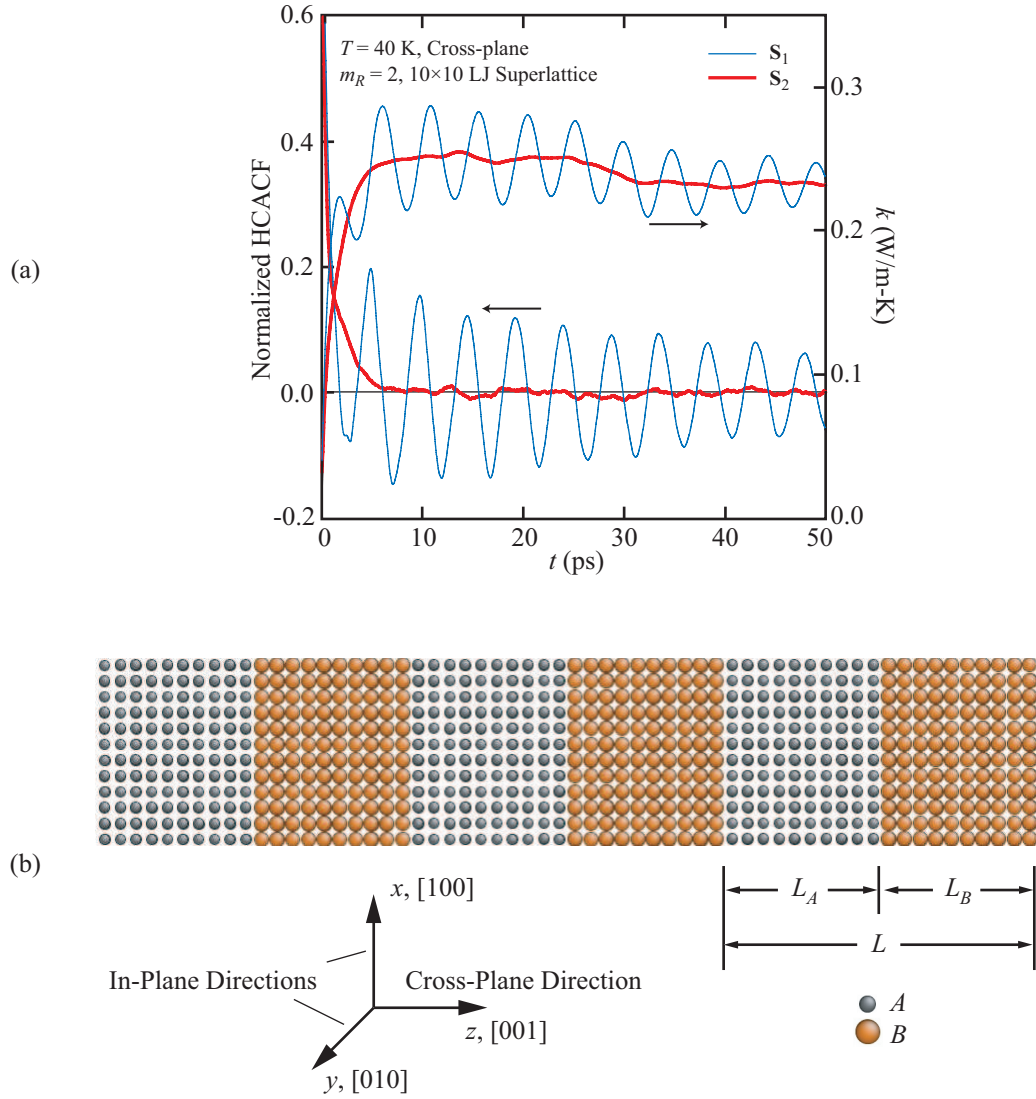
Figure 2.1: (a) Heat current autocorrelation function and its integral (the converged value is proportional to the thermal conductivity) plotted versus correlation time for the 10×10, $m_R = 2$ LJ superlattice in the cross-plane direction at a temperature of 40 K. The heat current has been calculated using the instantaneous [$\mathbf{S}_1$, Eq. (2.15)] and equilibrium [$\mathbf{S}_2$, Eq. (2.16)] atomic positions. The HCACFs are normalized by their initial values and have been averaged over five independent simulations. Reprinted with permission from Ref. [29], Copyright 2008 American Physical Society. (b) 10×10, $m_R = 2$ LJ superlattice with the cross-plane and in-plane directions labeled. The $m \times n$ notation denotes that the unit cell contains m and n monolayers of the first and second materials. For the LJ superlattices, the first material is always species A and the second is species B. This superlattice has a period length of $L = 20$ monolayers, and the interfaces are oriented along the (001) crystallographic plane.

Table 2.2: Simulation parameters and dimensions used in the Green-Kubo thermal conductivity predictions. UC, ML, SL, IP, and CP stand for conventional unit cell, monolayer, superlattice, in-plane, and cross-plane.

Sample	τ_{dc}^{GK} (ns)	τ_{eq} (ns)	τ_{corr} (ns)	N_{sim}	System Dimensions
Bulk Si and Bulk Ge	5.50	1.10	1.60	10	6^3 UCs
LJ Alloys	4.28	2.14	0.214	5	4^3 UCs
LJ SLs with $L \leq 10$ MLs	4.28	2.14	0.214	5	IP: 6^2 UCs
					CP: Eight Periods
LJ SLs with $L = 20$ MLs	4.28	2.14	0.214	5	IP: 6^2 UCs
					CP: Four Periods
LJ SLs with $L = 40$ MLs	4.28	2.14	0.214	5	IP: 6^2 UCs
					CP: Two Periods

which is the definition used here (see Ref. [69]). By substituting Eq. (2.18) into Eq. (2.14), the heat current vector can be recast as

$$\mathbf{S}_2 = \frac{1}{2}\sum_i \sum_j \mathbf{r}_{j,o}^i[\mathbf{F}_{ij} \cdot \mathbf{v}(i)] + \frac{1}{6}\sum_i \sum_j \sum_k (\mathbf{r}_{j,o}^i + \mathbf{r}_{k,o}^i)[\mathbf{F}_{ijk} \cdot \mathbf{v}(i)], \qquad (2.19)$$

where $\mathbf{F}_{ij}$ and $\mathbf{F}_{ijk}$ are

$$\mathbf{F}_{ij} = -\frac{\partial v_2(i,j)}{\partial \mathbf{r}(i)}, \quad \text{and} \qquad (2.20)$$

$$\mathbf{F}_{ijk} = -\frac{\partial v_3(i,j,k)}{\partial \mathbf{r}(i)}. \qquad (2.21)$$

2.5.2 Green-Kubo simulation details

For the Green-Kubo thermal conductivity predictions, data is collected from simulations run in the NVE ensemble for a period of τ_{dc}^{GK} after an equilibration period of τ_{eq}. During the data collection period, the heat current is calculated every five time steps. An autocorrelation length of τ_{corr} is used in the calculation of the HCACF. In order to properly sample the phase space, the HCACFs from N_{sim} independent simulations that each have random initial velocities are averaged. From the averaged HCACF, the thermal conductivity is obtained using Eq. (2.12). The value of each of these Green-Kubo parameters is provided in Table 2.2. Note that the required
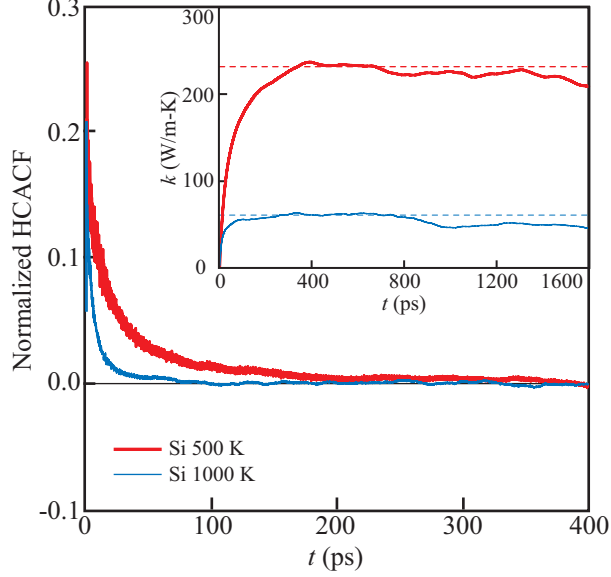
Figure 2.2: Heat current autocorrelation functions (body) and their integrals (inset) for Si at temperatures of 500 K and 1000 K. The simulation cells in both cases contain 6^3 conventional diamond unit cells (1728 atoms). The HCACFs have been normalized by their initial values and averaged over ten independent simulations.

autocorrelation period in the Si- and Ge-based materials is longer than that required for the LJ materials. This difference is due to longer phonon relaxation times in the Si- and Ge-based materials compared to the LJ materials.

2.5.3 Specification of the heat current autocorrelation function integral

Two challenges are encountered when applying the Green-Kubo method to predict thermal conductivity. The first challenge is accurately specifying the converged value of the HCACF integral, which is proportional to the thermal conductivity through Eq. (2.12). The HCACFs and their integrals are shown in Figs. 2.2 and 2.3 for Si at temperatures of 500 K and 1000 K, and for the 5×5, $m_R = 2$ and 5×5, $m_R = 5$ LJ superlattices at a temperature of 40 K as examples. Each HCACF has been normalized by its initial value. The Si HCACFs are averaged over the [001], [010], and [001] crystallographic directions, and the in-plane LJ superlattice HCACFs are

17
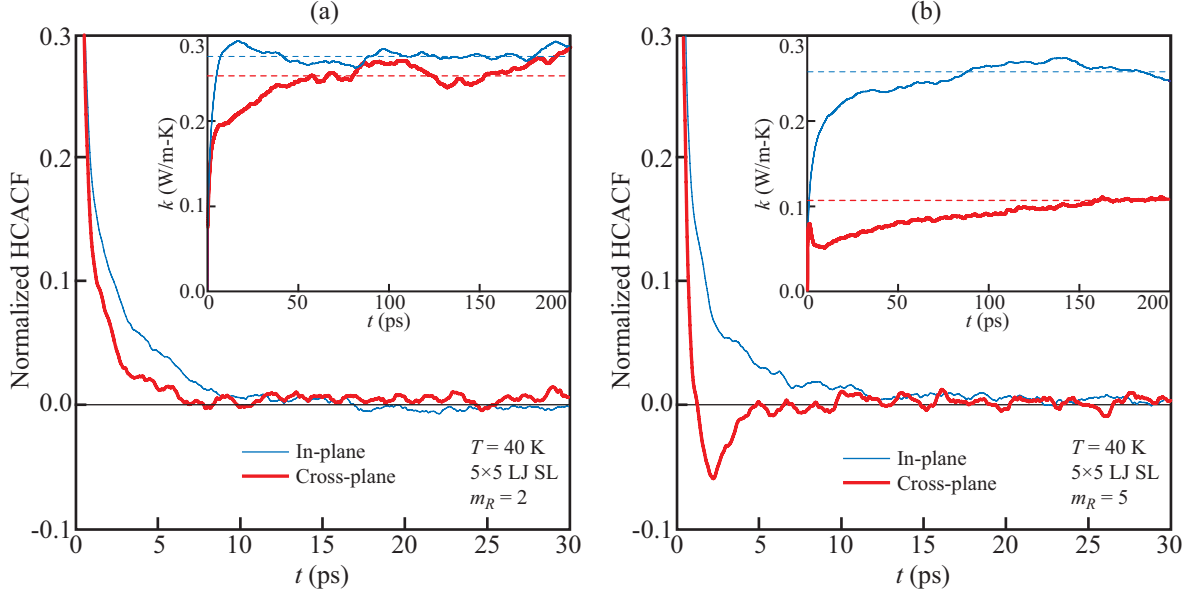
Figure 2.3: Heat current autocorrelation functions (body) and their integrals (inset) for 5×5 LJ superlattices at a temperature of 40 K with (a) $m_R = 2$, and (b) $m_R = 5$. The HCACFs have been normalized by their initial values and averaged over five independent simulations. Reprinted with permission from Ref. [29], Copyright 2008 American Physical Society.

averaged over the [001] and [010] directions.

For Si at temperatures of 500 K and 1000 K (see Fig. 2.2), the HCACF decays monotonically due to phonon-phonon scattering [70, 71]. Because phonon-phonon relaxation times decrease with increasing temperature, the HCACF decays more rapidly at a temperature of 1000 K than at a temperature of 500 K. While the HCACF integral has converged after approximately 400 ps in both cases, it begins to drift after approximately 800 ps due to noise in the HCACF at long correlation times. The converged value of the HCACF integral is therefore specified by averaging its value between 400-800 ps. The converged values of the HCACF integrals in Figs. 2.2 and 2.3 are labeled using dashed horizontal lines.

For the LJ superlattices at a temperature of 40 K [see Figs. 2.3(a) and 2.3(b)], both in-plane HCACFs appear to decay to zero after 20-30 ps, but their integrals

18

do not converge until a correlation time of approximately 50 ps. The in-plane thermal conductivity is specified on a case-by-case basis by averaging the integral of the HCACF over the region where it has converged. For the cross-plane direction, the result for the $m_R = 2$ case is qualitatively similar to that for the in-plane direction. The $m_R = 5$ case, however, exhibits different behavior. The HCACF is negative between correlation times of 1 ps and 5 ps, with a minimum at 2 ps. This negative correlation is due to energy reflection at the superlattice interfaces.[2] As with the in-plane direction, the converged value of the integral of the cross-plane HCACF is specified on a case-by-case basis. Determining the converged region of the cross-plane HCACF integral, however, is not a trivial task. For some of the complex unit cell designs that are described in Section 7.5, it is not possible to determine a region of convergence in the integral of the cross-plane HCACF, even after increasing the autocorrelation length and the number of independent simulations. Due to this challenge, the direct method, which is discussed in Section 2.6, is preferred to predict cross-plane thermal conductivity.

2.5.4 Finite simulation cell size-effects

The second challenge encountered when applying the Green-Kubo method is properly addressing the effect of the finite simulation cell-size on the predicted thermal conductivity. The thermal conductivity may depend on the size of the simulation cell if there are not enough phonon modes to accurately reproduce the phonon scattering in the corresponding bulk material. This size dependence is removed by increasing the size of the simulation cell until the thermal conductivity reaches a size-independent

---

[2]This conclusion is based on the fact that for the $L_A = L_B$ LJ superlattices, the time at the HCACF minimum increases linearly with the layer thicknesses. By plotting the layer thickness against the time at the minimum, a velocity can be extracted from the slope. This velocity is 520 m/s, approximately 70% of the average of the acoustic phonon group velocities [see Eq. (2.29)] of the bulk superlattice species. Because the two species in the $m_R = 2$ superlattices have a smaller acoustic mismatch than the $m_R = 5$ superlattices, the negative correlation caused by energy reflection at the interfaces is not as strong.

Table 2.3: Dependence of the Green-Kubo-predicted thermal conductivity on the size of the simulation cell for bulk Si at a temperature of 500 K. The prediction uncertainty is the 95% confidence interval based on the results of ten independent simulations.

Cell Size (Conventional Unit Cells)	N	k (W/m-K)
4^3	512	233 ± 45
5^3	1000	283 ± 59
6^3	1728	230 ± 47
7^3	2744	181 ± 37
8^3	4096	231 ± 57

value. In Table 2.3, the dependence of the Green-Kubo-predicted thermal conductivity on the size of the simulation cell for bulk Si at a temperature of 500 K is shown. The provided prediction uncertainties are the 95% confidence intervals based on the results of ten independent simulations. There is no discernable size-dependence in the thermal conductivity for simulation cells containing 4^3 to 8^3 conventional unit cells, a finding that is in agreement with the results of Schelling *et al.* for SW Si at a temperature of 1000 K [30].

For the LJ superlattices, the cross-plane dimensions required to remove the simulation cell-size effect are superlattice dependent. For LJ superlattices with period lengths, L, less than or equal to 10 monolayers, eight periods are required. For the LJ superlattices with $L = 20$ monolayers and $L = 40$ monolayers, four and two periods are required. The required length of the simulation cell is smaller for the small-period superlattices than the large-period superlattices because there is more phonon scattering due to the larger number of interfaces. In all cases, the required in-plane dimensions are six unit cells by six unit cells. These in-plane dimensions are larger than the four unit cells by four unit cells often reported to remove the Green-Kubo simulation-cell-size effects in LJ Ar [70,71]. This difference is attributed to the non-cubic simulation cells used here. The simulation cell-sizes used in the

Green-Kubo thermal conductivity predictions discussed throughout the remainder of this work are provided in Table 2.2.

2.6 Direct method for predicting thermal conductivity and thermal resistance

2.6.1 Overview

The direct method is a nonequilibrium, steady-state MD approach for predicting thermal conductivity or thermal resistance [30, 59]. Schematic diagrams of the direct method simulation cells are shown in Figs. 2.4(a)-2.4(c). In each case, the simulation cell contains a sample region bordered by hot and cold reservoirs of length L_{res} and fixed boundaries in the z direction. The fixed boundary regions each contain four monolayers of fixed atoms in order to prevent reservoir atoms from sublimating. Because this thickness exceeds the cutoff radius of the interatomic potentials (i.e., the distance beyond which the interatomic potential is zero), the atoms in the reservoirs "see" an infinite boundary region. The cross-section of the simulation cell is square and has area A_c. Periodic boundary conditions are imposed in the x and y directions.

In the direct method, a known heat flux, q, is applied across the sample, causing a temperature profile to develop. For predictions of the thermal conductivity, the temperature gradient within the sample region is specified and the thermal conductivity is determined using the Fourier law,

$$k = \frac{-q}{dT/dz}. \tag{2.22}$$

Alternatively, a temperature gradient can be imposed across the sample, and the resulting heat flux can be measured. Lukes *et al.* noted, however, that long simulation times are required to obtain convergence of the heat flux value when using the imposed temperature gradient method [32], and therefore, the imposed heat flux method is
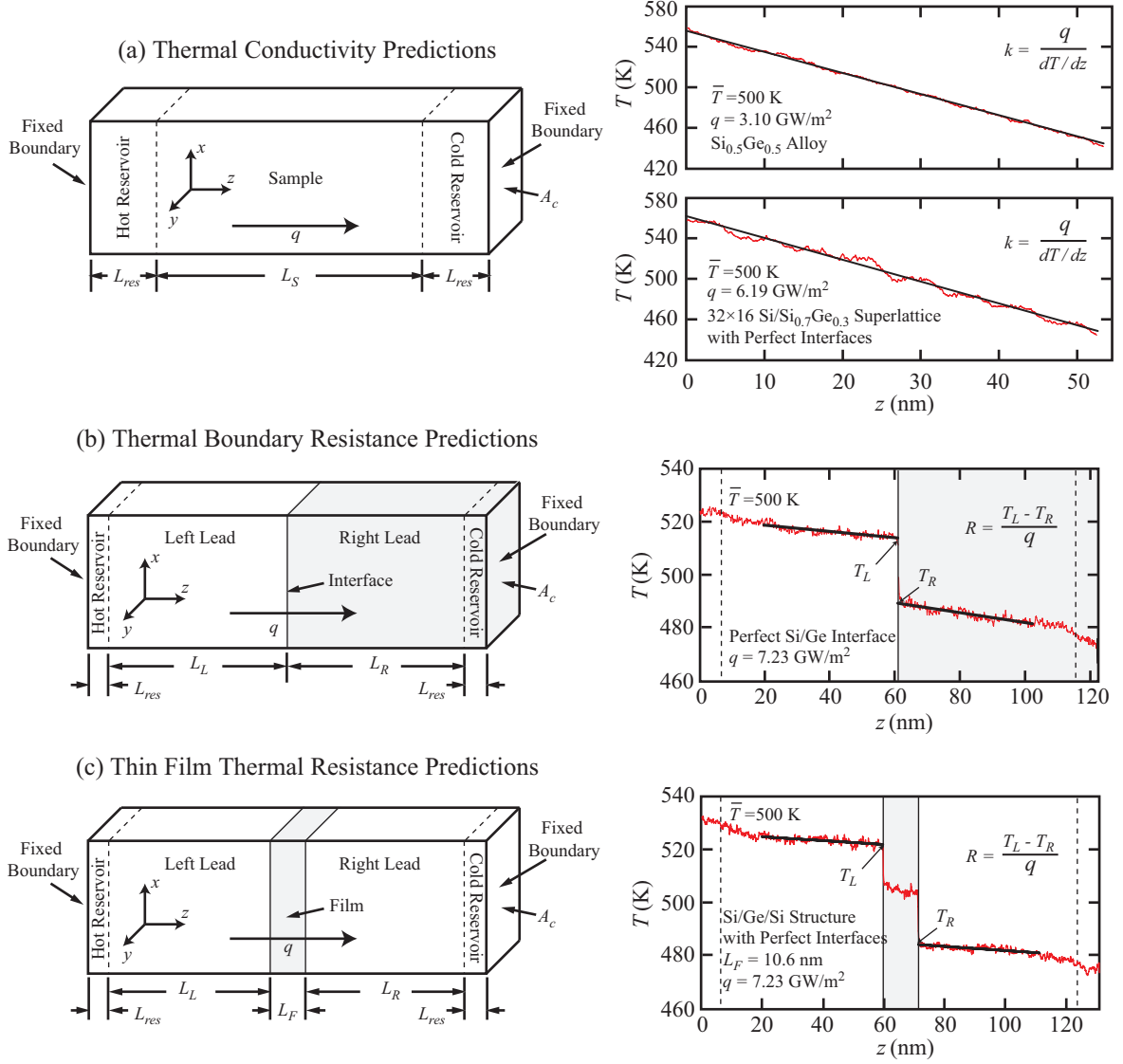
Figure 2.4: Schematic diagrams of the direct method simulation cells used in the predictions of (a) thermal conductivity, (b) thermal boundary resistance, and (c) thin film thermal resistance. In each simulation cell, periodic boundary conditions are imposed in the x and y directions. Several representative steady-state temperature profiles are also provided. The temperature profiles provided for the thermal conductivity predictions correspond to the sample region, while the temperature profiles provided for the thermal resistance predictions correspond to the entire simulation cell.

used here. For predictions of the thermal boundary resistance and thin film thermal resistance, the temperature drop across either the interface or film, $T_L - T_R$, is specified

and the thermal resistance, R, is determined by

$$R = \frac{T_L - T_R}{q}. \qquad (2.23)$$

2.6.2 Data collection and analysis

The sample and reservoirs are set to an initial temperature profile by scaling the atomic velocities for a period of τ_{set}. For simulations of the Si- and Ge-based materials and LJ Ar, a uniform temperature profile is imposed across the system. For simulations of LJ superlattices, a linear temperature profile is imposed in order to quickly achieve a steady-state temperature profile. The initial temperature profile for these simulations has a total temperature drop of 10 K, and the midpoint of the sample is set to the desired average temperature of the simulation cell, $\bar{T}$. The heat flux is then applied using the method described in Section 2.6.3. From this point, a period of τ_{ss} is allowed for the sample to reach steady-state conditions. The time required to reach steady-state conditions is inversely proportional to the effective thermal diffusivity of the entire sample, a quantity that is proportional to the thermal conductivity and indicates how quickly a material adjusts to temperature changes [72]. After the sample has reached steady-state conditions, data are collected for an additional period of τ_{dc}^{DM} for the thermal conductivity or thermal resistance prediction. The values of τ_{set}, τ_{ss}, and τ_{dc}^{DM} are provided in Table 2.4.

The steady-state temperature profile is obtained by averaging the temperature of each monolayer over the data collection period. The temperature profiles across the $Si_{0.5}Ge_{0.5}$ alloy, the 32×16 $Si/Si_{0.7}Ge_{0.3}$ superlattice, the Si/Ge interface and a Si/Ge/Si thin film structure at an average temperature of 500 K are provided in Figs. 2.4(a)-2.4(c) as examples. For the thermal conductivity predictions, a least-squares linear regression analysis is used to calculate the temperature gradient. Alternatively,

Table 2.4: Simulation parameters and dimensions used in the direct method. UC, ML, and SL stand for conventional unit cell, monolayer, and superlattice. The number provided in parentheses is the number of sample lengths used in the linear extrapolation procedure (if applicable).

Sample	τ_{set} (ns)	τ_{ss} (ns)	τ_{dc}^{DM} (ns)	q (GW/m^2)	A_c (UCs)	L_{res} (MLs)	$L_L = L_R$ (MLs)	L_S (MLs)
Si$_{1-x}$Ge$_x$ Alloys	0.55	3.3	1.1	3.10	4^2	128	-	320-512 (3)
Si/Si$_{0.7}$Ge$_{0.3}$ SLs	0.55	3.3	1.1	6.19	4^2	≥ 128	-	256-672 (4)
Si/Ge SLs	0.55	3.3	2.8	6.19	4^2	≥ 128	-	240-960 (4)
LJ SLs $m_R = 2$								
$\quad L < 16$ MLs	0.11	4.3	8.6	See Text	4^2	4	-	≥ 256 (1)
$\quad L \geq 16$ MLs	0.11	4.3	8.6	See Text	4^2	4	-	60-240 (4)
LJ SLs $m_R = 5$								
$\quad L < 16$ MLs	0.11	8.6	8.6	See Text	4^2	4	-	≥ 256 (1)
$\quad L \geq 16$ MLs	0.11	8.6	8.6	See Text	4^2	4	-	60-240 (4)
Si- and Ge-based Interfaces and Thin Films								
$\quad T = 300$ K	0.55	3.3	2.8	7.23	4^2	50	700	-
$\quad T = 400$ K	0.55	3.3	2.8	7.23	4^2	50	500	-
$\quad T \geq 500$ K	0.55	3.3	2.8	7.23	4^2	50	400	-

the temperature gradient could be specified as the difference between the temperatures at the ends of the sample region divided by the sample length [73]. Because more data is used to specify the temperature gradient using the least-squares regression analysis, this method is applied as it will be less susceptible to statistical fluctuations. For thermal resistance predictions, a least-squares linear regression analysis is applied to the temperature profile in each lead and the linear fits are evaluated at the interface or the lead/film boundaries to specify the temperature drop. The nonlinear regions in the temperature profile found in the 100 monolayers closest to the reservoir/sample boundary are neglected when performing the regression analysis for the thermal resistance predictions. The linear fits are also provided for the temperature profiles shown in Figs. 2.4(a)-2.4(c).

2.6.3 Imposing the heat flux

The heat flux is generated by adding a constant amount of kinetic energy, ΔE_k, to the hot reservoir and removing ΔE_k from the cold reservoir at every time step using the method described by Ikeshoji and Hafskjold [74]. The heat flux generated with this scheme is

$$q = \frac{\Delta E_k}{A_c \Delta t}.$$

(2.24)

The value of the heat flux should be chosen so that the temperature drop across the sample, interface, or thin film is larger than the statistical temperature fluctuations in the temperature profile. This requirement ensures that the temperature gradient or temperature drop can be accurately specified. The value of the heat flux should not be so large, however, that nonlinear temperature profiles are introduced due to the temperature-dependence of the thermal conductivity.

For Si- and Ge-based materials and LJ Ar, a range of heat fluxes is examined to ensure that the predicted thermal conductivity or thermal resistance does not depend on the value of the heat flux. The effect of the heat flux on the Si/Ge thermal boundary resistance is provided in Table 2.5 as an example. The thermal boundary resistance provided for case A is the 95% confidence interval based on the results of five independent simulations while for the other cases, the provided value is the result of one simulation. The Si/Ge thermal boundary resistance is independent of the imposed heat flux (compare cases A, C, and D) over the range of values considered. The heat fluxes that generate heat flux-independent predictions are summarized in Table 2.4.

For the LJ superlattices, a guess-and-check approach is used to obtain a value of the heat flux that results in a temperature drop across the sample, ΔT, that is within

Table 2.5: Effect of the direct method simulation parameters (q, L_L, L_R, L_{res}, A_c, and sample orientation) on the MD-predicted Si/Ge thermal boundary resistance at a temperature of 500 K. For the sample orientation, Si/Ge (Ge/Si) indicates that Si (Ge) is on the hot side and Ge (Si) is on the cold side of the simulation cell. The thermal boundary resistance provided for case A is the 95% confidence interval based on the results of five independent simulations. UC stands for convenctional unit cell.

	q (GW/m^2)	$L_L = L_R$ (monolayers)	L_{res} (monolayers)	A_c (UCs)	Orientation	R (10^{-9} m^2 K/W)
A	7.23	400	50	4^2	Si/Ge	2.93 ± 0.29 (95%)
B	7.23	400	50	4^2	Ge/Si	2.94
C	3.10	400	50	4^2	Si/Ge	3.02
D	13.4	400	50	4^2	Si/Ge	2.97
E	7.23	200	50	4^2	Si/Ge	4.01
F	7.23	300	50	4^2	Si/Ge	3.22
G	7.23	500	50	4^2	Si/Ge	2.72
H	7.23	600	50	4^2	Si/Ge	2.83
I	7.23	400	20	4^2	Si/Ge	3.17
J	7.23	400	100	4^2	Si/Ge	2.95
K	7.23	400	50	4^2	Si/Ge	3.13
L	7.23	400	50	4^2	Si/Ge	2.81

1 K from initial temperature drop of 10 K. This approach ensures that the sample has reached steady-state after a period of τ_{ss}. In this approach, the temperature drop across the sample is defined to be

$$\Delta T = -L_S \frac{dT}{dz},$$

(2.25)

where L_S is the sample length used in the thermal conductivity predictions [see Fig. 2.4(a)].

2.6.4 Finite simulation cell-size effect

Removal of size-dependence in thermal resistance predictions

As with the Green-Kubo method, a challenge associated with the direct method is obtaining predictions that are independent of the size of the simulation cell. For example, the thermal conductivity may depend on the sample length when it is on the order of the bulk phonon mean free paths. If this is the case, the amount of phonon scattering at the boundaries between the reservoirs and the sample is comparable to

that occurring within the sample itself, leading to phonon dynamics not representative of a bulk sample. Similarly, the thermal boundary resistance may depend on the length of the left and right leads, L_L and L_R [see Figs. 2.4(b) and 2.4(c)], when they are on the order of the bulk phonon mean free paths. If this is the case, phonons can travel ballistically from the reservoirs to the interface, leading to incident phonon distributions that are not representative of an interface between two bulk materials.

The guaranteed method for removing the finite simulation cell-size effect is to increase the size of the simulation cell until size-independent results are obtained. This method is demonstrated in Table 2.5 for predictions of the Si/Ge thermal boundary resistance at a temperature of 500 K. The thermal boundary resistance is independent of the reservoir length (compare cases A, I, and J) and cross-sectional area (cases A, K, and L) over the range of values considered. The thermal boundary resistance is found to decrease with increasing L_L and L_R until size-independent results are obtained when L_L and L_R are greater than or equal to 400 monolayers (cases A and E-H). The thermal boundary resistance is also independent of the sample orientation (i.e., the sample can be oriented with either species on the hot side of the simulation cell), see cases A and B.

The results presented in Table 2.5 indicate that the Si/Ge thermal boundary resistance at a temperature of 500 K is independent of the size of the simulation cell when using the dimensions provided for case A. These dimensions are used for all of the thermal resistance predictions at temperatures greater than or equal to 500 K. At temperatures lower than 500 K, however, these dimensions may not be sufficient to remove the simulation cell size-effect. To ensure that this effect is negligible, simulation cells with $L_L = L_R = 700$ monolayers and $L_L = L_R = 500$ monolayers are used at temperatures of 300 K and 400 K. These values of L_L and L_R are roughly a factor

of $500/T$ greater than the values provided for case A. This factor is chosen based on the fact that thermal conductivity of a crystal is approximately proportional to T^{-1} in the classical limit, and on the kinetic theory prediction that the average phonon mean free path is proportional to the thermal conductivity [52]. The dimensions that generate size-independent thermal resistance predictions are summarized in Table 2.4.

Removal of size-dependence in thermal conductivity predictions

Increasing the size of the simulation cell until size-independent results are obtained is also found to be an effective method to remove the thermal conductivity dependence on cross-sectional area and reservoir length. Aside from the LJ superlattices with $L <$ 16 monolayers, however, the sample length cannot be made large enough to remove its effect on the thermal conductivity due to computational expense. This challenge is encountered because low-frequency phonon modes, which have large phonon mean free paths, make significant contributions to the thermal conductivity. For example, 41% of the thermal conductivity of bulk SW Si at a temperature of 500 K is predicted from anharmonic LD calculations to be due to phonons with frequencies less than 20 rad/ps (the maximum frequency in bulk SW Si is 112 rad/ps) [75]. The average mean free path of these phonons in the [001] direction is over 0.5 μm [75]. For comparison, these phonons are predicted from harmonic LD calculations to contribute only 14% to the thermal conductance across the Si/Ge interface. This small contribution explains why the thermal resistance predictions are less sensitive to sample length than the thermal conductivity predictions.

When computational expense prevents the removal of the sample length-effect by simply increasing the sample length, a post-processing procedure is required to extrapolate the results for several sample lengths. The extrapolation procedure used here is

based on the assumption that the thermal conductivity depends only on the sample length and the phonon properties in the corresponding bulk material, or equivalently,

$$\frac{1}{k} = \chi \left[\text{bulk phonon properties}, \frac{1}{L_S} \right].$$ (2.26)

Here, χ is a function of the bulk phonon properties and L_S^{-1}. This function converges to k_∞^{-1} as $L_S^{-1} \rightarrow 0$, where k_∞ is the bulk thermal conductivity. In theory, k_∞^{-1} can be estimated by predicting χ and its partial derivatives with respect to L_S^{-1} (denoted by χ', χ'', etc.) at some finite sample length and extrapolating to $\chi[0]$ using a Taylor series expansion, i.e.,

$$\frac{1}{k_\infty} = \chi[0] = \chi[L_S^{-1}] + \frac{\chi'[L_S^{-1}]}{1!} \left(\frac{-1}{L_S} \right) + \frac{\chi''[L_S^{-1}]}{2!} \left(\frac{-1}{L_S} \right)^2 + ...$$ (2.27)

To obtain the partial derivatives of χ, one could use the direct method to predict the thermal conductivities for a range of sample sizes and take the derivatives of a polynomial fit to a plot of k^{-1} versus L_S^{-1} (i.e., χ versus L_S^{-1}). It is difficult, however, to specify the second- and higher-order derivatives with this approach due to uncertainty in the direct method predictions and the need to consider at least $N+1$ different sample sizes to calculate an N-th order derivative. To avoid this challenge, k_∞^{-1} is approximated by truncating Eq. (2.27) after the first-order term. Under this approximation, the procedure used to estimate the bulk thermal conductivity reduces to plotting k^{-1} versus L_S^{-1} for a range of sample lengths and extrapolating a linear fit to the data to $L_S^{-1} = 0$. This linear extrapolation procedure is thus equivalent to that used by others who justified it using the kinetic theory expression for thermal conductivity and the Matthiesen rule [29, 30, 76–78].

An advantage of this description of the linear extrapolation procedure over the kinetic theory/Matthiesen rule-based description is that it allows an avenue to determine when the extrapolation procedure can be expected to be accurate. In Appendix

Table 2.6: Lattice constants, densities, and elastic constants for LJ Ar, SW Si, and SW Ge at a temperature of 0 K. The properties are from Refs. [48, 49, 80–82].

Property	LJ Ar	SW Si	SW Ge
a (Å)	5.269	5.43095	5.65362
ρ (kg/m^3)	1813	2329	5340
C_{11} (GPa)	4.113	151.6	138.3
C_{12} (GPa)	2.286	76.5	50.9
C_{44} (GPa)	2.430	56.5	58.8

B, a metric is derived for this determination. The derivation is based on the assumptions that (i) the optical phonons make negligible contribution to the thermal conductivity, (ii) the phonon dispersion curves for the acoustic phonons are linear and isotropic (i.e., the Debye approximation), (iii) the only intrinsic phonon scattering[3] mechanism is phonon-phonon scattering and its associated relaxation time is proportional to ω^{-2}, and (iv) the relaxation times associated with phonon-phonon and phonon-boundary scattering are independent. These assumptions are reasonable for Ar, Si, and Ge. Under these assumptions, the error introduced by truncating Eq. (2.27) after the first-order term is expected to be less than 10% when

$$L_S > \frac{24 k_\infty \Omega}{k_{\mathrm{B}} v_{ac}},\qquad(2.28)$$

where Ω is the volume of the primitive cell, v_{ac} is a representative group velocity for the acoustic phonons, and L_S is taken here to be the average sample length used in the extrapolation.

Because computational expense effectively sets the sample length that can be simulated with the direct method, Eq. (2.28) is applied to determine the maximum thermal conductivity that can be accurately predicted using the linear extrapolation procedure, k_∞^{max}. In other words, if the bulk thermal conductivity estimated using

---

[3]Possible sources of intrinsic phonon scattering are phonon-phonon scattering, phonon-electron scattering, and phonon scattering at defects and internal interfaces [38, 79].

the linear extrapolation procedure, k_∞^{est}, exceeds k_∞^{max}, then the prediction may not be accurate. An estimate for k_∞^{max} for Ar, Si, and Ge is obtained by taking v_{ac} to be the average of the [001] longitudinal acoustic $(v_{ac,L}^{[001]})$ and two transverse acoustic group velocities $(v_{ac,T}^{[001]})$ in the long-wavelength limit, i.e.,

$$v_{ac} = \frac{v_{ac,L}^{[001]} + 2v_{ac,T}^{[001]}}{3}, \tag{2.29}$$

where $v_{ac,L}^{[001]} = (C_{11}/\rho)^{1/2}$ and $v_{ac,T}^{[001]} = (C_{44}/\rho)^{1/2}$ [51]. Here, ρ, C_{11}, and C_{44} are the material density and elastic constants. The values of these properties for Ar, Si, and Ge are provided in Table 2.6. Substituting Eq. (2.29) and $\Omega = a^3/4$ (the primitive cell volume for face-centered cubic and diamond crystal lattices) into Eq. (2.28) and solving for k_∞^{max} yields

$$k_\infty^{max} = \frac{L_S k_B (C_{11}^{1/2} + 2C_{44}^{1/2})}{18a^3\rho^{1/2}}, \tag{2.30}$$

where a is the lattice constant. The average sample length used in the direct method simulations presented in this thesis is approximately 50 nm, which is a length that requires moderate computational expense.[4] For this length, k_∞^{max} is estimated to be 1 W/m-K, 4 W/m-K, and 2 W/m-K for Ar, Si, and Ge.

The linear extrapolation procedure to estimate the bulk thermal conductivity is demonstrated in Fig. 2.5 for Ar at a temperature of 20 K, and the $Si_{0.5}Ge_{0.5}$ alloy, the 32×16 $Si/Si_{0.7}Ge_{0.3}$ and 24×24 Si/Ge superlattices, and Ge at a temperature of 500 K. For each sample, the trend of k^{-1} versus L_S^{-1} appears linear. The estimated bulk thermal conductivity is obtained by extrapolating a linear fit to the data to $L_S^{-1} = 0$. For Ar at a temperature of 20 K, $k_\infty^{est} = 1.4$ W/m-K, a value that does not significantly exceed k_∞^{max} and is in good agreement with the Green-Kubo prediction of 1.2 W/m-K [80]. For Si (not shown in Fig. 2.5) and Ge at a temperature of

---

[4]A 6 ns simulation of SW Si with $L_S = 50$ nm ($\sim$370 monolayers), $A_c = 4^2$ UCs, and $L_R = 128$ monolayers contains approximately 20,000 atoms and requires $\sim$200 processor hours.
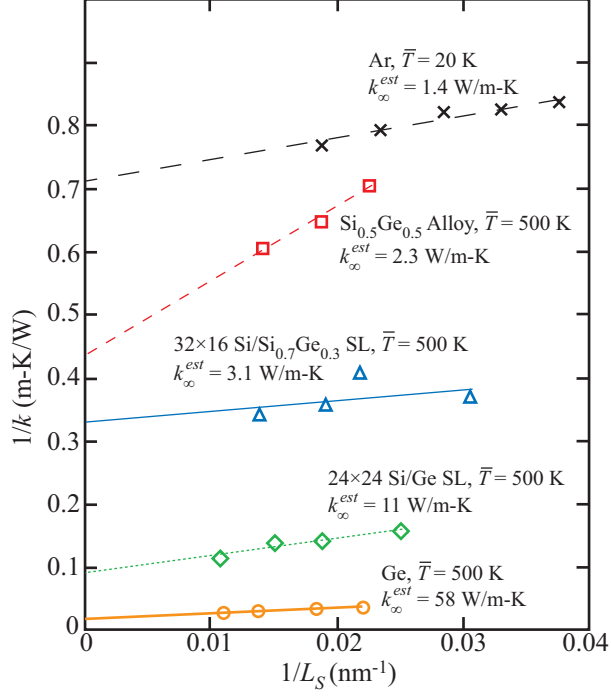
Figure 2.5: Inverse of the direct method-predicted thermal conductivity versus inverse of the sample length. The bulk thermal conductivity is estimated by extrapolating to an infinite system size $(1/L_S \to 0)$.

500 K, k_∞^{est} is equal to 93 W/m-K and 58 W/m-K. These values are less than half of the corresponding Green-Kubo predictions (see Table 2.3). Because k_∞^{est} is 20-30 times greater than k_∞^{max} for both materials, this discrepancy is attributed to error introduced by neglecting the second- and higher-order terms in the extrapolation procedure [see Eq. (2.27)]. For the $Si_{0.5}Ge_{0.5}$ alloy and the 32×16 $Si/Si_{0.7}Ge_{0.3}$ and 24×24 Si/Ge superlattices at a temperature of 500 K, the estimated bulk thermal conductivities are 2.3 W/m-K, 3.1 W/m-K, and 11 W/m-K. These predictions are believed to be accurate for two reasons. First, the values of k_∞^{est} are close to the k_∞^{max} values for Si and Ge. Second, the additional intrinsic scattering mechanisms in alloys and superlattices (e.g., phonon scattering at atomic substitutions and the internal interfaces interfaces [38,83]) will lead to smaller required sample lengths for accurate
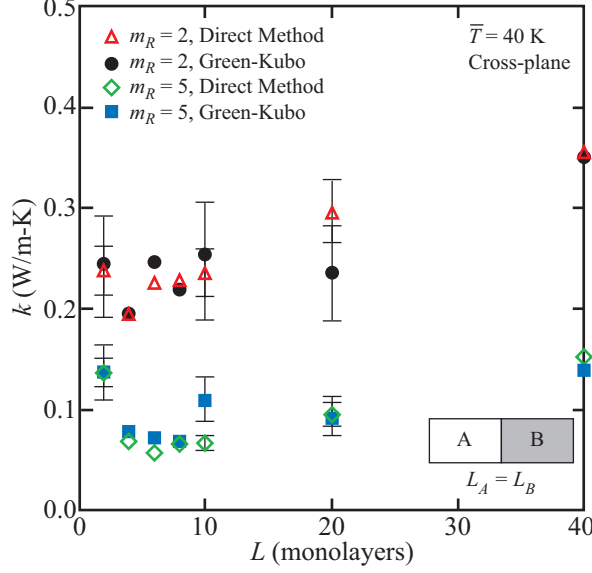
Figure 2.6: Comparison between the thermal conductivity predictions obtained by the Green-Kubo and direct methods for $m_R = 2$ and $m_R = 5$, $L_A = L_B$ LJ superlattices at a temperature of 40 K. The cross-plane thermal conductivity is plotted as a function of period length ($L = L_A + L_B$). Error bars have been included for a selection of the results. Reprinted with permission from Ref. [29], Copyright 2008 American Physical Society.

thermal conductivity predictions.

2.7 Quantitative comparisons between the Green-Kubo and direct method predictions of the thermal conductivity

Despite the substantial differences in theory and implementation between the Green-Kubo and direct methods, little work has been conducted to quantitatively compare the thermal conductivity predictions obtained by both methods. Two exceptions are the work of Schelling *et al.* [30] and Zhou *et al.* [84]. Schelling *et al.* predicted the thermal conductivity of SW Si at a temperature of 1000 K to be 62 ± 16 W/m-K using the Green-Kubo method and 65 ± 16 W/m-K using the direct method. For their direct method prediction, the linear extrapolation procedure with an average sample length of ∼100 nm was used. The error associated with the linear extrapolation method is estimated here to be approximately 20% at this sample length (see Fig.

B.1).[5] Their finding that the two methods agree to within the prediction uncertainty is thus consistent with the length-dependent thermal conductivity model discussed in Appendix B. Zhou *et al.* compared the prediction methods for GaN at temperatures of 500 K and 800 K and also found agreement to within the prediction uncertainty.

Here, the thermal conductivity prediction methods are compared for cross-plane direction of the $L_A = L_B$ LJ superlattices with $m_R = 2$ and $m_R = 5$ at a temperature of 40 K. The results are shown in Fig. 2.6. Error bars corresponding to the prediction uncertainties (estimated based on predicted repeatability to be $\pm 10\%$ for the direct method and $\pm 20\%$ for the Green-Kubo method) are provided for several points. For all but one point ($m_R = 5$, 5×5), the two sets of predictions are in agreement and neither method consistently underpredicts or overpredicts the other. It is thus concluded that either the Green-Kubo method or direct method can be used to predict the superlattice cross-plane thermal conductivity.

2.8 Summary

Because no assumptions concerning the nature of the phonon transport are required, MD simulations are an ideal tool for predicting thermal conductivity and thermal resistance, provided a suitable interatomic potential function is available. In this chapter, the methodology related to the MD-based Green-Kubo and direct methods was discussed. The discussion focused on predicting the thermal transport properties of SW Si- and SW Ge-based materials and LJ superlattices. The primary challenge associated with applying the Green-Kubo method is specifying the converged value of the HCACF integral. Removal of the finite size-effect is the primary challenge associated with applying the direct method. When these challenges are

---

[5]The normalized sample length [see Eq. (B.12)] is calculated to be $l = 5$ using a bulk thermal conductivity of $k_\infty \approx 60$ W/m-K and the material properties provided in Table 2.4.

properly addressed, thermal conductivities predicted using both methods are found to be in agreement.

CHAPTER III

Lattice dynamics calculations

3.1 Introduction

Molecular dynamics simulation is an ideal tool for predicting phonon mode-averaged properties such as thermal conductivity and thermal resistance. It is challenging, however, to extract additional model-level details related to the thermal transport from an MD simulation due to computational expense [85–87]. Such details are more easily obtained using LD calculations [88], in which the system dynamics are transformed from the real-space coordinates (the atomic positions) to the reciprocal-space coordinates (the phonon modes). In this chapter, the methodology related to LD calculations of phonon frequencies, polarization vectors, group velocities, and transmission coefficients is provided. These phonon properties are used to calculate thermal boundary resistance and thin film thermal resistance in Chapters IV and V.

3.2 Phonon frequencies and polarization vectors

In this thesis, the LD calculations are performed under the harmonic approximation to decrease the required computational time. In this approximation, a Taylor series expansion of the system potential energy about the equilibrium atomic coordinates is truncated after the second-order term [38, 88]. The harmonic approximation is exact at zero temperature and is of good accuracy for stiff materials with small

36

thermal expansion coefficients such as Si and Ge.[1] The primary drawback of the harmonic approximation, however, is that no information about inelastic phonon scattering (e.g., the phonon-phonon relaxation times) can be obtained because the phonon modes are decoupled. These properties can be obtained from anharmonic LD calculations [38,43,89], which treat the anharmonicity of the crystal as a perturbation to the harmonic solution.

Under the harmonic approximation, the equation of motion of the jth atom in the kth unit cell is [88]

$$m_j \ddot{\mathbf{u}}(jk,t) = \sum_{j'} \sum_{k'} \mathbf{\Psi}(jk, j'k') \mathbf{u}(jk, t), \qquad (3.1)$$

where $\mathbf{u}$ is the displacement of atom jk from its equilibrium position, and the summation is over every atom in the crystal (including jk itself).[2] The 3×3 second-order force constant matrix $\mathbf{\Psi}$ describes the interaction between atoms jk and $j'k'$ and is defined as

$$\mathbf{\Psi}(jk, j'k') = \frac{\partial^2 \Phi}{\partial \mathbf{r}(jk) \partial \mathbf{r}(j'k')}. \qquad (3.2)$$

While force constant matrices can be calculated analytically [66], they are more easily calculated numerically for the Stillinger-Weber potential due to its complicated three-body interactions. The force constant matrix can be efficiently calculated by taking the negative of the partial derivative of the force on atom $j'k'$ [see Eq. (2.5)] with respect to the position of atom jk.

The solution to Eq. (3.1) is a superposition of the crystal's normal (phonon) modes, which are assumed to be spatially delocalized plane waves. Each mode is

---

[1]For example, the phonon frequencies calculated using harmonic and anharmonic LD-based methods differ by less than 3% in SW Si below temperatures of 1000 K [43].

[2]This summation is not as daunting as it may first appear. In nonpolar materials, such as Si and Ge, each atom has non-negligible interactions with only its first few nearest neighbor shells. For the SW potential in particular, the second-order force constants are zero beyond the second nearest neighbor shell.

denoted by a wave vector $\boldsymbol{\kappa}$ and polarization ν such that [88]

$$\mathbf{u}(jk, t) = \sum_{\boldsymbol{\kappa}} \sum_{\nu} \mathbf{U}(j, \boldsymbol{\kappa}, \nu) \exp\{i[\boldsymbol{\kappa} \cdot \mathbf{r}(jk) - \omega(\boldsymbol{\kappa}, \nu)t]\}, \tag{3.3}$$

where ω is the mode frequency and $\mathbf{U}$ is the complex mode-dependent displacement vector that describes the vibrational amplitude of atom j relative to the other atoms in the unit cell. Substituting Eq. (3.3) into Eq. (3.1) leads to the eigenvalue equation [88]

$$\omega^2(\boldsymbol{\kappa}, \nu)\mathbf{e}(\boldsymbol{\kappa}, \nu) = \mathbf{D}(\boldsymbol{\kappa})\mathbf{e}(\boldsymbol{\kappa}, \nu), \tag{3.4}$$

where $\mathbf{D}$ is the $3n \times 3n$ dynamical matrix and $\mathbf{e}$ is the mode-dependent polarization vector of length $3n$, where n is the number of atoms in the unit cell. The dynamical matrix is comprised of n^2 $3{\times}3$ sub-matrices, one for each j-j' pair. These sub-matrices are

$$\mathbf{D}_{jj'}(\boldsymbol{\kappa}) = \frac{1}{(m_j m_{j'})^{1/2}} \sum_{k'} \boldsymbol{\Psi}(j1, j'k') \exp(i\boldsymbol{\kappa} \cdot \mathbf{r}_{j1}^{j'k'}), \tag{3.5}$$

where 1 denotes the reference unit cell, and the summation is over all unit cells. The polarization vector contains $3n$ complex elements that are

$$
\begin{aligned}
[\mathbf{e}(\boldsymbol{\kappa}, \nu)]^T &= \left[m_1^{1/2}U_x(1, \boldsymbol{\kappa}, \nu), m_1^{1/2}U_y(1, \boldsymbol{\kappa}, \nu), m_1^{1/2}U_z(1, \boldsymbol{\kappa}, \nu), \right. \\
&\qquad \left. m_2^{1/2}U_x(2, \boldsymbol{\kappa}, \nu) \dots, m_n^{1/2}U_z(n, \boldsymbol{\kappa}, \nu) \right],
\end{aligned}
\tag{3.6}
$$

where U_x, U_y, and U_z are the x, y, and z components of $\mathbf{U}$ and the superscript T denotes the transpose. The polarization vector is normalized such that $\mathbf{e}^\dagger \cdot \mathbf{e} = 1$, where the superscript $\dagger$ denotes the conjugate transpose.

At each wave vector, there are $3n$ phonon modes. Each mode has an associated frequency and polarization vector. The frequencies are the square roots of the eigenvalues of $\mathbf{D}$ and the polarization vectors are the eigenvectors of $\mathbf{D}$. Because the
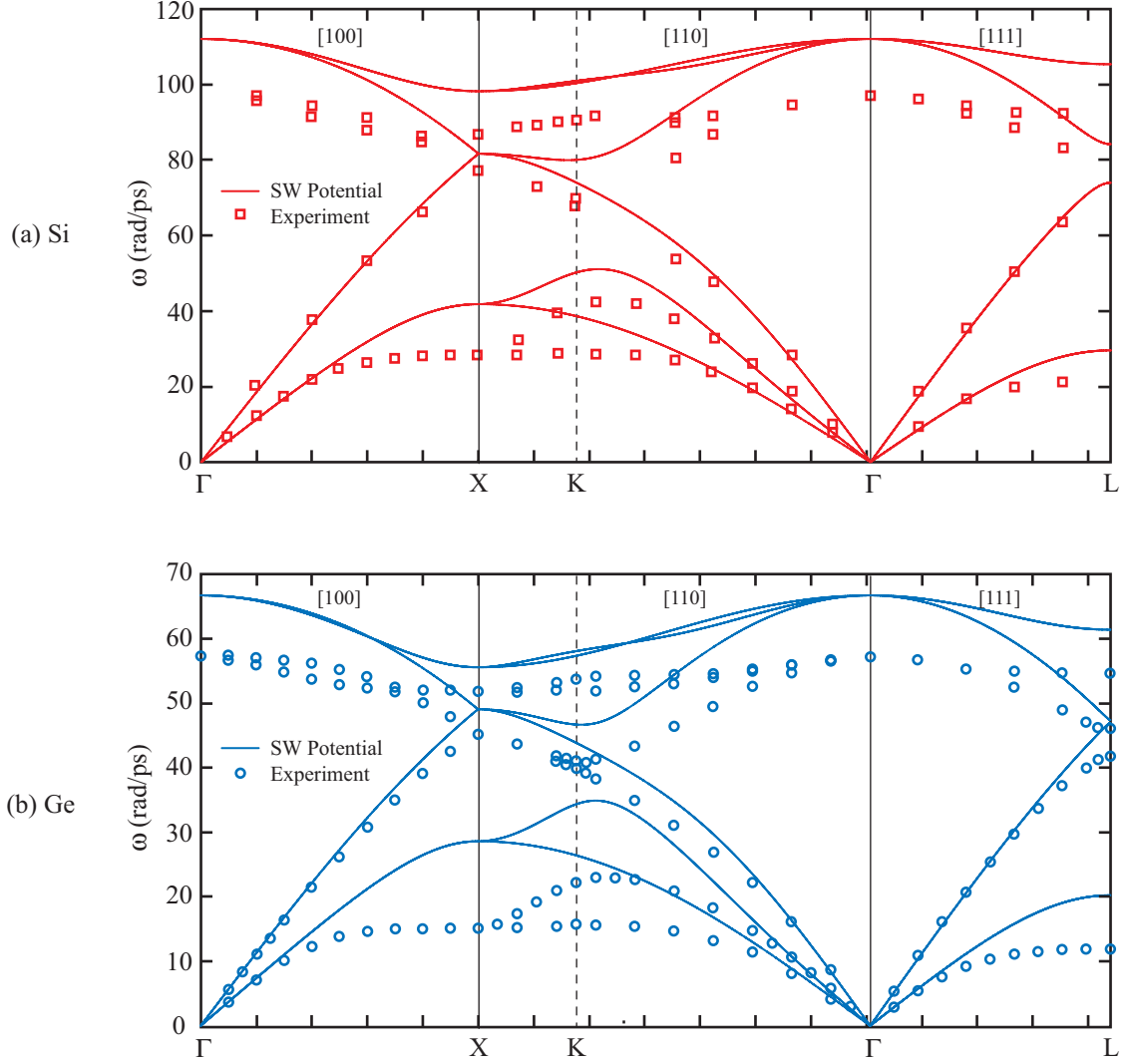
Figure 3.1: Phonon dispersion curves along the high symmetry directions for (a) bulk SW Si and (b) bulk SW Ge. The experimentally-measured phonon dispersion curves for Si (read from Fig. 1 of Ref. [90]) and Ge (from Ref. [91]) are provided for comparison. Note the differences in the frequency scale between the plots. The labels Γ, X, K, and L denote high-symmetry points in the Brillouin zone. In the first Brillouin zone, these points have coordinates of $\Gamma = (0, 0, 0)$, $X = \frac{2\pi}{a}(1, 0, 0)$, K $= \frac{2\pi}{a}(0.75, 0.75, 0)$, and L $= \frac{2\pi}{a}(0.5, 0.5, 0.5)$, where a is the lattice constant. There is an equivalent X point in an adjacent Brillouin zone at $X = \frac{2\pi}{a}(1, 1, 0)$.

dynamical matrix is Hermitian, its eigenvalues are real and its eigenvectors are orthogonal. By calculating the phonon frequencies for a range of wave vectors along a chosen crystallographic direction, phonon dispersion curves can be generated. The phonon dispersion curves along the [100], [110], and [111] directions in bulk SW Si and

bulk SW Ge are provided in Figs. 3.1(a) and 3.1(b) as examples. For each direction, the phonon frequencies were calculated for 1000 evenly spaced wave vectors, and a line was drawn through the results. The labels Γ, X, K, and L denote high-symmetry points in the Brillouin zone and are defined in the figure caption. Both Si and Ge have a two atom primitive unit cell, and therefore, there are $3 \times 2 = 6$ dispersion branches (one for each polarization). The lowest three branches are the acoustic branches, and the higher branches are the optical branches. Note that in the [100] and [111] directions, however, several of the branches are degenerate. The experimentally measured phonon dispersion curves are also provided in Fig. 3.1 for comparison [90, 91]. While the SW potential is capable of reproducing the main features of the phonon dispersion curves, it generally overpredicts the phonon frequencies and the slopes of the dispersion curves, especially near the zone boundaries (e.g., near the X-point).

3.3 Phonon group velocities

The mode-dependent phonon group velocity, $\mathbf{v}_g$, is defined as

$$\mathbf{v}_g(\boldsymbol{\kappa}, \nu) = \frac{\partial \omega(\boldsymbol{\kappa}, \nu)}{\partial \boldsymbol{\kappa}}. \tag{3.7}$$

While the group velocities can be calculated directly from the slopes of the phonon dispersion curves, a challenge is encountered with this method at the locations where the dispersion branches cross. At these locations, it is difficult to keep track of which branch corresponds to each mode. Here, this challenge is avoided by following the approach of Ref. [92] and deriving an analytical expression for the phonon group velocity in terms of the dynamical matrix and polarization vector. This expression allows one to easily keep track of the frequency, group velocity, and polarization vector that correspond to a particular mode. This ability is critical for the calculation of the phonon transmission coefficients, which is discussed in Section 3.4.

The derivation of the analytical expression for the phonon group velocity is easiest to follow by considering each component individually. The derivation for the z component of the phonon group velocity, $v_{g,z}$, is provided here. Taking the derivative of Eq. (3.4) with respect to the z component of the phonon wave vector, κ_z, results in

$$2\omega \frac{\partial \omega}{\partial \kappa_z} \mathbf{e} + \omega^2 \frac{\partial \mathbf{e}}{\partial \kappa_z} = \frac{\partial \mathbf{D}}{\partial \kappa_z} \mathbf{e} + \mathbf{D} \frac{\partial \mathbf{e}}{\partial \kappa_z}. \tag{3.8}$$

Multiplying Eq. (3.8) by $\mathbf{e}^\dagger$ from the left and simplifying using the fact that $\mathbf{e}^\dagger \cdot \mathbf{e} = 1$ yields

$$2\omega \frac{\partial \omega}{\partial \kappa_z} = \mathbf{e}^\dagger \frac{\partial \mathbf{D}}{\partial \kappa_z} \mathbf{e} + \mathbf{e}^\dagger \left(\mathbf{D} - \omega^2 \mathbf{I} \right) \frac{\partial \mathbf{e}}{\partial \kappa_z}, \tag{3.9}$$

where $\mathbf{I}$ is the identity matrix. The complex conjugate of Eq. (3.4) is

$$\mathbf{e}^\dagger \left(\mathbf{D}^\dagger - \omega^2 \mathbf{I} \right) = 0. \tag{3.10}$$

Because the dynamical matrix is Hermitian, $\mathbf{D} = \mathbf{D}^\dagger$ and Eq. (3.10) can be used to eliminate the second term on the right hand side of Eq. (3.9). Combining the result with the z component of Eq. (3.7) yields

$$v_{g,z}(\boldsymbol{\kappa}, \nu) = \frac{1}{2\omega(\boldsymbol{\kappa}, \nu)} \left[\mathbf{e}^\dagger(\boldsymbol{\kappa}, \nu) \frac{\partial \mathbf{D}(\boldsymbol{\kappa})}{\partial \kappa_z} \mathbf{e}(\boldsymbol{\kappa}, \nu) \right]. \tag{3.11}$$

3.4 Phonon transmission coefficients

3.4.1 Incident phonon

The phonon transmission coefficient is defined as the fraction of the incident phonon energy that is transmitted across a junction between two semi-infinite leads [see schematic diagram in Fig. 3.2(a)]. Here, the phonon transmission coefficients are calculated using the harmonic LD-based scattering boundary method [92–94]. In this section, the details related to the scattering boundary method are discussed and the results for an example calculation of a phonon incident on a symmetrically-strained Si/Ge interface are provided.

Semi-infinite Lead *L*   Junction   Semi-infinite Lead *R*

Reflected Phonons

Transmitted Phonons

Incident Phonon

(b)

Si Lead   Junction   Ge Lead

$a_\parallel$

$a_{\perp,Si}$ $a_{\perp,Ge}$

$a_\parallel = 5.54229$ Å
$a_{\perp,Si} = 5.31830$ Å
$a_{\perp,Ge} = 5.73527$ Å

(c)

Si Lead   Junction   Ge Lead

$a_{\perp,Si}$ $a_{\perp,Ge}$

Atomic Positions

Atom #	Element	m (10^{-26} kg)	x (Å)	y (Å)	z (Å)
1	Si	4.66371	0.00000	0.00000	0.00000
2	Si	4.66371	1.38557	1.38557	1.32958
3	Si	4.66371	2.77114	0.00000	2.65915
4	Si	4.66371	4.15671	1.38557	3.98873
5	Si	4.66371	0.00000	0.00000	5.31830
6	Si	4.66371	1.38557	1.38557	6.64644
7	Ge	12.0621	2.77114	0.00000	8.03198
8	Ge	12.0621	4.15671	1.38557	9.46786
9	Ge	12.0621	0.00000	0.00000	10.90168
10	Ge	12.0621	1.38557	1.38557	12.33550
11	Ge	12.0621	2.77114	0.00000	13.76931
12	Ge	12.0621	4.15671	1.38557	15.20313

Figure 3.2: Schematic diagrams of (a) a junction between two semi-infinite leads, and (b) the symmetrically-strained Si/Ge interface. The symmetrically-strained Si/Ge interface is defined using the junction unit cell provided in (c).

A schematic diagram of the symmetrically-strained Si/Ge interface is shown in Fig. 3.2(b). Only a portion of the interface is shown, as the leads are assumed to be semi-infinite in the calculations. The positions of atoms near the interface are set using the 12-atom "junction unit cell" shown in Fig. 3.2(c) with translational vectors $\mathbf{a}_1$ and $\mathbf{a}_2$ equal to

$$\mathbf{a}_1 = \frac{a_\parallel}{2}\,\mathbf{i} + \frac{a_\parallel}{2}\,\mathbf{j} \quad \text{and} \quad \mathbf{a}_2 = -\frac{a_\parallel}{2}\,\mathbf{i} + \frac{a_\parallel}{2}\,\mathbf{j}. \tag{3.12}$$

The positions of the lead atoms in the junction unit cell can also be defined using the primitive translational vectors for the diamond crystal lattice. The lattice constant in the directions parallel to the interface, $a_\parallel$, is equal to the average of the bulk zero-stress, zero-temperature SW Si and SW Ge lattice constants of 5.54229 Å (the bulk lattice constants are provided in Table 2.6). The lead lattice constants in the direction perpendicular to the interface, $a_\perp$, are chosen to give zero stress in that direction and are determined by minimizing the lead potential energy while keeping the parallel lattice constant fixed at $a_\parallel$. These lattice constants are 5.31830 Å and 5.73527 Å for SW Si and SW Ge. The distances between the monolayers within the junction are determined by relaxing the structure using a steepest decent approach. In these calculations, the junction contains the two monolayers on either side of the interface. Increasing the size of the junction in the z direction has negligible effect on the calculated phonon transmission coefficients.

The incident phonon chosen for the example calculation is the third lowest-frequency mode in Si [assumed to be the left lead, see Figs. 3.2(b)-3.2(c)] at a wave vector of

$$\boldsymbol{\kappa}^I = 2.0\,\mathbf{i} + 2.0\,\mathbf{j} + 2.0\,\mathbf{k}\ [\text{nm}^{-1}], \tag{3.13}$$

where the superscript I is used to denote properties of the incident phonon. Using the methodology discussed in Sections 3.2 and 3.3, the frequency, polarization vector,

Table 3.1: Frequency, wave vector, group velocity, and polarization vector of the example incident phonon. The phonon is incident on the symmetrically-strained Si/Ge interface from the Si side.

	Property	Incident Mode
	ω^I (rad/ps)	29.509
	κ_x^I (nm^{-1})	2.0000
	κ_y^I (nm^{-1})	2.0000
	κ_z^I (nm^{-1})	2.0000
	$v_{g,x}^I$ (m/s)	4818.8
	$v_{g,y}^I$ (m/s)	4818.8
	$v_{g,z}^I$ (m/s)	4726.3
	$m_{Si}^{1/2}U_x^I(1)$	-0.40791 + 0.00000i
	$m_{Si}^{1/2}U_y^I(1)$	-0.40791 + 0.00000i
$\mathbf{e}^I =$	$m_{Si}^{1/2}U_z^I(1)$	-0.40892 - 0.00110i
	$m_{Si}^{1/2}U_x^I(2)$	-0.38372 + 0.13839i
	$m_{Si}^{1/2}U_y^I(2)$	-0.38372 + 0.13839i
	$m_{Si}^{1/2}U_z^I(2)$	-0.38430 + 0.13977i

and group velocity for this incident phonon are calculated. The results are provided in Table 3.1.

3.4.2 Excited modes

When a phonon is incident on the junction, N^L modes are excited in the left lead and N^R modes are excited in the right lead. The properties of these modes are denoted using the superscripts L and R. The first step in calculating the phonon transmission coefficient is to identify the frequency, polarization vector, and group velocity (if applicable) of each excited mode.

The Si and Ge leads at the Si/Ge interface are "similar," meaning that the crystal lattices of each lead are identical and are not misoriented with respect to one another [95]. For these systems, the x and y components of the wave vectors of the excited modes, κ_x and κ_y, must be equal to the values for the incident mode due to the

Table 3.2: Frequency, wave vector, group velocity, polarization vector, and amplitude of each mode excited by the example incident phonon in the left lead.

	Property	Mode $L1$	Mode $L2$	Mode $L3$
	ω^L (rad/ps)	29.509	29.509	29.509
	κ_x^L (nm^{-1})	2.0000	2.0000	2.0000
	κ_y^L (nm^{-1})	2.0000	2.0000	2.0000
	κ_z^L (nm^{-1})	-2.0000	-6.3197	-5.9924
	$v_{g,x}^L$ (m/s)	4818.8	187.40	374.03
	$v_{g,y}^L$ (m/s)	4818.8	187.40	374.03
	$v_{g,z}^L$ (m/s)	-4726.3	-3332.9	-4673.4
	$m_{Si}^{1/2}U_x^L(1)$	-0.40791 + 0.00000i	-0.50000 + 0.00000i	0.41475 + 0.00000i
	$m_{Si}^{1/2}U_y^L(1)$	-0.40791 + 0.00000i	0.50000 + 0.00000i	0.41475 + 0.00000i
$\mathbf{e}^L =$	$m_{Si}^{1/2}U_z^L(1)$	0.40892 - 0.00110i	0.00000 + 0.00000i	0.36623 + 0.14781i
	$m_{Si}^{1/2}U_x^L(2)$	-0.38372 - 0.13839i	-0.39803 + 0.30261i	0.38694 + 0.14930i
	$m_{Si}^{1/2}U_y^L(2)$	-0.38372 - 0.13839i	0.39803 - 0.30261i	0.38694 + 0.14930i
	$m_{Si}^{1/2}U_z^L(2)$	0.38430 + 0.13977i	0.00000 + 0.00000i	0.39489 - 0.00607i
	$\mathcal{L}$	-0.14282 + 0.05976i	0.00000 + 0.00000i	0.35647 - 0.17000i

translational invariance of the system in these directions [53, 95], i.e.,

$$\kappa_x^L = \kappa_x^R = \kappa_x^I \tag{3.14}$$

$$\kappa_y^L = \kappa_y^R = \kappa_y^I.$$

For systems with "dissimilar" leads (e.g., interfaces between solids with different crystal lattices and grain boundaries), Eq. (3.14) is not appropriate. The relationship between the x and y components of the incident and excited mode wave vectors for such systems is discussed by Pettersson and Mahan [95].

Because inelastic processes cannot occur under the harmonic approximation, the incident phonon can only excite phonons with the same frequency (i.e., the scattering event is elastic). The z component of the wave vector of each excited mode must therefore satisfy [95]

$$\omega\big(\kappa_x^L, \kappa_y^L, \kappa_z^L\big) = \omega\big(\kappa_x^R, \kappa_y^R, \kappa_z^R\big) = \omega\big(\kappa_x^I, \kappa_y^I, \kappa_z^I\big). \tag{3.15}$$

Table 3.3: Frequency, wave vector, group velocity, polarization vector, and amplitude of each mode excited by the example incident phonon in the right lead.

	Property	Mode $R1$	Mode $R2$	Mode $R3$
	ω^R (rad/ps)	29.509	29.509	29.509
	κ_x^R (nm^{-1})	2.0000	2.0000	2.0000
	κ_y^R (nm^{-1})	2.0000	2.0000	2.0000
	κ_z^R (nm^{-1})	5.1265	8.6301	$10.9553 + 2.0508i$
	v_x^R (m/s)	1946.0	995.11	-
	v_y^R (m/s)	1946.0	995.11	-
	v_z^R (m/s)	3493.7	2491.7	-
$\mathbf{e}^R =$	$m_{Ge}^{1/2}U_x^R(1)$	$0.30765 + 0.00000i$	$0.46198 + 0.00000i$	$0.42026 - 0.44781i$
	$m_{Ge}^{1/2}U_y^R(1)$	$0.30765 + 0.00000i$	$0.46198 + 0.00000i$	$-0.42195 + 0.44508i$
	$m_{Ge}^{1/2}U_z^R(1)$	$0.52716 - 0.18112i$	$-0.21174 + 0.16828i$	$0.00191 - 0.00118i$
	$m_{Ge}^{1/2}U_x^R(2)$	$0.22046 - 0.21459i$	$0.32372 - 0.32959i$	$0.25097 + 0.24374i$
	$m_{Ge}^{1/2}U_y^R(2)$	$0.22046 - 0.21459i$	$0.32372 - 0.32959i$	$-0.25995 - 0.23818i$
	$m_{Ge}^{1/2}U_z^R(2)$	$0.50408 - 0.23791i$	$-0.26843 + 0.03315i$	$0.00080 + 0.00129i$
	$\mathcal{R}$	$-1.0453 - 0.26143i$	$-0.22051 - 0.06741i$	$0.00000 - 0.00000i$

A convenient method to solve for the values of κ_z^L and κ_z^R that satisfy Eq. (3.15) is described by Zhao and Freund [53]. This method is based on an alternative definition of the eigenvalue problem [Eq. (3.4)], which is

$$\omega^2(\boldsymbol{\kappa}, \nu)\tilde{\mathbf{e}}(\boldsymbol{\kappa}, \nu) = \tilde{\mathbf{D}}(\boldsymbol{\kappa})\tilde{\mathbf{e}}(\boldsymbol{\kappa}, \nu), \tag{3.16}$$

where the sub-matrices of $\tilde{\mathbf{D}}$ are

$$\tilde{\mathbf{D}}_{jj'}(\boldsymbol{\kappa}) = \frac{1}{(m_j m_{j'})^{1/2}} \sum_{k'} \boldsymbol{\Psi}(11, 1k') \exp(i\boldsymbol{\kappa} \cdot \mathbf{r}_{11}^{1k'}). \tag{3.17}$$

Here, the extra 1 compared to Eq. (3.5) denotes the reference atom in the unit cell. The eigenvalues of $\tilde{\mathbf{D}}$ and $\mathbf{D}$ are the same, but the eigenvectors of $\tilde{\mathbf{D}}$ and $\mathbf{D}$ differ by a phase factor [38, 88], i.e.,

$$\mathbf{e}(\boldsymbol{\kappa}, \nu) = \tilde{\mathbf{e}}(\boldsymbol{\kappa}, \nu) \exp(-i\boldsymbol{\kappa} \cdot \mathbf{r}_{11}^{j1}). \tag{3.18}$$

Zhao and Freund noted that due to the short range nature of the SW potential, the only nonzero terms in the summation of Eq. (3.17) have $r_{11,z}^{1k'}$ equal to $-a_\perp/2$, 0,

46

or $+a_\perp/2$, where $\mathbf{r}_{11}^{1k'} = r_{11,x}^{1k'}\mathbf{i} + r_{11,y}^{1k'}\mathbf{j} + r_{11,z}^{1k'}\mathbf{k}$. The matrix $\tilde{\mathbf{D}}$ can therefore be divided into three separate $3n \times 3n$ matrices,

$$\tilde{\mathbf{D}} = \varsigma^{-1}\tilde{\mathbf{D}}_- + \tilde{\mathbf{D}}_0 + \varsigma\tilde{\mathbf{D}}_+, \tag{3.19}$$

where

$$\varsigma = \exp\left(i\frac{\kappa_z a_\perp}{2}\right). \tag{3.20}$$

Similar to the definition of the dynamical matrix, the matrices $\tilde{\mathbf{D}}_-$, $\tilde{\mathbf{D}}_0$, and $\tilde{\mathbf{D}}_+$ are each comprised of n^2 3×3 sub-matrices. For $\tilde{\mathbf{D}}_-$, the sub-matrices are

$$\tilde{\mathbf{D}}_{jj'-} = \frac{1}{(m_j m_{j'})^{1/2}} \sum_{k'} \mathbf{\Psi}(11, 1k') \exp[i(\kappa_x r_{11,x}^{1k'} + \kappa_y r_{11,y}^{1k'})]\delta, \tag{3.21}$$

where δ is the Kronecker delta function and is equal to one if $r_{11,z}^{1k'} = -a_\perp/2$ and zero otherwise. The definitions for $\tilde{\mathbf{D}}_0$ and $\tilde{\mathbf{D}}_+$ are similar (i.e., the matrix $\tilde{\mathbf{D}}_0$ contains the $r_{11,z}^{1k'} = 0$ terms and the matrix $\tilde{\mathbf{D}}_+$ contains the $r_{11,z}^{1k'} = a_\perp/2$ terms).

Substituting Eq. (3.19) into Eq. (3.16) yields

$$(\omega^I)^2\tilde{\mathbf{e}} = \left(\varsigma^{-1}\tilde{\mathbf{D}}_- + \tilde{\mathbf{D}}_0 + \varsigma\tilde{\mathbf{D}}_+\right)\tilde{\mathbf{e}}, \tag{3.22}$$

which is a generalized nonlinear eigensystem for ς. This generalized nonlinear eigensystem can be converted to a generalized linear eigensystem through a vector substitution of $\boldsymbol{\zeta} = \varsigma\tilde{\mathbf{e}}$. The resulting generalized linear eigensystem is

$$\begin{bmatrix} \tilde{\mathbf{D}}_- & 0 \\ 0 & \mathbf{I} \end{bmatrix}\begin{bmatrix} \tilde{\mathbf{e}} \\ \boldsymbol{\zeta} \end{bmatrix} = \varsigma\begin{bmatrix} \omega^2\mathbf{I} - \tilde{\mathbf{D}}_0 & -\tilde{\mathbf{D}}_+ \\ \mathbf{I} & 0 \end{bmatrix}\begin{bmatrix} \tilde{\mathbf{e}} \\ \boldsymbol{\zeta} \end{bmatrix}. \tag{3.23}$$

Equation (3.23) is converted to a standard eigenvalue problem by multiplying it by the inverse of the matrix on the right hand side, i.e.,

$$\begin{bmatrix} \omega^2\mathbf{I} - \tilde{\mathbf{D}}_0 & -\tilde{\mathbf{D}}_+ \\ \mathbf{I} & 0 \end{bmatrix}^{-1}\begin{bmatrix} \tilde{\mathbf{D}}_- & 0 \\ 0 & \mathbf{I} \end{bmatrix}\begin{bmatrix} \tilde{\mathbf{e}} \\ \boldsymbol{\zeta} \end{bmatrix} = \varsigma\begin{bmatrix} \tilde{\mathbf{e}} \\ \boldsymbol{\zeta} \end{bmatrix}. \tag{3.24}$$

The values of κ_z that satisfy Eq. (3.15) are calculated from the eigenvalues of Eq. (3.24) using Eq. (3.20). For each lead, there are $2 \times 3 \times n$ eigenvalues. The eigenvalues with $|\varsigma| = 1$ correspond to phonon modes that have only real components for κ_z. Of these modes, only the half that propagate away from the junction are physically realistic. The eigenvalues with $|\varsigma| \neq 1$ correspond to evanescent modes that have complex κ_z and do not propagate. Of these modes, only the half that decay to zero away from the junction are physically realistic. As discussed by Zhao and Freund [53], when $\mathbf{D}_-$ or $\mathbf{D}_+$ is singular, some of the eigenvalues have $|\varsigma| = 0$ or $|\varsigma| = \infty$. These eigenvalues correspond to evanescent modes with associated atomic vibrations that decay immediately to zero on either side of the junction and are thus neglected.

The physically realistic values of κ_z^L and κ_z^R for the modes excited by the example incident phonon are provided in Tables 3.2 and 3.3. For each excited evanescent mode (e.g., mode $R3$ in Table 3.3), the polarization vector $\mathbf{e}$ is calculated by converting the $\tilde{\mathbf{e}}$ component of the associated eigenvector of Eq. (3.24) using Eq. (3.18). Because evanescent modes do not propagate, no group velocity is provided for these modes. For each excited phonon mode, the group velocity and polarization vector are calculated by solving the eigenvalue problem given by Eq. (3.4) and selecting the mode with the same frequency as the incident phonon. This approach ensures that if there are any degeneracies amongst the excited modes then their polarization vectors will be orthogonal to one another.[3] The polarization vectors and group velocities of the excited modes are also provided in Tables 3.2 and 3.3.

---

[3]The eigenvectors of Eq. (3.24) are not necessarily orthogonal to one another because the product of the two matrices on the left hand side of Eq. (3.24) is not Hermitian.

3.4.3 Amplitudes of the excited modes

The next step in calculating the phonon transmission coefficient is to determine the amplitude of each excited mode. Assuming that the incident phonon has an amplitude of unity, the complex displacement vector, $\boldsymbol{u}$,[4] of the jth atom in the kth primitive unit cell in the left lead can be expressed as a superposition over the incident mode and the excited modes in the left lead, i.e.,

$$\boldsymbol{u}_{jk} = \mathbf{U}^I(j)\exp[i\boldsymbol{\kappa}^I \cdot \mathbf{r}(jk)] + \sum_L^{N^L} \mathcal{L}^L \mathbf{U}^L(j)\exp[i\boldsymbol{\kappa}^L \cdot \mathbf{r}(jk)], \qquad (3.25)$$

where $\mathcal{L}^L$ is the amplitude of excited mode L. Similarly, the displacement of the jth atom in the kth primitive cell in the right lead is

$$\boldsymbol{u}_{jk} = \sum_R^{N^R} \mathcal{R}^R \mathbf{U}^R(j)\exp[i\boldsymbol{\kappa}^R \cdot \mathbf{r}(jk)], \qquad (3.26)$$

where $\mathcal{R}^R$ is the amplitude of excited mode R. Equations (3.25) and (3.26) are referred to as the "scattering boundary equations" and fully describe the lead dynamics associated with the scattering process with only $N^L + N^R$ unknowns.

The amplitudes of the excited modes are determined by coupling the dynamics of atoms in the left and right leads through the equations of motion of atoms near the junction. Under the harmonic approximation, the equation of motion at ω^I for the lth atom in the pth junction unit cell is

$$m_l(\omega^I)^2 \boldsymbol{u}_{lp} = \sum_{l'}\sum_{p'} \boldsymbol{\Psi}(lp, l'p')\boldsymbol{u}_{l'p}\exp[i(\kappa_x^I r_{lp,x}^{l'p'} + \kappa_y^I r_{lp,y}^{l'p'})], \qquad (3.27)$$

where the summation is over all atoms. The displacement amplitude vector $\boldsymbol{u}$ for each atom in the junction unit cell and the amplitude of each excited mode are determined by solving a linear system of equations. This system of equations is composed of (i)

---

[4]$\boldsymbol{u}$ is related to $\mathbf{u}$ by

$$\mathbf{u} = \boldsymbol{u}\exp(-i\omega t).$$

an equation of motion [Eq. (3.27)] for each atom in the reference junction unit cell that is either in or interacts[5] with the junction [atoms 3-10 in Fig. 3.2(c)], and (ii) a scattering boundary equation [Eq. (3.25) or Eq. (3.26)] for each lead atom that appears in these equations of motion [atoms 1-4 and 9-12 in Fig. 3.2(c)]. Because this system of equations may contain more equations than unknowns, it is solved using singular value decomposition. The amplitude of each mode excited by the example incident phonon is provided in Tables 3.2 and 3.3.

Once the excited mode amplitudes are found, the phonon transmission coefficient is calculated from [92]

$$\alpha_{L \to R} = \sum_R^{N^R} |\mathcal{R}^R|^2 \frac{v_{g,z}^R}{v_{g,z}^I} \frac{a_\perp^L}{a_\perp^R}, \tag{3.28}$$

where the summation is over the excited phonon modes in the right lead. Evanescent modes are not included in the summation in Eq. (3.28) because they do not propagate, and thus, cannot carry energy away from the junction.

A useful check that the scattering boundary method is correctly implemented is to add the phonon transmission coefficient to the phonon reflection coefficient, $\rho_{L \to R}$, which is

$$\rho_{L \to R} = \sum_L^{N^L} |\mathcal{L}^L|^2 \frac{v_{g,z}^L}{v_{g,z}^I} \frac{a_\perp^L}{a_\perp^L}, \tag{3.29}$$

and check that $\alpha_{L \to R} + \rho_{L \to R} = 1$, as required by conservation of energy. For the example incident phonon described in Table 3.1, $\alpha_{L \to R}$ and $\rho_{L \to R}$ are 0.82186 and 0.17820 and energy is conserved to within 0.01%.

3.4.4 Comparison to wave-packet simulations

As further verification of the code implementation, phonon transmission coeffi-cients calculated using the scattering boundary method are compared to those pre-

---

[5]A pair of atoms is said to interact when there are nonzero components in $\boldsymbol{\Psi}$.
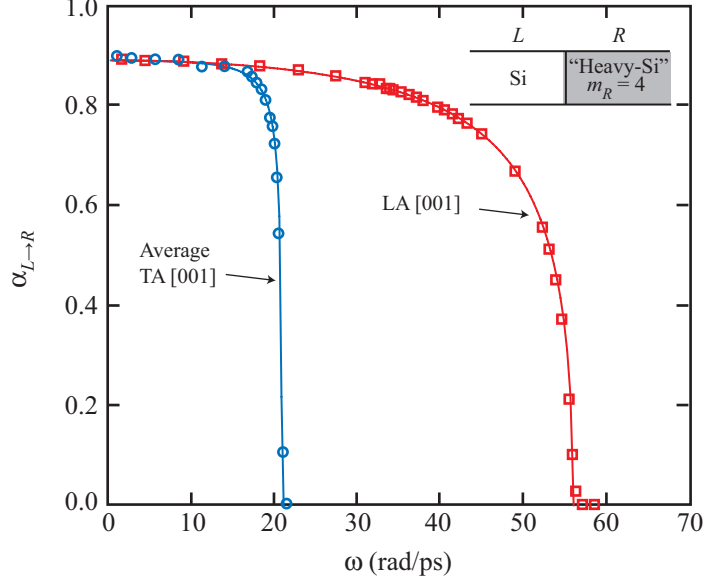
Figure 3.3: Comparison between the phonon transmission coefficients predicted by Schelling *et al.* [86] using wave-packet simulations (points) and calculated using the scattering boundary method (lines). Data are provided for [001] transverse acoustic (TA) and longitudinal acoustic (LA) phonons incident on the Si/heavy-Si, $m_R = 4$ interface from the Si side.

dicted by Schelling and co-workers using the MD-based wave-packet method [54, 86]. In the wave-packet method, all of the atoms are initially located at their zero-temperature equilibrium positions and a spatially localized phonon wave-packet is launched at the interface. The phonon transmission coefficient is determined by dividing the total energy (potential and kinetic) on the transmitted side of the interface after the scattering event by the initial energy of the wave-packet. This method requires on the order of one processor hour to predict a single phonon transmission coefficient, compared to less than a second for the scattering boundary method.

The phonon transmission coefficients predicted using the wave-packet and scattering boundary methods for [001] transverse acoustic (TA) and longitudinal acoustic (LA) phonons incident on an interface between Si and a species that differs from Si only in mass ("heavy-Si") by a ratio of four are provided in Fig. 3.3. The phonons are incident on the interface from the Si side. For transverse phonons, the phonon trans-

mission coefficient is dependent on polarization [86]. The results shown in Fig. 3.3 correspond to the average of the two transverse acoustic branches. The predictions of both methods are in excellent agreement, giving confidence to the implementation of the scattering boundary method. This agreement also suggests that the degree of phonon localization does not affect the transmission coefficient of phonons incident on an isolated interface (the phonons are spatially delocalized in the scattering boundary method). As discussed by Schelling and Phillpot, however, the transmission coefficients for phonons incident on a thin film are dependent on the degree of phonon localization [54]. This point is discussed further in Chapter V.

3.5   Summary

Theoretical calculation of thermal boundary resistance and thin film thermal resistance requires knowledge of the frequency, group velocity, and transmission coefficient for each phonon mode on either side of the interface or thin film. In this chapter, the methodology for predicting these quantities was provided. To avoid a challenge associated with numerically calculating phonon group velocities from phonon dispersion curves, an analytical expression for the phonon group velocity was derived. The full details related to the calculation of the transmission coefficient for a phonon incident on an isolated interface were provided. The phonon transmission coefficients calculated using this method are found to be in excellent agreement with those calculated using the MD-based wave-packet method.

CHAPTER IV

Thermal boundary resistance predictions from molecular dynamics simulations and theoretical calculations

4.1 Introduction

4.1.1 Background

The scattering of thermal energy carriers (i.e., electrons and phonons) at an interface between two solids results in a thermal boundary resistance [9]. An ability to accurately predict thermal boundary resistance (or its inverse, the thermal boundary conductance) is valuable in the thermal analysis of devices and materials in which the interface separation is on the same scale as the carrier mean free paths. As discussed in Section 1.1, examples of these devices and materials include quantum cascade lasers, CMOS transistors, and semiconductor superlattices.

The most commonly applied theoretical models for predicting thermal boundary resistance are the acoustic mismatch model (AMM) and the diffuse mismatch model (DMM) [9, 96]. At temperatures less than $\sim$30 K, the AMM and DMM predict similar values for the thermal boundary resistance that are in reasonable agreement with experimental measurements [9]. At typical application temperatures, however, assumptions in the AMM and DMM make their predictions inaccurate. Both models assume that the thermal transport is dominated by phonons, which is valid for interfaces between dielectrics or lightly doped semiconductors. There are differing

views, however, on the role of electron-phonon coupling at metal/dielectric interfaces [97–102], to which all of the experimental data correspond due to metrological limitations. In the DMM, the phonon interface scattering is assumed to be diffuse (i.e., the incident phonon loses all memory of its direction and polarization) while the AMM assumes that there is no probability of diffuse scattering (i.e., specular scattering). The actual degree of specular and diffuse scattering is dependent on the interface quality [9, 38, 79], which is often known only qualitatively. In addition, both models neglect the atomic-level detail of the interface and are usually applied under the Debye approximation of linear and isotropic phonon dispersion curves [103–109]. These two assumptions lead to inaccuracy at temperatures where phonons with wavelengths on the same scale as the interatomic spacing are excited [110]. Furthermore, both the AMM and DMM assume that the phonon interface scattering is elastic (i.e., the reflected and transmitted phonons have the same frequency as the incident phonon). This assumption leads to a prediction of (i) a constant thermal boundary resistance in the classical limit,[1] and (ii) a lower bound on the thermal boundary resistance known as the phonon radiation limit [9, 97, 111, 112]. Contrary to these predictions, a thermal boundary resistance that decreases with increasing temperature in the classical limit [99, 105, 106], and values below the phonon radiation limit [97, 99, 112], have been experimentally measured. These results have been attributed to the presence of inelastic phonon scattering at the interface.

One approach for developing improved models for thermal boundary resistance is to modify the AMM or DMM to include phenomena neglected in the original models (e.g., phonon scattering near the interface [107], inelastic interface scattering

---

[1]The classical limit is reached when the equilibrium phonon distribution [Eq. (4.4)] is well-approximated by $f_{\mathrm{BE}} = k_{\mathrm{B}}T/\hbar\omega$. This condition is met in experiment at high temperatures (above the Debye temperature) and in classical MD simulations at all temperatures.

[113], interface disorder [103,104], and electron-phonon coupling [98,100]). While the predictions of the modified models are generally in better agreement with experiment than the original AMM or DMM, they have only been applied under the Debye approximation and in some cases require fitting parameters [107]. The enhanced agreement with experiment may therefore be fortuitous. An alternative approach, and the one used here, is to use atomic-level methods such as MD simulations and LD calculations to better understand the phonon transport physics. In this way, models can be developed based on justifiable assumptions.

4.1.2 Objective

Despite over five decades of research, a robust model for the thermal boundary resistance has remained elusive [9,96]. One reason for the slow development of such a model is the many sources of uncertainty when comparing theoretical predictions and experimental measurements (e.g., the roles of electron-phonon coupling, interface quality, and inelastic phonon scattering). The objective of this chapter is to assess the theory for thermal transport by phonons across an interface by eliminating these sources of uncertainty. This objective is achieved by evaluating theoretical expressions for the thermal boundary resistance using phonon properties obtained from harmonic LD calculations and comparing the results to independent MD-predicted values in a self-consistent manner. In both the theoretical and MD predictions, there is no electronic contribution to the thermal transport. The predictions are compared for perfect interfaces between two crystals that contain no defects. The theoretical expressions are evaluated in the classical limit, as required for the validity of the MD simulations. In addition, the comparison is performed at temperatures where the phonon interface scattering is demonstrated to be elastic, as required for the validity
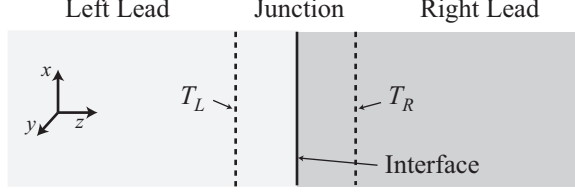
Figure 4.1: Schematic diagram of an interface between two semi-infinite leads. Under the assumption of no inelastic scattering within the junction, the thermal boundary resistance is equal to the junction thermal resistance. Reprinted with permission from Ref. [26], Copyright 2009 American Physical Society.

of the LD-based calculations.

Two types of interface are considered: (i) a symmetrically-strained Si/Ge interface, and (ii) a series of interfaces between Si and a species referred to as "heavy-Si," which differs from Si only in mass by a ratio of m_R. For the Si/heavy-Si interfaces, mass ratios between 1 and 6 are considered. For comparison, the mass ratio between Ge and Si is 2.6. Each interface is oriented along the (001) crystallographic plane (see coordinate system in Fig. 4.1).

4.2 Thermal transport across an interface

4.2.1 Overview

In this section, the theory for thermal transport by phonons across an interface is reviewed. To increase the generality of the discussion, the theory is described for a system containing a junction between two semi-infinite solids (i.e., leads), as shown in Fig. 4.1 for the case where the junction contains a single interface. This theory has been applied to predict the thermal resistance of a variety of junction types, including dielectric quantum wires [114], carbon nanotubes [115], grain boundaries [116, 117], and interfaces [53, 94, 95, 110, 118, 119].

Two expressions for the junction thermal resistance, R, will be developed. The

junction thermal resistance is defined as

$$R = \frac{T_L - T_R}{q},$$ (4.1)

where q is the heat flux across the junction, and T_L and T_R are the temperatures at the lead/junction boundaries. These expressions will be evaluated using phonon properties predicting from harmonic LD calculations, which assume that there is no inelastic scattering within the junction (see Section 3.4). Under this assumption, the thermal boundary resistance, which is defined in terms of the temperature drop across the interface, is equal to the junction thermal resistance, regardless of the junction width.

Each lead emits phonons to and absorbs phonons from the junction. At steady-state, the net heat flux across the junction is

$$
\begin{aligned}
q &= \frac{1}{(2\pi)^3} \int_L \sum_\nu^+ \hbar\omega(\boldsymbol{\kappa},\nu) v_{g,z}(\boldsymbol{\kappa},\nu) \alpha_{L\to R}(\boldsymbol{\kappa},\nu) f_L(\boldsymbol{\kappa},\nu) d\boldsymbol{\kappa} \\
&+ \frac{1}{(2\pi)^3} \int_R \sum_\nu^- \hbar\omega(\boldsymbol{\kappa},\nu) v_{g,z}(\boldsymbol{\kappa},\nu) \alpha_{R\to L}(\boldsymbol{\kappa},\nu) f_R(\boldsymbol{\kappa},\nu) d\boldsymbol{\kappa},
\end{aligned}
$$ (4.2)

where L and R denote the left and right leads, and $\hbar$ is the Planck constant divided by 2π. The first (second) integral is over the first Brillouin zone of the left (right) lead, and the first (second) summation is over phonons moving in the positive (negative) z direction. The variables f_L and f_R are the mode-dependent phonon distributions functions in the left and right leads at the lead/junction boundaries. These distributions can be written as

$$
\begin{aligned}
f_L(\boldsymbol{\kappa},\nu) &= f_{\mathrm{BE}}[\omega(\boldsymbol{\kappa},\nu), T_L] + f_L'(\boldsymbol{\kappa},\nu) \\
f_R(\boldsymbol{\kappa},\nu) &= f_{\mathrm{BE}}[\omega(\boldsymbol{\kappa},\nu), T_R] + f_R'(\boldsymbol{\kappa},\nu),
\end{aligned}
$$ (4.3)

where f_{BE} is the equilibrium Bose-Einstein distribution function, and f_L' and f_R' are

57

the deviations from the equilibrium distribution. The equilibrium distribution is

$$f_{\text{BE}}(\omega, T) = \left[\exp\left(\frac{\hbar\omega}{k_{\text{B}}T} \right) - 1 \right]^{-1},$$

(4.4)

where k_{B} is the Boltzmann constant. Here, the temperature of a nonequilibrium system is defined to be that of an equilibrium system with the same kinetic energy [38,118]. The temperatures at the lead/junction boundaries are therefore equal to T_L and T_R if

$$\frac{1}{(2\pi)^3} \int \sum_\nu \hbar\omega f' d\boldsymbol{\kappa} = 0$$

(4.5)

in each lead.

4.2.2 Junction thermal resistance

R_E

The first expression that is derived for the junction thermal resistance is analogous to the Landauer formula for electron transport [92], and is based on the assumption that each lead is an infinite thermal reservoir held in equilibrium at a uniform temperature. Under this assumption, $f'_L = f'_R = 0$ for all modes, and Eq. (4.2) becomes

$$q = \frac{1}{(2\pi)^3} \int_L \sum_\nu^+ \hbar\omega v_{g,z} \alpha_{L\to R} f_{\text{BE}}(\omega, T_L) d\boldsymbol{\kappa} + \frac{1}{(2\pi)^3} \int_R \sum_\nu^- \hbar\omega v_{g,z} \alpha_{R\to L} f_{\text{BE}}(\omega, T_R) d\boldsymbol{\kappa}.$$

(4.6)

When $T_L = T_R$, the two terms on the right hand side of Eq. (4.6) must cancel to give zero heat flux at thermal equilibrium. This condition allows Eq. (4.6) to be simplified to involve integration over just one of the leads. For example, if both leads are at a temperature of T_R,

$$\frac{1}{(2\pi)^3} \int_R \sum_\nu^- \hbar\omega v_{g,z} \alpha_{R\to L} f_{\text{BE}}(\omega, T_R) d\boldsymbol{\kappa} = -\frac{1}{(2\pi)^3} \int_L \sum_\nu^+ \hbar\omega v_{g,z} \alpha_{L\to R} f_{\text{BE}}(\omega, T_R) d\boldsymbol{\kappa},$$

(4.7)

allowing Eq. (4.6) to be simplified to

$$q = \frac{1}{(2\pi)^3} \int_L \sum_{\nu}^{+} \hbar\omega v_{g,z} \alpha_{L \to R} [f_{\text{BE}}(\omega, T_L) - f_{\text{BE}}(\omega, T_R)] d\boldsymbol{\kappa}. \qquad (4.8)$$

In writing Eq. (4.8), the phonon properties have been assumed to be temperature-independent between temperatures of T_L and T_R. After substituting Eq. (4.8) into Eq. (4.1), and expanding $f_{\text{BE}}(\omega, T_L) - f_{\text{BE}}(\omega, T_R)$ using a first-order Taylor series, the thermal resistance is found to be

$$R_E = \left[\frac{1}{(2\pi)^3} \int_L \sum_{\nu}^{+} \hbar\omega v_{g,z} \alpha_{L \to R} \frac{\partial f_{\text{BE}}}{\partial T} d\boldsymbol{\kappa} \right]^{-1}, \qquad (4.9)$$

where the subscript E denotes that the phonons in the leads follow the equilibrium distribution function, Eq. (4.4).

Due to its simplicity, Eq. (4.9) is the most commonly applied expression for calculating thermal resistance [53, 94, 95, 110, 116–119]. It is well known, however, that this expression is inaccurate when the average phonon transmission coefficient approaches unity [9, 120]. For example, when Eq. (4.9) is applied to a perfect crystal (i.e., a system containing no interface), $\alpha_{L \to R} = 1$ for all phonon modes, and the incorrect result of a nonzero thermal resistance is predicted. The theory underlying Eq. (4.9) also contains an inconsistency, as it suggests that at steady-state, there is simultaneously zero heat flux within the leads (where there is no temperature gradient) and a non-zero heat flux across the junction [96, 120]. This inconsistency and the erroneous prediction for the no-interface case both result from the assumption that f'_L and f'_R are equal to zero [120].

R_{NE}

Following the approach of Simons [120], an expression is now derived for the junction thermal resistance that is valid for nonequilibrium phonon distributions in each

lead, which is denoted by R_{NE}. The resulting expression is more general than that given by Simons, however, because the Debye approximation for the phonon dispersion will not be made. The thermal resistance is found by substituting Eq. (4.2) into Eq. (4.1) [using the general forms for f_L and f_R given in Eq. (4.3)], and simplifying using a procedure similar to that described in the development of Eq. (4.9). The resulting expression is

$$R_{NE} = \gamma R_E, \tag{4.10}$$

where

$$\gamma = 1 - \frac{1}{(2\pi)^3} \int_L \sum_\nu^+ \beta_L \alpha_{L \to R} d\boldsymbol{\kappa} - \frac{1}{(2\pi)^3} \int_R \sum_\nu^- \beta_R \alpha_{R \to L} d\boldsymbol{\kappa}, \tag{4.11}$$

and β is the fraction of the total heat flux carried by a specific phonon mode in the lead, given by

$$\beta = \frac{\hbar \omega v_{g,z} f'}{q}. \tag{4.12}$$

For the case where no interface is present, $\alpha_{L \to R} = 1$ for all phonon modes and both terms involving integrals in Eq. (4.11) are equal to 1/2, leading to the correct result of zero thermal resistance.

To evaluate R_{NE} for a general system, the mode-dependent deviations from the equilibrium phonon distributions, f', which appear in Eq. (4.12) need to be specified. This specification can be done by solving the BTE. Exact solution of the BTE is challenging for the lead/junction/lead system, however, because the phonon distributions in the leads are coupled due to energy transmission across the junction. To simplify the solution procedure, the approach of Chen [121] is followed by assuming that the phonon distribution in each lead near the junction is bulk-like, allowing the BTE to be solved independently for each lead. The accuracy of this assumption is discussed in Section 4.4.

For a system of phonons subject to a temperature gradient in one-dimension, the steady-state BTE for a specific phonon mode takes the form [38]

$$v_{g,z}\frac{\partial f}{\partial z} = \left(\frac{\partial f}{\partial t}\right)_{\text{coll}}, \tag{4.13}$$

where $(\partial f/\partial t)_{\text{coll}}$ is the collision term, which describes the rate of change of the phonon distribution due to phonon scattering. The relaxation time approximation is applied by writing the collision term as

$$\left(\frac{\partial f}{\partial t}\right)_{\text{coll}} = -\frac{f'}{\tau}, \tag{4.14}$$

where τ is the phonon relaxation time. It is also assumed that f' is independent of temperature so that

$$\frac{\partial f}{\partial z} = \frac{\partial f}{\partial T}\frac{\partial T}{\partial z} = \frac{\partial f_{\text{BE}}}{\partial T}\frac{\partial T}{\partial z}. \tag{4.15}$$

After substituting Eqs. (4.14) and (4.15) into Eq. (4.13), f' is found to be

$$f' = -v_{g,z}\tau\frac{\partial f_{\text{BE}}}{\partial T}\frac{\partial T}{\partial z}. \tag{4.16}$$

Using this result and the Fourier law [Eq. (2.22)], Eq. (4.12) can be rewritten as

$$\beta = \frac{\hbar\omega v_{g,z}^2 \tau}{k}\frac{\partial f_{\text{BE}}}{\partial T}, \tag{4.17}$$

where the thermal conductivity, k, is given by[2]

$$k = \frac{1}{(2\pi)^3}\int\sum_{\nu}\hbar\omega v_{g,z}^2\tau\frac{\partial f_{\text{BE}}}{\partial T}d\boldsymbol{\kappa}. \tag{4.18}$$

When f' is specified using the approach described in this section and the lead species are identical, Eq. (4.10) can be reduced to the inverse of the formula provided

---

[2]An alternative expression for the thermal conductivity is given in Appendix B [Eq. (B.2)]. This equation is equivalent to Eq. (4.18) because

$$c_{ph} = \hbar\omega\frac{\partial f_{\text{BE}}}{\partial T},$$

where c_{ph} is the volumetric specific heat per phonon mode.
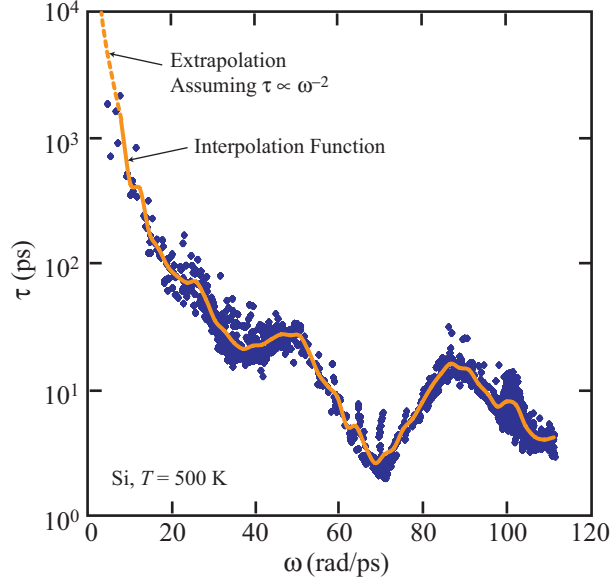
Figure 4.2: Classical phonon relaxation times in the first Brillouin zone for SW Si predicted using anharmonic LD calculations at a temperature of 500 K. Reprinted with permission from Ref. [26], Copyright 2009 American Physical Society.

by Aubry *et al.* for the thermal conductance of a grain boundary [117]. In arriving at their expression, Aubry *et al.* take the temperature associated with an incident phonon to be the local temperature at a distance of $v_{g,z}\tau$ (i.e., one mean free path) from the grain boundary instead of T_L or T_R. The development presented here, which mirrors that of Simons [120], has two advantages over this approach. First, the assumptions made in arriving at Eq. (4.16) for f' are easily identified, allowing an avenue for further investigation into sources of inaccuracy. Second, this approach can be used to specify f' for phonons moving away from the junction, allowing for a consistent definition for T_L and T_R to be maintained [see discussion preceding Eq. (4.5)].

4.3 Predicting the thermal boundary resistance

4.3.1 Theoretical evaluation of R_E and R_{NE}

The theoretical expressions for the thermal boundary resistance [Eqs. (4.9) and (4.10)] are evaluated using Monte Carlo integration with 10^5 random phonon wavevectors in the first Brillouin zone of each lead, where the lead is defined using the two-atom diamond primitive cell. This level of Brillouin zone-sampling results in a prediction uncertainty of $\pm 2\%$. For comparison to the classical MD predictions, R_E and R_{NE} are evaluated in the classical limit by setting $f_{\mathrm{BE}} = k_{\mathrm{B}}T/\hbar\omega$. At each wavevector, the frequencies and group velocities are obtained using LD calculations applied under the harmonic approximation (see Sections 3.2 and 3.3). The phonon transmission coefficients are obtained using the harmonic LD-based scattering boundary method discussed in Section 3.4, which assumes that the phonon interface scattering is specular and elastic. The assumption of specular scattering is valid for perfect interfaces because they contain no defects or roughness that would promote diffuse scattering [9,38]. In Section 4.4.1, the phonon interface scattering is demonstrated to be elastic at the Si/Ge interface at temperatures less than or equal to $\sim$500 K.

The phonon relaxation times are calculated using an anharmonic LD-based method [75,89]. For all phonon modes, the calculated relaxation time is proportional to T^{-1} to within 5% accuracy between temperatures of 300 K and 1000 K. In addition, at a fixed temperature, the relaxation times can be approximated as a function of frequency alone, as shown in Fig. 4.2 for SW Si at a temperature of 500 K. Based on these observations, a linear interpolation function is generated using the GNU Scientific Library [122] for each species based on the calculated relaxation times at a temperature of 500 K. These interpolation functions are used with the T^{-1} proportionality to specify the relaxation time for any phonon mode and temperature. At

low frequencies, the calculated relaxation times are extrapolated by assuming that $\tau \propto \omega^{-2}$, as predicted by Callaway [123].

4.3.2 Molecular dynamics predictions

To assess the accuracy of the theoretical expressions for the thermal boundary resistance, their predictions are compared to independent predictions obtained from MD simulations and the direct method, which require no assumptions about the nature of the phonon scattering. The full details related to these simulations are provided in Section 2.6.

The initial atomic positions are chosen to obtain relaxed structures in a manner similar to that used for the LD-based calculations (described in Section 3.4.1). In the MD simulations, however, the temperature dependence of the bulk lattice constants is also included, though it is found to have negligible effect on the predicted thermal boundary resistance. From separate MD simulations run in the NPT ensemble, the bulk lattice constants of SW Si and SW Ge are found to be approximated to within 0.02% between temperatures of 300 K and 1000 K by

$$a_{Si}(T) \quad = \quad 5.430 + 1.975 \times 10^{-5}T \ [\text{Å}] \tag{4.19}$$

$$a_{Ge}(T) \quad = \quad 5.654 + 3.205 \times 10^{-5}T \ [\text{Å}], \tag{4.20}$$

where T is in Kelvin. When assigning the initial atomic positions for the direct method simulations, the bulk lattice constants are evaluated using the average temperature in the simulation cell, $\bar{T}$. The z components of the initial atomic positions are set using species-dependent perpendicular lattice constants that lead to zero-stress in the z direction. These perpendicular lattice constants are calculated from elasticity theory to be [124]

$$a_\perp = a \left[1 - \frac{2C_{12}}{C_{11}} \left(\frac{a_\parallel}{a} - 1 \right) \right], \tag{4.21}$$
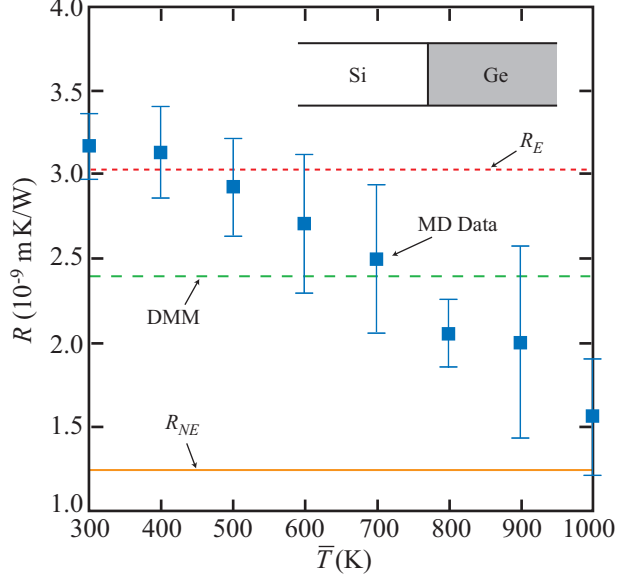
Figure 4.3: Temperature-dependence of the thermal boundary resistance of a symmetrically-strained Si/Ge interface. The error bars provided for the MD-predicted values represent the 95% confidence interval based on five independent simulations. Reprinted with permission from Ref. [26], Copyright 2009 American Physical Society.

where C_{11} and C_{12} are the elastic constants. Using the analytical method described by Cowley [82], C_{11} and C_{12} are calculated to be 151.6 GPa and 76.5 GPa for SW Si, and 138.3 GPa and 50.9 GPa for SW Ge.

4.4 Results

4.4.1 Temperature-dependence of the Si/Ge thermal boundary resistance

The MD predictions of the thermal boundary resistance for the symmetrically-strained Si/Ge interface between temperatures of 300 K and 1000 K are shown in Fig. 4.3. Error bars representing the 95% confidence interval based on five independent simulations are provided for each data point. A low-temperature regime in which the thermal boundary resistance is temperature-independent and equal to $\sim 3.1 \times 10^{-9}$ m²-K/W, and a high-temperature regime in which the thermal boundary resistance decreases with increasing temperature are observed. The boundary between these

regimes exists at a temperature between 400 K and 500 K.

As mentioned in Section 4.1.1, experimental measurements of the thermal boundary resistance of an isolated interface have only been made for metal/dielectric interfaces. To provide a comparison to the MD predictions, an estimate of the experimental Si/Ge thermal boundary resistance is made based on the thermal conductivity measurements of Borca-Tasciuc *et al.* for undoped, symmetrically-strained Si/Ge superlattices [125]. For a Si/Ge superlattice with interfaces separated by 7 nm, they measured the thermal conductivity in the direction perpendicular to the interfaces to be 2.9 W/m-K at a temperature of 300 K [125]. Here, the Si/Ge thermal boundary resistance is estimated to be of order 10^{-9} m^2-K/W by assuming that the dominant source of thermal resistance in these superlattices is due to the interfaces.[3] This estimate is in agreement with the MD-predicted values.

The MD-predicted temperature-dependence of the Si/Ge thermal boundary resistance at high temperatures is attributed to inelastic phonon interface scattering, which (i) increases with increasing temperature due to increasing anharmonicity of the atomic interactions, and (ii) tends to increase the phonon transmission coefficients [9]. This mechanism is believed to dominate over other potential mechanisms, which are identified from the expressions for R_E and R_{NE} [Eqs. (4.9) and (4.10)]. First, the temperature-dependence of the phonon frequencies and group velocities is negligible for SW Si and Ge, and $\partial f_{\mathrm{BE}}/\partial T$ is a constant in the classical limit. Second, the temperature-dependence of the lead thermal conductivities is canceled by the temperature-dependence of the phonon relaxation times in Eq. (4.17). The temperature-independence of the thermal boundary resistance in the low-temperature

---

[3]This estimate of the experimental Si/Ge thermal boundary resistance can only be considered accurate to an order of magnitude for two reasons. First, the interfaces are not isolated from each other, as they are separated by a distance much less than the bulk phonon mean free paths (e.g., the average phonon mean free path in Si is estimated to be 300 nm at room temperature [7]). Second, the lattice mismatch between Si and Ge will lead to strain-induced defects (e.g., misfit dislocations) at a realistic Si/Ge interface [28, 124].

regime is thus taken as an indication that the phonon interface scattering there is elastic.

An intuitive explanation for why increasing inelastic phonon interface scattering tends to increase the phonon transmission coefficients and decrease the thermal boundary resistance was provided by Swartz and Pohl [9]. Here, their explanation is adapted for discussion of the Si/Ge interface. If a phonon incident on the Si/Ge interface from the Si side has a frequency greater than the maximum Ge frequency, none of its energy can transmit across the interface if the phonon can only scatter elastically. On the other hand, there is a possibility for energy transmission if the phonon can scatter inelastically into two phonons of lower frequency. Inelastic phonon scattering thus increases the available channels for thermal conductance across the interface and decreases the thermal boundary resistance. Similar trends of decreasing thermal boundary resistance with increasing temperature have been predicted from MD [73, 126] and observed experimentally [99, 105, 106], and attributed to inelastic phonon interface scattering.

4.4.2 Thermal boundary resistance of the Si/heavy-Si interfaces

In Fig. 4.4, the MD predictions of the thermal boundary resistance for the Si/heavy-Si interfaces are shown as a function of mass ratio at a temperature of 500 K. The 95% confidence interval is provided for two of the data points. The thermal boundary resistance decreases monotonically with decreasing mass ratio and approaches zero for $m_R = 1$, the case where no interface is present in the system. The phonon interface scattering is expected to be elastic at all the Si/heavy-Si interfaces at this temperature. This expectation is based on (i) the fact that a heavy-Si atom samples a more harmonic potential well than a Si atom because of its smaller
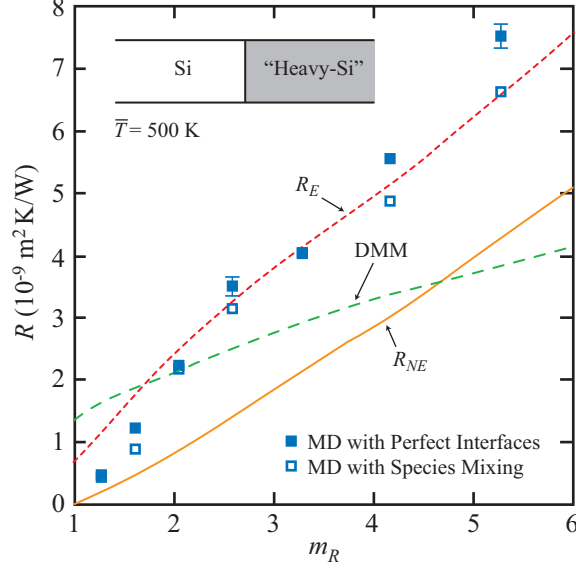
Figure 4.4: Thermal boundary resistance of the Si/heavy-Si interface plotted as a function of mass ratio (m_R) at a temperature of 500 K.

mean-square atomic displacement [88], and (ii) the observation that the anharmonicity in Si does not lead to significant inelastic scattering at the Si/Ge interface at this temperature (see Fig. 4.3).

For comparison, MD predictions of the thermal boundary resistance for Si/heavy-Si interfaces with species mixing in the first monolayer on either side of the interface are also provided in Fig. 4.4. The species mixing is included by randomly assigning the species of each atom in the interface region using the methodology discussed in Section 6.2.2. As will be shown in Chapter VI, this level of species mixing drastically alters the magnitude and period-length dependence of the thermal conductivity of Si/Ge superlattices. For the Si/heavy-Si interfaces, however, species mixing has negligible effect on the thermal boundary resistance.

4.4.3 Comparison with theoretical predictions

The accuracy of the theoretical expressions for the thermal boundary resistance is assessed by comparing their predictions to the MD-predicted values. For the Si/Ge interface, R_E [Eq. (4.9)] is calculated to be 3.0×10^{-9} m^2-K/W in the classical limit. As shown in Fig. 4.3, this value is in good agreement with the MD predictions at and below a temperature of 500 K, where the phonon scattering is predominantly elastic. This value of R_E is also within 5% of the value of 2.85×10^{-9} m^2-K/W calculated by Zhao and Freund for the Si/Ge interface in the classical limit using a similar LD-based method and the SW potential [53]. The small difference between the calculations is due to lattice mismatch strain, which was neglected by Zhao and Freund. For the Si/heavy-Si interfaces at a temperature of 500 K (Fig. 4.4), R_E is in agreement with the MD-predicted values to within 12% for $m_R \geq 2$. As expected, R_E is erroneously nonzero when no interface is present in the system (i.e., $m_R = 1$).

The calculations of R_{NE} [Eq. (4.10)], which are also provided in Figs. 4.3 and 4.4, are in poor agreement with the MD-predicted thermal boundary resistances. For the Si/Ge interface in the classical limit, R_{NE} is 1.3×10^{-9} m^2-K/W, approximately 60% less than the MD-predicted values in the low-temperature, elastic scattering regime. For the Si/heavy-Si interfaces at a temperature of 500 K, R_{NE} decreases with decreasing mass ratio and is equal to zero when no interface is present in the system, consistent with the MD-predicted trend. Over the entire mass ratio range, however, R_{NE} is 40-60% less than the MD-predicted values.

These observations are consistent with the findings of Aubry *et al.* [117] and Kimmer *et al.* [116], who compared MD-predicted thermal resistances to theoretically calculated values for two SW Si grain boundaries at a temperature of 500 K. They

used input from MD wave-packet simulations and assumed that either τ or the product $\tau v_{g,z}$ was constant for all modes in their theoretical calculations. They predict the thermal resistance of the $\Sigma 3(111)$ grain boundary from MD to be 0.1×10^{-9} m²-K/W, a value within 20-60% of R_{NE} and a factor of 8 less than R_E. Based on the MD-predicted thermal resistance, the level of phonon scattering at this grain boundary is believed to be similar to that at a Si/heavy-Si interface with $m_R = 1.1$. For this interface, a similar relationship between R_E, R_{NE} and the MD-predicted thermal boundary resistance would also be expected based on the trends shown in Fig. 4.4. For the $\Sigma 29(001)$ grain boundary, their MD-predicted thermal resistance is 1.3×10^{-9} m²-K/W, a value within 10% of R_E but 50% greater than R_{NE}. Based on the MD-predicted thermal resistance, the level of phonon scattering at this grain boundary is believed to be comparable to that for a Si/heavy-Si interface with $m_R = 1.6$, for which R_E is also in closer agreement with the MD-predicted thermal boundary resistance than R_{NE}.

As mentioned in Section 4.3.1, R_E and R_{NE} are evaluated by assuming that the phonon interface scattering is specular and elastic. Both assumptions must be valid in the MD simulations to provide an accurate assessment of the theoretical expressions for the thermal boundary resistance. The assumption of elastic scattering has already been demonstrated to be valid at temperatures less than or equal to $\sim$500 K (see Section 4.4.1). The assumption of specular scattering is also expected to be valid for the perfect interfaces because they contain no defects or roughness that would promote diffuse scattering. For additional evidence of this claim, the MD-predicted thermal boundary resistances are compared to values calculated using Eq. (4.9) with the phonon transmission coefficients determined by the DMM, where all phonons are assumed to scatter diffusively at the interface [9, 110]. Under this assumption, the

phonon transmission coefficient depends only on the incident phonon frequency and is given by [9, 110]

$$\alpha_{L \rightarrow R}^{DMM}(\omega^I) = \frac{\frac{1}{(2\pi)^3} \int_R \sum_\nu |v_{g,z}| \delta \left[\omega - \omega^I\right] d\boldsymbol{\kappa}}{\frac{1}{(2\pi)^3} \int_L \sum_\nu |v_{g,z}| \delta \left[\omega - \omega^I\right] d\boldsymbol{\kappa} + \frac{1}{(2\pi)^3} \int_R \sum_\nu |v_{g,z}| \delta \left[\omega - \omega^I\right] d\boldsymbol{\kappa}},$$

(4.22)

where

$$\begin{aligned} \delta &= \frac{1}{\Delta\omega} & \text{if } |\omega - \omega^I| \leq \frac{\Delta\omega}{2} \\ &= 0 & \text{otherwise.} \end{aligned}$$

Equation (4.22) is evaluated using Monte Carlo integration with 10^5 random wave vectors, phonon properties obtained from harmonic LD-based calculations and a frequency bin width, $\Delta\omega$, of 1 rad/ps. As shown in Fig. 4.3, the DMM-predicted thermal boundary resistance for the Si/Ge interface is 20% less than the MD-predicted values in the low-temperature, elastic scattering regime. This agreement is believed to be fortuitous, however, because for the Si/heavy-Si interfaces (see Fig. 4.4), the DMM- and MD-predicted thermal boundary resistances are in poor agreement at all mass ratios except near $m_R \approx 2$, which is close to the atomic mass ratio between Ge and Si of 2.6. The fact that R_E is in better agreement with the MD-predicted thermal boundary resistances than the DMM-predicted values is taken as further evidence that the assumption of specular phonon scattering is valid.

Even when the phonon interface scattering is specular and elastic, neither R_E nor R_{NE} is in good agreement with the MD-predicted thermal boundary resistances for all of the interfaces examined here. For R_E, the inaccuracy observed for the Si/heavy-Si interfaces with $m_R < 2$ is due to the assumption of equilibrium phonon distributions in each lead, as mentioned in Section 4.2.2. For R_{NE}, the observed inaccuracy is

attributed to the assumption of bulk-like nonequilibrium phonon distributions near the interface. According to the BTE, the steady-state phonon distribution for a given mode at position $\mathbf{r}$ is such that the rate of phonon creation and annihilation is balanced by the rate that phonons leave the neighborhood of $\mathbf{r}$ due to diffusion [38,79]. In a bulk crystal with no defects, the phonon creation and annihilation rates are determined by inelastic multi-phonon scattering processes, which are accounted for in the anharmonic LD-based calculations described in Section 4.3.1. Near an interface, however, the phonon creation and annihilation rates will be affected by phonon scattering at the interface, leading to phonon distributions that are different from those in the bulk. Because R_E is in good agreement with the MD predictions for the Si/Ge interface and the Si/heavy-Si interfaces with $m_R > 2$, it is hypothesized that for these interfaces these additional scattering processes lead to phonon distributions that are well-approximated by the equilibrium distribution at T_L or T_R.

4.5   Summary

The accuracies of two theoretical expressions for thermal boundary resistance were assessed by comparing their predictions to independent predictions from MD simulations. In one expression (R_E), the phonon distributions are assumed to follow the equilibrium, Bose-Einstein distribution, while in the other expression (R_{NE}), the phonons are assumed to have nonequilibrium, but bulk-like distributions. The phonon properties are obtained using LD-based methods, which assume that the phonon interface scattering is specular and elastic.

A symmetrically-strained Si/Ge interface and a series of Si/heavy-Si interfaces were considered. All of the interfaces used in the comparison are perfect, justifying the assumption of specular scattering. The MD-predicted Si/Ge thermal boundary re-

sistance is temperature-independent below a temperature of $\sim$500 K, indicating that the phonon scattering is elastic, as required for the validity of the theoretical calculations. At higher-temperatures, the MD-predicted Si/Ge thermal boundary resistance decreases with increasing temperature, a trend attributed to inelastic scattering.

With the exception of the Si/heavy-Si interfaces with $m_R < 2$, the theoretical calculations of R_E were found to be in good agreement with the MD-predicted thermal boundary resistances at temperatures where the phonon scattering is elastic. The inaccuracy of R_E observed for the Si/heavy-Si interfaces with $m_R < 2$ is most extreme at $m_R = 1$, where R_E is erroneously nonzero. This inaccuracy has been attributed to the assumption of equilibrium phonon distributions in each lead [96, 120]. The theoretical expression for R_{NE} gives the correct result of zero thermal boundary resistance for the Si/heavy-Si interface with $m_R = 1$. For the Si/Ge interface and for the Si/heavy-Si interfaces with $m_R > 1$, however, R_{NE} was found to be 40-60% less than the corresponding MD-predicted thermal boundary resistances at temperatures where the phonon interface scattering is elastic. This inaccuracy was attributed to the assumption of bulk-like phonon distributions in each lead. It was argued that the phonon distributions near the interface will deviate from their bulk values due to the additional phonon creation and annihilation processes that are associated with the phonon-interface scattering.

CHAPTER V

Effect of film thickness on the thermal resistance of semiconductor thin films

5.1   Introduction

5.1.1   Background

The thermal transport properties of semiconductor films are experimentally observed to depend on the film thickness when it is less than the bulk phonon mean free paths [5, 7, 127, 128]. For example, at room temperature, the in-plane thermal conductivity of Si thin films is approximately half of the bulk value for film thicknesses on the order of 100 nm [7, 129]. Furthermore, if phonon transport is ballistic in the film, the phonon distributions on either side of the film will be correlated to one other. This correlation will lead to a thermal boundary resistance between the film and its adjoining medium that is dependent on the film thickness. An understanding of these thickness dependencies is required to develop accurate models for predicting the thermal transport properties of semiconductor films.

One common approach for modeling thermal transport in semiconductor thin films is to solve the BTE [118, 129–133]. In this approach, phonons are treated as particles and their wave-like nature is neglected. Closing the BTE requires specification of the phonon scattering rates (i.e., the phonon relaxation times or mean free paths) and boundary conditions. One common approach for specifying the scattering rates

is to assume that all of the phonons in the film have a mode-independent mean free path [118, 130]. This assumption is difficult to justify, however, because the phonon relaxation times in semiconductors such as Si are predicted to span many orders of magnitude [38, 79, 89]. Another approach is to assume that the phonon relaxation times follow an analytical expression [132, 133], such as $\tau = A\omega^{-2}$, where the temperature-dependent proportionality constant, A, is determined by fitting to experimental data [123]. The boundary conditions are often specified by assuming that a fraction of the phonons scatter specularly at the boundaries between the film and its adjoining medium, which may be a solid, fluid, or vacuum, while the remainder scatter diffusely [38, 118]. This fraction is often treated as a mode-independent fitting parameter, thereby neglecting the atomic-level detail of the boundaries. Even with more accurate methods to close the BTE (e.g., mode dependent phonon properties obtained from *ab initio* calculations), the BTE-based approach will not be suitable for films with thicknesses on the same scale as the average wavelength of the thermally excited phonons, where the wave-like nature of the phonons is important [31]. For Si at room temperature, this wavelength is estimated to be 1 nm [31].

5.1.2 Objective

In this chapter, LD calculations and MD simulations are used to examine the dependence of thin film thermal resistance on film thickness. Both methods are capable of modeling films in which the wave-like nature of the phonons is important. By comparing the predictions of the two methods, the effects of changes in the allowed vibrational states in the film and the presence of inelastic phonon-phonon scattering in the film on the thin film thermal resistance are examined.

Two types of thin film structure are considered (see Fig. 5.1). In one structure, a
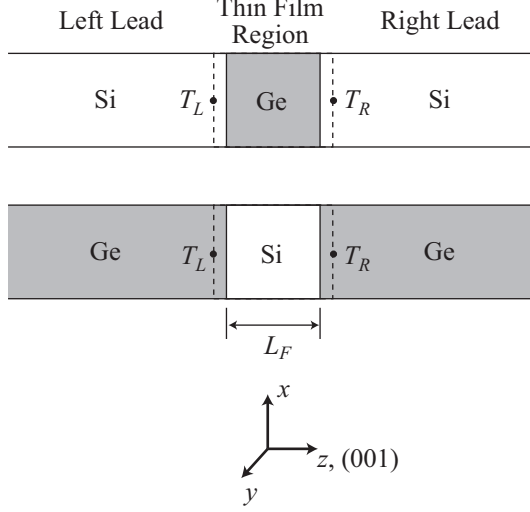
Figure 5.1: Schematic diagrams of the Si/Ge/Si and Ge/Si/Ge structures.

Ge film with thickness L_F is confined between two Si leads (the Si/Ge/Si structure). In the other, a Si film is confined between two Ge leads (the Ge/Si/Ge structure). While similar configurations of a thin film confined by larger extents of a different species are often encountered in application [see Fig. 1.1(a)], they have received minimal theoretical attention, especially for thermal transport in the cross-plane direction. Previous MD-based studies of cross-plane thermal transport in thin films used simulation cells that contained a film confined between two thermal reservoirs of the same species [30, 32, 134–136]. In these studies, the film cross-plane thermal conductivity is predicted to increase towards the bulk value as the film thickness increases due to the decreasing effect of phonon scattering at the film/reservoir boundaries on the phonon mean free paths. In the Si/Ge/Si and Ge/Si/Ge structures, the Si/Ge interfaces are oriented along the (001) crystallographic plane and the film is symmetrically-strained by setting the lattice constant in the x and y directions to the average of the bulk Si and bulk Ge lattice constants. The layer spacings in the z direction are chosen to give zero-stress in that direction using the methodology described in Sections 3.4.1

76

and 4.3.2.

5.2 Predicting the thin film thermal resistance

The thin film thermal resistance is defined here to be the thermal resistance of the entire thin film region, which includes the film and the two lead/film interfaces (see Fig. 5.1). It is thus defined as

$$R = \frac{T_L - T_R}{q},$$
(5.1)

where T_L and T_R are the lead temperatures at the lead/film boundaries.

The thin film thermal resistance is calculated theoretically and compared to independent predictions obtained using direct method MD simulations. The methodology related to the MD simulations is provided in Section 2.6. In the theoretical calculations, the expression for the thermal resistance that was derived in Chapter V under the assumption that the phonon distributions in each lead follow the equilibrium Bose-Einstein distribution [i.e., R_E, given by Eq. (4.9)] is used. This assumption was demonstrated in Section 4.4.3 to yield accurate predictions of the Si/Ge thermal boundary resistance. As the average phonon transmission coefficient approaches unity, however, the accuracy of this approximation is expected to decrease and lead to thermal resistance predictions that are too large [120]. Approximating the phonon distributions using the equilibrium distribution is thus expected to be suitable for modeling a thin film structure if the average phonon transmission coefficient across the film is less than or equal to that across the isolated Si/Ge interface. This condition is met when the thin film thermal resistance exceeds the Si/Ge thermal boundary resistance.

The theoretical calculations are performed in the classical limit using phonon properties obtained using the harmonic LD calculations discussed in Chapter III. The cal-

culation of the phonon transmission coefficients assumes that (i) no inelastic phonon scattering occurs within the thin film region, (ii) the phonons scatter specularly at the lead/film boundaries, and (iii) the phonons are spatially delocalized. The assumption of no inelastic scattering is valid when the phonon scattering at the Si/Ge interfaces is elastic and the phonons travel ballistically across the film. To ensure that the first condition is met, the MD simulations are performed at a temperature of 500 K, where the phonon scattering is primarily elastic (see Section 4.4.1). The second condition is met when the film thickness is less than the phonon mean free paths in the corresponding bulk material. This point is discussed further in Section 5.3.3. The assumption of specular scattering is valid because the thin film structures contain no defects or roughness that would promote diffuse scattering [9, 38]. As discussed by Schelling and Phillpot, in order to properly model the interference between phonons reflected from the lead/film interfaces when the phonon transport is ballistic, the extent of the phonon wave-packet should be greater than the film thickness [54]. The assumption that the phonons are spatially delocalized is thus appropriate.

5.3   Results

5.3.1   Thin film thermal resistance

The theoretically calculated and MD-predicted thin film thermal resistances are provided in Fig. 5.2. Error bars representing the 95% confidence interval based on five independent simulations are provided for four of the MD-predicted data points. The MD predictions are made for films with thicknesses between 0.2 nm and 30 nm, while the theoretical calculations are made for thicknesses between 0.2 nm and 4 nm. Because the theoretically calculated thin film thermal resistances are independent of the film thickness for $L_F > 2$ nm, however, the values at $L_F = 4$ nm are extrapolated
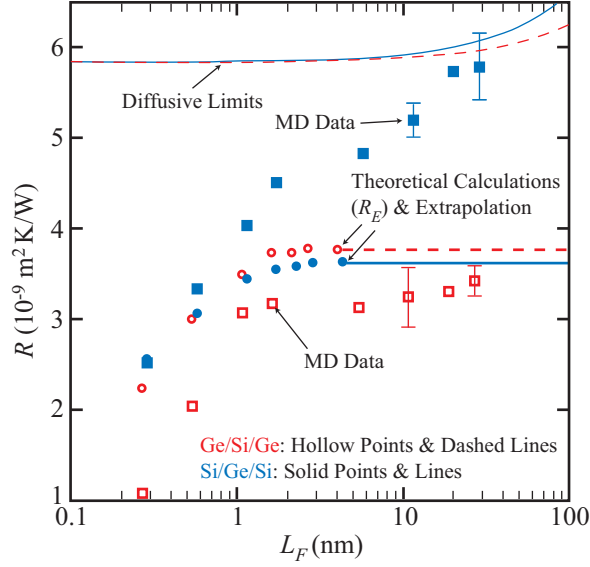
Figure 5.2: Theoretically calculated and MD-predicted thin film thermal resistances. The theoretical calculations are performed in the classical limit for comparison to the classical MD simulations, which are performed at a temperature of 500 K. The thin film thermal resistance in the diffusive limit is also provided for comparison.

to allow for comparison to the MD predictions. The values of the thin film thermal resistance in the diffusive limit, R_{DL}, reached when the film thickness is much greater than the phonon mean free paths in the corresponding bulk material, are also provided in Fig. 5.2 for comparison. The thin film thermal resistance in the diffusive limit is

$$R_{DL} = 2R_{Si/Ge} + \frac{L_F}{k}, \tag{5.2}$$

where $R_{Si/Ge}$ is the Si/Ge thermal boundary resistance and k is the bulk thermal conductivity of the film species. The L_F/k term is the thermal conduction resistance often used in continuum-level heat transfer analyses [72]. For the calculation of the diffusive limit, $R_{Si/Ge}$ is predicted using direct method MD simulations and k_{Si} and k_{Ge} are predicted using MD simulations and the Green-Kubo method. The predicted values of $R_{Si/Ge}$, k_{Si}, and k_{Ge} at a temperature of 500 K are $2.93 \pm 0.29 \times 10^{-9}$ m²-K/W, 230 ± 47 W/m-K, and 132 ± 34 W/m-K (see Fig. 4.3 and Table 2.3).

For the Ge/Si/Ge structures, the MD-predicted thin film thermal resistances increase rapidly with increasing thickness for $L_F < 2$ nm and are independent of thickness for 2 nm $< L_F < 30$ nm. This trend is in qualitative agreement with that calculated theoretically. The theoretically calculated thin film thermal resistances, however, are greater than the MD-predicted values. For example, the theoretically calculated thermal resistance of the Ge/Si/Ge structure with $L_F = 0.27$ nm is two times greater than the MD-predicted value. This discrepancy is likely due to inaccuracy in the phonon distribution functions used in the calculations because the MD-predicted thin film thermal resistance is less than the Si/Ge thermal boundary resistance (see discussion preceding Section 5.2). For the structures with $L_F > 2$ nm, the MD-predicted thin film thermal resistances are greater than the Si/Ge thermal boundary resistance, and the theoretically calculated and MD-predicted thermal resistances agree to within 15%.

For the Si/Ge/Si structures with $L_F < 2$ nm, the MD-predicted thin film thermal resistances increase rapidly with increasing thickness. This trend is in agreement with that calculated theoretically. Differences are observed between the MD and theoretical predictions, however, for structures with $L_F > 2$ nm. For these structures, the MD-predicted thin film thermal resistances continue to increase towards the diffusive limit with increasing film thickness, while the theoretically calculated values are independent of the film thickness.

Two mechanisms for understanding the thickness-dependence of the thin film thermal resistances are proposed. The first mechanism is changes in the allowed vibrational states in the film, which can influence both the phonon transmission coefficients and the nature of the phonon-phonon scattering in the film (through the selection rules for multi-phonon scattering events). Such changes arise due to the decreasing

fraction of film atoms that are bonded to lead atoms and the increased resolution of the Brillouin zone of the film species (defined using the bulk primitive lattice vectors) as the film thickness increases. The second mechanism is increased phonon-phonon scattering in the film as the film thickness approaches or exceeds the mean free path of the phonons in the film. Such inelastic scattering leads to reduced coupling of phonons on either side of the film, which may alter the phonon transmission coefficients, and increased thermal conduction resistance of the film. In Sections 5.3.2 and 5.3.3, the manner in which these two mechanisms affect the thermal resistance of the Si/Ge/Si and Ge/Si/Ge structures is discussed.

5.3.2 Allowed vibrational states-effect

Because the theoretical calculations neglect inelastic phonon scattering, the dependence of the theoretically calculated thin film thermal resistance on film thickness must be due to changes in the allowed vibrational states in the film. The MD-predicted thickness-dependence for the Si/Ge/Si structures with $L_F < 2$ nm and all of the Ge/Si/Ge structures is also likely to be a result of these changes due to the qualitative agreement between the theoretically calculated and MD-predicted trends. To quantify the thickness-dependence of the allowed vibrational states, LD calculations are used to obtain the phonon density of states (PDOS), $\rho(\omega)$, in the film. These calculations are performed using a unit cell that contains one atom for each monolayer in the film and one atom for each of 12 monolayers in each lead. This unit cell is periodically replicated in the xy plane. Increasing the length of the each lead has no discernable affect on the PDOS in the film. Extending on the concept of a local PDOS (i.e., the PDOS of a single atom in a supercell) used by others [137], the

81

PDOS in the film is defined here to be

$$\rho(\omega') = \frac{1}{(2\pi)^2 L_F} \int \sum_\nu \sum_j \sum_\beta \delta\left[\omega(\boldsymbol{\kappa}, \nu) - \omega'\right] |e_{j,\beta}(\boldsymbol{\kappa}, \nu)^2| d\boldsymbol{\kappa}, \qquad (5.3)$$

where the j-summation is over the film atoms in the unit cell, the β-summation is over the three Cartesian coordinates, $e_{j,\beta}(\boldsymbol{\kappa}, \nu)$ is the j, β-component of the phonon polarization vector for mode $(\boldsymbol{\kappa}, \nu)$, and

$$\begin{aligned} \delta &= \frac{1}{\Delta\omega} \qquad \text{if } |\omega(\boldsymbol{\kappa}, \nu) - \omega'| \leq \frac{\Delta\omega}{2} \\ &= 0 \qquad \text{otherwise.} \end{aligned} \qquad (5.4)$$

When the PDOS is defined using Eq. (5.3), its integral over frequency is equal to $3n_v$, where n_v is the number density of atoms in the film. Equation (5.3) is evaluated using Monte Carlo integration with 10^4 random phonon wavevectors in the two-dimensional Brillouin zone for the thin film structure and a frequency bin width, $\Delta\omega$, of 0.5 rad/ps.

The PDOS in the films of three Ge/Si/Ge and three Si/Ge/Si structures are provided in Figs. 5.3(a) and 5.3(b). The PDOS for bulk Si and Ge, which are obtained under the same strain conditions that exist in the thin film structures, are also provided for comparison (denoted by $L_F = \infty$). For films with $L_F < 2$ nm, the film PDOS is different than that of the corresponding bulk PDOS. Notable is the nonzero PDOS in the Ge film of the Si/Ge/Si structure between the maximum frequency in bulk Ge, ω_{max}^{Ge}, of 69 rad/ps and a frequency of ∼90 rad/ps [Fig. 5.3(b)]. As the film thickness increases, the PDOS in the film becomes increasingly bulk-like, with minimal differences between the film and bulk PDOS observed for films with thickness $L_F > 2$ nm. This transition to a bulk-like PDOS coincides with the thickness where the thin film thermal resistances stop increasing rapidly with increasing film thickness. This agreement is taken as evidence that the thickness-dependence of the
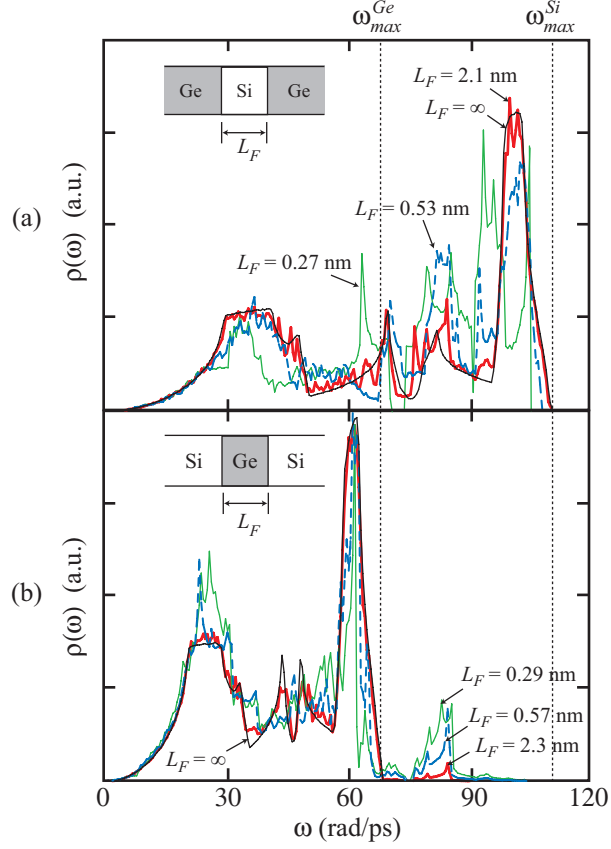
Figure 5.3: Phonon density of states in the films of (a) three Ge/Si/Ge, and (b) three Si/Ge/Si structures. The PDOS for bulk Si and Ge (denoted by $L_F = \infty$) are also provided for comparison.

thin film thermal resistance for films with $L_F < 2$ nm is due to changes in the allowed vibrational states in the film.

To further examine how the changes in the allowed vibrational states in the film affect the thermal transport, the contributions to the theoretically calculated thin film thermal conductance, G_E, as a function of either phonon frequency or incidence angle, θ, are calculated. These functions, g_ω and g_θ, are defined such that

$$G_E = R_E^{-1} = \int_0^\infty g_\omega d\omega = \int_0^{\pi/2} g_\theta d\theta. \tag{5.5}$$

In Figs. 5.4(a)-5.4(d), g_ω and g_θ are provided for the thin film structures for which the PDOS was provided in Figs. 5.3(a) and 5.3(b). As with the film PDOS, g_ω and g_θ
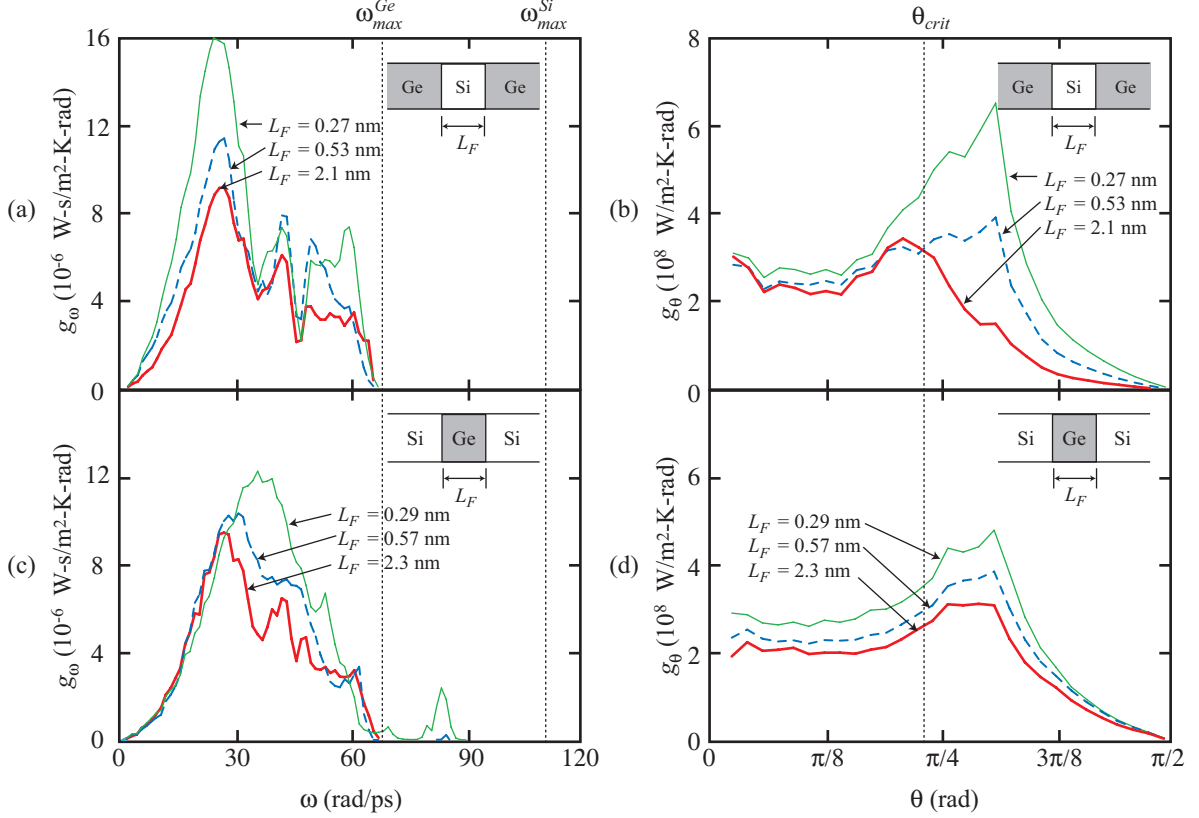
Figure 5.4: Theoretically calculated dependence of the thin film thermal conductance on (a) phonon frequency and (b) phonon incidence angle for the Ge/Si/Ge structures, and (c) phonon frequency and (d) phonon incidence angle for the Si/Ge/Si structures.

are independent of film thickness for $L_F > 2$ nm. Vertical lines are provided in Figs. 5.4(a) and 5.4(c) for the maximum phonon frequencies in bulk Si and Ge. A vertical line is also provided for the Si/Ge critical angle, θ_{crit}, in Figs. 5.4(b) and 5.4(d). By Snell's law, the phonon transmission coefficient is zero for a phonon incident on an interface from a material with a low group velocity to a material with higher group velocity (e.g., Ge to Si) if its incidence angle is greater than θ_{crit} [9,94,118]. Here, θ_{crit} is estimated to be 0.73 rad under the approximation that the phonon group velocities in each material are equal v_{ac} [see Eq. (2.29)]. Due to the realistic phonon dispersion used in the theoretical calculations, g_θ is nonzero for incidence angles greater than this estimated θ_{crit}. The critical angle is used here only as a point of reference.

While the theoretically calculated thermal resistances of the two types of thin film structure are comparable in terms of magnitude and thickness-dependence, the thickness-dependence is manifested differently in each type of structure. As the film thickness in the Ge/Si/Ge structures decreases, g_θ significantly increases only for θ greater than $\sim \theta_{crit}$ [see Fig. 5.4(b)], and g_ω increases for all frequencies by an approximately frequency-independent factor [Fig. 5.4(a)]. As the film thickness in the Si/Ge/Si structures decreases, g_ω increases only for ω greater than $\sim$30 rad/ps [Fig. 5.4(c)], and g_θ increases for all incident angles by a factor that is independent of incidence angle [Fig. 5.4(d)]. For these structures, g_ω is even nonzero for frequencies of $\omega_{max}^{Ge} < \omega < 90$ rad/ps due to the vibrational states that exist in this frequency range when $L_F < 2$ nm [see Fig. 5.3(b)]. These trends are due solely to changes in the phonon transmission coefficients because the other phonon properties relevant to the thermal conductance [see Eq. (4.9)] are independent of the film thickness. Furthermore, the frequency- and angular-dependence of the phonon transmission coefficients can be separated because there is little correlation between phonon direction and frequency in bulk Si and bulk Ge, as evidenced by their near-isotropic phonon dispersion curves [138]. The g_ω and g_θ trends therefore suggest that the changes in the allowed vibrational states affect mostly the transmission coefficients of (i) phonons with $\theta > \theta_{crit}$ in the Ge/Si/Ge structures (independent of frequency), and (ii) phonons with $\omega > 30$ rad/ps in the Si/Ge/Si structures (independent of incidence angle).

5.3.3 Phonon-phonon scattering-effect

Temperature profiles

As demonstrated in Section 5.3.2, thickness-dependent changes in the allowed vibrational states have negligible effect on the thin film thermal resistance for films with $L_F > 2$ nm. Any thickness-dependence of the thin film thermal resistance for
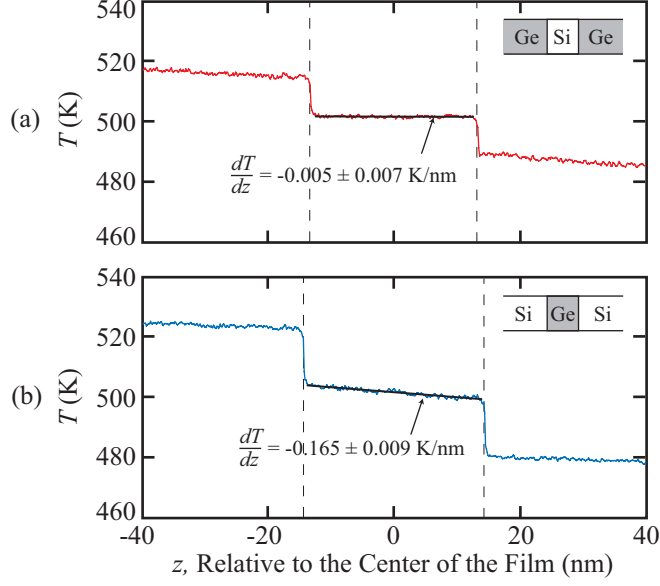
Figure 5.5: Steady-state temperature profiles near and across the thin film region of the Si/Ge/Si and Ge/Si/Ge structures with a film thickness of 200 monolayers ($L_F = 28.7$ nm for the Ge film and $L_F = 26.6$ nm for the Si film) predicted from MD simulation. The same heat flux of $q = 7.23$ GW/m^2 was applied across both structures.

these films must therefore be due to the effects of inelastic phonon-phonon scattering in the film. Because the MD-predicted thermal resistances of the Ge/Si/Ge structures with $2 < L_F < 30$ nm are thickness-independent, the phonon transport must be ballistic in the Si film. For the Si/Ge/Si structures with $L_F > 2$ nm, however, the MD-predicted thin film thermal resistances increase with increasing film thickness, suggesting that the phonon-phonon scattering in the Ge film is non-negligible (i.e., the phonon transport is partially diffusive). Because the theoretical calculations assume ballistic phonon transport, this argument also explains why the theoretically calculated and MD-predicted thin film thermal resistances are in good agreement for the Ge/Si/Ge structures but are in poor agreement for the Si/Ge/Si structures with $L_F > 2$ nm.

Additional evidence for ballistic phonon transport in the Ge/Si/Ge structures and more diffusive transport in the Si/Ge/Si structures is found in the MD-predicted

steady-state temperature profiles. The temperature profiles across a Ge/Si/Ge structure with $L_F = 26.6$ nm and a Si/Ge/Si structure with $L_F = 28.7$ nm (the films in both structures have a thickness of 200 monolayers) are shown in Figs. 5.5(a) and 5.5(b) as an example. The same heat flux of $q = 7.23$ GW/m^2 was applied across both structures. To reduce statistical fluctuations, each temperature profile is averaged over five independent simulations. Using a least-squares linear regression analysis, the temperature gradient in the Si film is found to be 0.005 ± 0.007 K/nm (95% confidence). This value is a factor of 6 less than the value of 0.031 K/nm that would develop in Si if the phonon scattering was entirely diffusive [calculated from the Fourier law, Eq. (2.22)]. Because phonon scattering is required to establish a temperature gradient [131, 138–140], the small temperature gradient in the Si film relative to the value in the diffusive limit is taken as evidence of ballistic phonon transport. In the Ge film, the temperature gradient is -0.165 ± 0.009 K/nm (95% confidence). This temperature gradient is a factor of 3 greater than the value of -0.060 K/nm that would develop if the phonon scattering was entirely diffusive, indicating the presence of phonon-phonon scattering in the film.

The MD-predicted thickness-dependence of the film temperature gradient for a fixed value of the heat flux is also different between the Ge/Si/Ge and Si/Ge/Si structures. For all of the Ge/Si/Ge structures ($L_F < 30$ nm), the temperature gradient is nearly zero and has no thickness-dependence because the phonon transport is ballistic [see Fig. 5.5(a)]. Flat temperature profiles have also been predicted by others using the lattice Boltzmann method for films in which the phonon transport is ballistic [138, 139]. As the film thickness increases, the lattice Boltzmann method predicts that the magnitude of the film temperature gradient increases towards the value in the diffusive limit. It is expected that a similar trend would be observed for

Ge/Si/Ge structures with $L_F > 30$ nm. For the Si/Ge/Si structures, however, the opposite trend is observed, and the magnitude of the temperature gradient in the Ge film decreases towards the value in the diffusive limit as the film thickness increases. This trend is in agreement with that predicted by others using MD simulation for films confined by two thermal reservoirs of the same species [30, 32, 134–136]. This difference suggests that the thermal transport in thin films depends not only on the species and thickness of the film, but also on the material that confines it.

Transition between ballistic and diffusive phonon transport

The objective now is to determine why ballistic phonon transport is observed in the Ge/Si/Ge structures while more diffusive transport is observed in the Si/Ge/Si structures. The standard technique for determining whether the phonon transport is ballistic, diffusive, or partially diffusive is to compare the average bulk phonon mean free path, Λ, to the film thickness. An estimate for Λ is obtained from the kinetic theory expression for thermal conductivity [52],

$$k = \frac{1}{3}C_v v_{ac}\Lambda, \tag{5.6}$$

where C_v is the specific heat per unit volume. Using thermal conductivities predicted from Green-Kubo MD simulations and classical specific heats, Λ is estimated for both bulk SW Si and SW Ge to be 50 nm at a temperature of 500 K. Based on this result, the transition from ballistic to diffusive transport might be expected to occur for similar values of the film thickness in the Ge/Si/Ge and Si/Ge/Si structures, which is contrary to the MD predictions (see Fig. 5.2). A higher-level analysis of the phonon-phonon scattering in the bulk species is needed.

The details of the phonon-phonon scattering in bulk Si and Ge is examined by calculating the phonon mean free path as a function of phonon frequency, $\bar{\lambda}_z(\omega)$, at
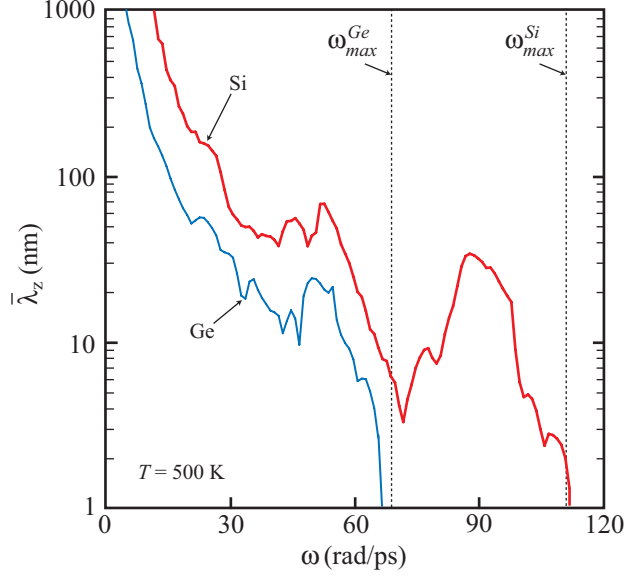
Figure 5.6: Average phonon mean free path in bulk SW Si and SW Ge as a function of phonon frequency at a temperature of 500 K.

a temperature of 500 K, where

$$\bar{\lambda}_z(\omega') = \frac{\int \sum_\nu \lambda_z(\boldsymbol{\kappa}, \nu)\delta\left[\omega(\boldsymbol{\kappa}, \nu) - \omega'\right] d\boldsymbol{\kappa}}{\int \sum_\nu \delta\left[\omega(\boldsymbol{\kappa}, \nu) - \omega'\right] d\boldsymbol{\kappa}}. \tag{5.7}$$

Here, λ_z is the phonon mode-dependent mean free path in the z direction, which is equal to $v_{g,z}\tau$. Equation (5.7) is evaluated using a frequency bin width of 0.5 rad/ps and phonon relaxation times predicted using anharmonic LD calculations for 32^3 evenly-spaced wavevectors in the first Brillouin zone for the conventional diamond unit cell [43, 75, 89]. The results are plotted in Fig. 5.6.

Consider Si/Ge/Si and Ge/Si/Ge structures with film thicknesses of $L_F = 1$ nm. As shown in Fig. 5.6, $\bar{\lambda}_z$ is greater than this film thickness for all phonon frequencies in bulk Ge and bulk Si. The phonon transport in both films is thus ballistic. Now consider what happens as the film thickness increases. For the Si/Ge/Si structure, the film thickness will immediately begin to exceed $\bar{\lambda}_z$ in bulk Ge for frequencies

89

near ω_{max}^{Ge}, leading to partially diffusive transport. When the film thickness reaches $L_F = 28.7$ nm (the largest value for the Si/Ge/Si structure), the film thickness exceeds $\bar{\lambda}_z$ for $\omega > 31$ rad/ps. According to Fig. 5.4(c), phonons in this frequency range contribute 51% to the thermal conductance when the phonon transport is ballistic [the LD calculations used to generate Figs. 5.4(a) - 5.4(d) assume ballistic transport]. For the Ge/Si/Ge structure, the phonon transport is entirely ballistic until the film thickness exceeds $\bar{\lambda}_z(\omega_{max}^{Ge}) = 5$ nm because phonons with $\omega > \omega_{max}^{Ge}$ do not contribute to the thermal transport [see Fig. 5.4(a)]. When the film thickness reaches $L_F = 26.6$ nm (the largest value for the Ge/Si/Ge structure), the film thickness exceeds $\bar{\lambda}_z$ for $\omega > 59$ rad/ps. According to Fig. 5.4(a), phonons in this frequency range contribute only 7% to the thermal conductance when the phonon transport is ballistic. These results suggest that the phonon transport across the Si/Ge/Si structures should be more diffusive than that across the Ge/Si/Ge structures, which is consistent with the MD predictions of the thin film thermal resistance (see Section 5.3.1). For both types of thin film structure, fully diffusive phonon transport is not expected until the film thickness is ~10 μm due to the large phonon mean free paths at low frequencies and the lack of other scattering mechanisms in the models [138].

5.4 Summary

The thin film thermal resistances of Ge/Si/Ge and Si/Ge/Si structures with film thicknesses, L_F, between 0.2 nm and 30 nm were calculated theoretically and compared to independent MD predictions. The theoretical calculations were performed in the classical limit using the expression for R_E that was derived in Chapter IV under the assumption that the phonon distributions in each lead follow the equilibrium, Bose-Einstein distribution [Eq. (4.9)]. The MD predictions were made at a

temperature of 500 K.

For structures with $L_F < 2$ nm, the thin film thermal resistances increase rapidly with increasing film thickness (see Fig. 5.2). Because the PDOS in the film is thickness-dependent only in this range (Fig. 5.3), this trend was attributed to changes in the allowed vibrational states in the film. These changes affect the dependence of the phonon transmission coefficient on incidence angle for the Ge/Si/Ge structures and on frequency for the Si/Ge/Si structures [Figs. 5.4(a)-5.4(d)].

For Ge/Si/Ge structures with $L_F > 2$ nm, the MD-predicted thermal resistances are thickness-independent and agree with the theoretically calculated values to within 15%. For Si/Ge/Si structures with $L_F > 2$ nm, the MD-predicted thermal resistances increase with increasing film thickness, while the theoretically calculated values are thickness-independent. Because the theoretical calculations assume that the phonon transport is ballistic, these results indicate that the phonon transport is ballistic in the Ge/Si/Ge structures and more diffusive in the Si/Ge/Si structures. The standard technique of comparing the mode-averaged phonon mean free path to the film thickness is insufficient in predicting whether the phonon transport would be ballistic or diffusive in the film. The correct prediction can be made when the frequency-dependence of the phonon mean free paths is considered (see Fig. 5.6).

The manner by which the temperature gradient in the film converges to the value in the diffusive limit for a fixed value of the heat flux was also found to be different between the two types of structure. For Si/Ge/Si structures, the magnitude of the temperature gradient decreases towards the value in the diffusive limit as the film thickness increases, while the opposite trend is expected for Ge/Si/Ge structures. This difference, along with the difference in the thickness-dependence of the phonon transmission coefficients, is taken as evidence that the thermal transport properties

of a thin film depend on the material that confines it in addition to the species and thickness of the film. This finding has implications in the interpretation of experimental data because it indicates that measured thermal conductivities may depend on the substrate material.

CHAPTER VI

Effect of interfacial species mixing on phonon transport in semiconductor superlattices

6.1 Introduction

6.1.1 Background

The thermal conductivities[1] of typical semiconductor superlattices (e.g., $Si/Si_{1-x}Ge_x$, $GaAs/AlAs$, and Bi_2Te_3/Sb_2Te_3) have been characterized experimentally [125, 141–155]. Some studies have found the superlattice thermal conductivity to be less than the thermal conductivity of an alloy of similar composition [125, 141–143, 145, 148, 150, 151]. This finding makes superlattices attractive for increasing ZT because semiconductor alloys are themselves, good thermoelectric materials [14, 19]. It is unclear, however, if the reductions below the alloy limit are due to phonon-interface scattering, coherent phonon wave effects, or phonon scattering at the defects induced by the strain associated with the lattice mismatch [83, 156]. The effect of the superlattice period length on the experimentally observed thermal conductivity is conflicting. Some studies have found that the thermal conductivity initially decreases with increasing period length until a minimum is reached, beyond which it increases [69, 142, 143, 148]. Others have observed that the thermal conductivity increases monotonically with increasing period length [141, 146, 153]. The quality of the internal superlattice interfaces

---

[1]In this chapter, references to the superlattice thermal conductivity correspond to the cross-plane direction.

may influence which trend is observed [153].

The most common modeling approaches used to investigate the experimental trends are rooted in the BTE [118, 151, 155, 157, 158] and LD calculations [159–167], both of which require many assumptions. In the BTE approach, phonons are treated as particles and their wave-like nature is neglected. This treatment requires that the phonon populations in neighboring layers be uncorrelated (i.e., incoherent phonon transport), valid when the phonon mean free path is less than the superlattice layer thicknesses. In addition, the nature of the phonon scattering within the layers (e.g., phonon relaxation times) and at interfaces must be specified *a priori* [118, 155]. The BTE approach predicts the primary resistance to thermal transport to be phonon scattering at interfaces [118, 151, 157, 158], leading to a trend of increasing thermal conductivity with increasing period length due to decreasing interface density.

Application of the LD method to model thermal transport in superlattices requires that the phonon populations in neighboring layers be coherently correlated and that the samples be perfectly periodic. The phonon populations will be coherently correlated when the phonon mean free path is greater than the superlattice period length. This assumption can be relaxed in a phenomenological manner to include incoherent effects by adding an imaginary component to the phonon wavevector [165, 166]. The requirement that the samples be perfectly periodic eliminates the modeling of alloys or deviations in superlattice interface quality,[2] both of which are common in applications. Traditional LD calculations are performed under the harmonic approximation [160–167]. As discussed in Chapter III, the phonon modes are decoupled under this approximation and thus, the phonon scattering rates must be specified.

---

[2]A LD-based approach was used by Ren *et al.* [160] to model interfacial species mixing in Si/Ge superlattices. This approach is questionable, however, because interfacial species mixing will lead to diffuse phonon scattering at the superlattice interfaces, destroying the phonon coherence required for the validity of the LD model.

This specification is typically done by assuming that the phonon relaxation times are phonon mode- and superlattice-independent [160–164, 167]. Broido and co-workers used an anharmonic LD-based approach to calculate the phonon mode-specific scattering rates for Si/Ge and GaAs/AlAs superlattices [159, 168]. They found that the assumption of a phonon mode- and superlattice-independent relaxation time is poor and predicted the thermal conductivity of short-period superlattices to decrease with increasing period length [159, 168]. One of the driving mechanisms for this trend is the formation of minibands (i.e., frequency gaps) in the phonon dispersion and corresponding reductions in the average phonon group velocity as the superlattice period length increases [161, 162, 164, 167].

The predictive power of the BTE- and LD-based approaches is limited due to the assumptions underlying them. Molecular dynamics simulations are a more powerful approach for modeling thermal transport in superlattices because they do not require such assumptions [31, 169–171]. Chen *et al.* applied MD simulations to examine the conditions required to produce a minimum thermal conductivity for LJ superlattices [31]. It was found that a minimum exists when there is no lattice mismatch, but when the species were given a lattice mismatch of 4%, the superlattice thermal conductivity increased monotonically with increasing period length. Daly *et al.* [169] and Imamura *et al.* [170] predicted the effect of interface roughness on the minimum thermal conductivity for a highly simplified model of GaAs/AlAs superlattices.[3] Both groups found that the addition of rough interfaces decreased the superlattice thermal conductivity and removed the minimum that they observed for superlattices with perfect interfaces. Previous MD studies of realistic Si- and Ge-based superlattices have been either limited in scope [40] or have predicted the thermal conductivity of

---

[3]In their model, GaAs was treated as a single atom with a mass equal to the average of the Ga and As masses. A similar approach was used to model AlAs.

a small superlattice fragment rather than the bulk value [172, 173].

6.1.2 Objective

The results of previous experimental and theoretical studies suggest that the superlattice thermal conductivity may be sensitive to deviations from perfect sample quality. In order to guide the design of superlattices with low ZT, it is important that models for predicting superlattice thermal conductivity can account for these deviations [124, 174, 175]. In this chapter, MD simulations are used to examine the effect of interfacial species mixing on the thermal conductivity of two types of realistic $Si/Si_{1-x}Ge_x$ superlattices. For comparison, the thermal conductivities of $Si_{1-x}Ge_x$ alloys are also predicted. Using these predictions, the role of phonon coherence on the thermal transport in superlattices is assessed.

The two types of superlattice examined in this chapter have been experimentally characterized [125, 147]. They are (i) $Si/Si_{0.7}Ge_{0.3}$ superlattices with the Si layer being twice as thick as the alloy layer, and (ii) Si/Ge superlattices with equal Si and Ge layer thicknesses. The 32×16 $Si/Si_{0.7}Ge_{0.3}$ and 24×24 Si/Ge superlattices are shown in Fig. 7.4 along with their period length, L. For both types of superlattice, a range of period lengths similar to those that have been experimentally characterized are considered [125, 147]. Note that the interfaces are parallel to the (001) crystallographic plane (i.e., the xy plane). In all of the samples, the mass and species of each atom are randomly assigned according to the natural isotope abundance [176] for Si or Ge and the desired fraction of Ge, x.

32×16 Si/Si$_{0.7}$Ge$_{0.3}$ Superlattice

$L = 6.55$ nm

24×24 Si/Ge Superlattice

$L = 6.64$ nm

• Si
• Ge

x

In-Plane Directions

Cross-Plane Direction

z

y
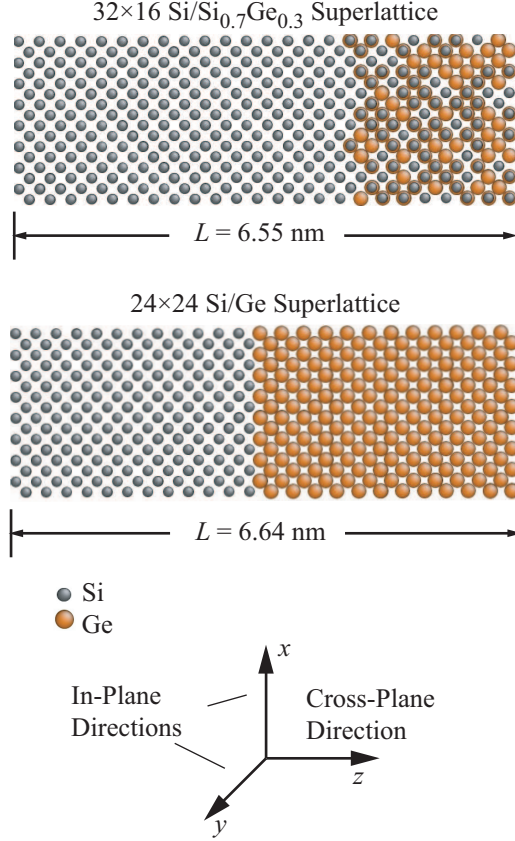
Figure 6.1: One period of the 32×16 Si/Si$_{0.7}$Ge$_{0.3}$ and 24×24 Si/Ge superlattices with perfect interfaces. Reprinted with permission from Ref. [28], Copyright 2009 American Physical Society.

6.2 Sample preparation

6.2.1 Relaxed zero-pressure samples

The thermal conductivity predictions are made using relaxed, zero-pressure samples. The zero-pressure simulation cell dimensions are determined from separate MD simulations run in the NPT ensemble (see Section 2.3) with independent control of stress in each direction. For the Si$_{1-x}$Ge$_x$ alloy, the zero-pressure lattice constant, a, at a temperature of 500 K is approximated to within 0.01% over the entire x range $(0 \leq x \leq 1)$ by

$$a(x) = 5.441 + 0.226x + 0.003x^2 \ [\text{Å}]. \tag{6.1}$$

For the $Si/Si_{1-x}Ge_x$ superlattices, the lattice constant that leads to zero stress in the in-plane directions (the x and y directions) lies between the bulk lattice constants for Si and the $Si_{1-x}Ge_x$ alloy. This configuration results in symmetrically strained superlattices in which the tensile stress in the Si layers balances the compressive stress in the $Si_{1-x}Ge_x$ layers. Due to the in-plane strain within each layer, the lattice constants that lead to zero cross-plane (the z direction) stress are also different than the bulk Si and $Si_{1-x}Ge_x$ alloy lattice constants. The Si layer is negatively strained and the $Si_{1-x}Ge_x$ layer is positively strained in the cross-plane direction. The zero-stress lattice constants obtained from the MD simulations are in good agreement with those predicted from elasticity theory and the SW elastic constants [124].

6.2.2   Interfacial species mixing

Realistic superlattices contain defects due to (i) interfacial species mixing, (ii) epitaxial layer roughening, and (iii) misfit dislocations [124, 174, 175]. In $Si/Si_{1-x}Ge_x$ superlattices, the defects exist to release the strain energy associated with the lattice mismatch between Si and $Si_{1-x}Ge_x$. While each defect type will influence the superlattice thermal conductivity, epitaxial layer roughening and misfit dislocations cannot be directly modeled with MD because they require prohibitively large simulation cells.[4] The effect of interfacial species mixing can be modeled, however, to begin to elucidate the effects that deviations from perfect sample quality have on the nature of the phonon transport in superlattices.

Interfacial species mixing is included in the superlattice samples by randomly assigning the species of each atom in the interface region according to the distribution

$$x(z) = x_L + \frac{1}{2}\left(x_R - x_L\right)\left[1 + \tanh\left(\frac{4z}{D}\right)\right]. \tag{6.2}$$

---

[4]The simulation cell cross-sectional area would need to be increased by a factor of ~40 to model misfit dislocations.

Table 6.1: Molecular dynamics-predicted thermal conductivities for $Si_{1-x}Ge_x$ alloys at a temperature of 500 K.

x	k (W/m-K)
0.125	2.6±0.5
0.250	2.4±0.5
0.375	2.0±0.4
0.500	2.3±0.5
0.625	3.4±0.7
0.750	4.2±0.8
0.875	6.1±1.2

Here, D is the interface thickness (i.e., the thickness of the species mixing region), z is measured relative to the closest interface, and x_L and x_R are the desired unmixed Ge concentrations on the left ($z < 0$) and right ($z > 0$) sides of the interface. The Ge concentration curve produced by Eq. (6.2) is similar in shape to experimental observations for $Si/Si_{1-x}Ge_x$ superlattices [13]. In Sections 6.3.2 and 6.3.3, the thermal conductivities of superlattices with atomically perfect interfaces are compared to those with $D = 2$ monolayers, which results in species mixing primarily in the first monolayer on either side of each interface. For example, in the Si/Ge superlattices, the average compositions of the Si and Ge monolayers on either side of the interface become $Si_{0.88}Ge_{0.12}$ and $Si_{0.12}Ge_{0.88}$.

6.3 Results

6.3.1 $Si_{1-x}Ge_x$ alloy

One way in which the ZT of a $Si/Si_{1-x}Ge_x$ superlattice can be increased above the values associated with the $Si_{1-x}Ge_x$ alloy is for its thermal conductivity to be reduced below that of an alloy with the same Ge concentration. The thermal conductivities of $Si_{1-x}Ge_x$ alloys are therefore predicted to allow for comparison to the predicted superlattice thermal conductivities, which are presented in Sections 6.3.2 and 6.3.3.

The predicted thermal conductivities for the $Si_{1-x}Ge_x$ alloys at a temperature

Figure 6.2: Molecular dynamics-predicted thermal conductivities for $Si/Si_{0.7}Ge_{0.3}$ superlattices (SLs) with perfect interfaces and with interfacial species mixing at a temperature of 500 K. The thermal conductivity of the alloy with identical average composition (the $Si_{0.9}Ge_{0.1}$ alloy) is provided for comparison. Reprinted with permission from Ref. [28], Copyright 2009 American Physical Society.

of 500 K are provided in Table 6.1. The alloy thermal conductivity decreases with increasing Ge concentration until $x = 0.375$, beyond which it increases with increasing Ge concentration. A minimum alloy thermal conductivity for a Ge concentration less than 0.5 is in agreement with experimental measurements for $Si_{1-x}Ge_x$ alloys at a temperature of 300 K (limited experimental data is available at a temperature of 500 K). These predicted alloy thermal conductivities are greater than the values predicted by Skye and Schelling using MD simulation and the SW potential [177]. This difference is attributed to finite cell-size effects present in their predictions (i.e., they did not apply the extrapolation procedure discussed in Section 2.6.4).

6.3.2 $Si/Si_{0.7}Ge_{0.3}$ superlattices

The MD-predicted thermal conductivities for $Si/Si_{0.7}Ge_{0.3}$ superlattices with perfect interfaces and with interfacial species mixing are plotted against the superlattice

period length in Fig. 6.2. The thermal conductivity of an alloy with the same Ge concentration (i.e., the $Si_{0.9}Ge_{0.1}$ alloy, extrapolated from the data in Table 6.1) is provided for comparison. In all cases, the superlattice thermal conductivities are greater than the corresponding alloy value. The superlattice thermal conductivities increase with increasing period length, a trend indicative of incoherent phonon transport and related to decreasing interface density [118, 157]. This result is expected because these superlattices lack perfect periodicity due to the disordered alloy layers, limiting the formation of coherent Bloch phonons to those with low frequency and long wavelengths (i.e., the elastic limit) [178]. In addition, the thermal conductivity of each $Si/Si_{0.7}Ge_{0.3}$ superlattice with perfect interfaces is within the prediction uncertainty of the corresponding structure with interfacial species mixing. This result is attributed to the fact that the $Si/Si_{0.7}Ge_{0.3}$ interfaces are disordered even before the introduction of interfacial species mixing.

The predicted trends of (i) increasing thermal conductivity with increasing period length and (ii) superlattice thermal conductivities greater than the corresponding alloy value are in qualitative agreement with the experimental measurements of Huxtable [147] made at a temperature of 320 K (the highest temperature available) for similar $Si/Si_{0.7}Ge_{0.3}$ superlattices. While the MD predictions and experimental measurements correspond to different temperatures, the data can still be compared because the superlattice thermal conductivity is experimentally observed to depend weakly on temperature above 200 K [147].

6.3.3 Si/Ge superlattices

The predicted thermal conductivities for Si/Ge superlattices with perfect interfaces and with interfacial species mixing are shown in Fig. 6.3 as a function of superlattice
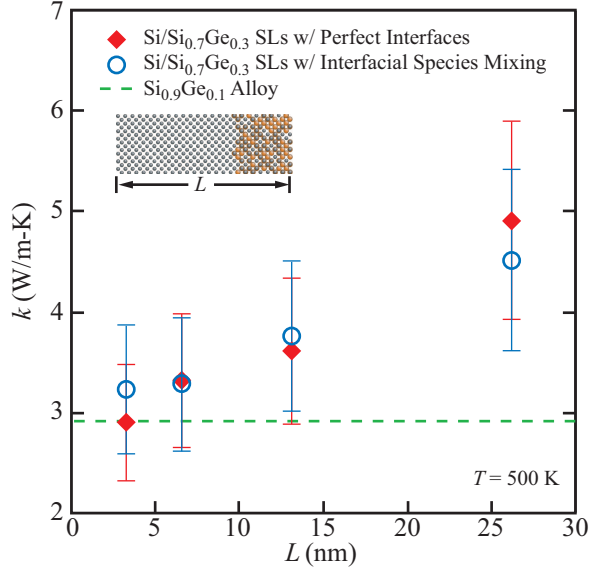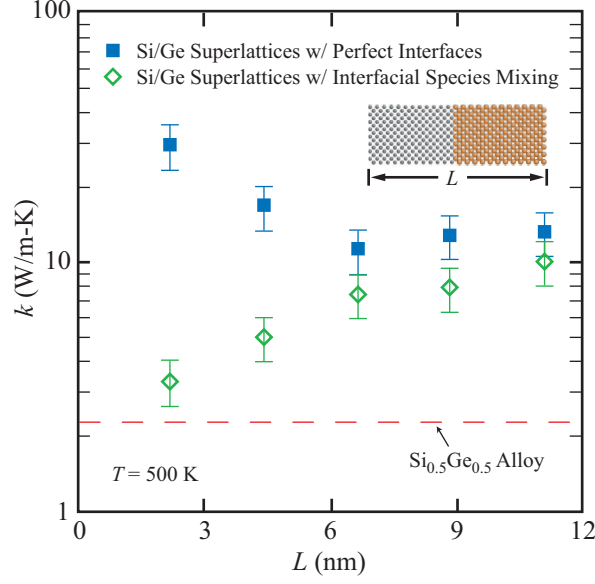
Figure 6.3: Molecular dynamics-predicted thermal conductivities for Si/Ge superlattices with perfect interfaces and with interfacial species mixing at a temperature of 500 K. The thermal conductivity of the $Si_{0.5}Ge_{0.5}$ alloy is provided for comparison. Reprinted with permission from Ref. [28], Copyright 2009 American Physical Society.

period length. The thermal conductivity of the alloy with the same Ge concentration (the $Si_{0.5}Ge_{0.5}$ alloy) is provided for comparison. For Si/Ge superlattices with perfect interfaces, the thermal conductivity is predicted to decrease with increasing period length and then reach a constant value of $\sim$12 W/m-K for period lengths greater than or equal to 6.64 nm. This trend is in qualitative agreement with that calculated by Broido and Reinecke for Si/Ge superlattices with perfect interfaces using an anharmonic LD model under the assumption of coherent phonon transport [159].

The thermal conductivity dependence on period length is different when interfacial species mixing is introduced. The thermal conductivities in this case increase with increasing period length, indicating incoherent phonon transport [118, 157]. In addition, the magnitude of the thermal conductivity decreases by as much as an order of magnitude compared to the samples with perfect interfaces. These findings are consistent with the MD predictions of Daly *et al.* for a simplified model of GaAs/AlAs

superlattices [169]. Note, however, that this level of interfacial species mixing was not found to affect thermal boundary resistance of Si/heavy-Si interfaces, as shown in Fig. 4.4.

Experimental measurements of the thermal conductivity of Si/Ge superlattice thermal conductivity have been made by Borca-Tasciuc *et al.* up to a temperature of 300 K [125]. As with the $Si/Si_{0.7}Ge_{0.3}$ superlattices, the thermal conductivity of Si/Ge superlattices is observed to be independent of temperature above 200 K [125]. The MD-predicted trends can thus be compared to the experimental trends at 300 K by assuming that the thermal conductivity remains temperature-independent up to a temperature of 500 K.

The experimental thermal conductivity of Si/Ge superlattices is observed to decrease with increasing period length [125], a trend similar to that predicted for superlattices in which the phonon transport is coherent [159]. The MD results indicate, however, that even a small deviation from perfect sample quality, which is examined here through the introduction of interfacial species mixing, is sufficient to remove the phonon coherence. It is thus unlikely that coherent phonon-effects are the mechanism leading to the experimentally observed thermal conductivity dependence on period length. Because the energy associated with the lattice-mismatch strain increases with increasing period length, strain induced defects (epitaxial layer roughening and misfit dislocations) will increase with increasing period length [150, 175]. Based on these findings, it is suggested that phonon scattering at an increasing number of these imperfections leads to the experimental trend of decreasing thermal conductivity with increasing period length.

An additional qualitative difference exists between the thermal conductivities predicted using MD simulations and measured experimentally. While the thermal con-

ductivity of Si/Ge superlattices is predicted to be greater than that of the $Si_{0.5}Ge_{0.5}$ alloy, the opposite trend is observed experimentally [125]. As noted by Kim *et al.* [83, 156], superlattice thermal conductivities below the alloy value can be a result of a high density of defects [83, 144, 147, 150, 156]. This statement is consistent with the results of this chapter and the results presented in Chapter VII for the LJ superlattices. For both of these material systems, the predicted thermal conductivities of defect-free superlattices are always greater than the corresponding alloy value.

6.4 Summary

Molecular dynamics simulations have been used to examine the effect of interfacial species mixing on the thermal conductivity of $Si/Si_{0.7}Ge_{0.3}$ and Si/Ge superlattices at a temperature of 500 K. In addition, the thermal conductivities of $Si_{1-x}Ge_x$ alloys were predicted for comparison to the superlattice values.

The thermal conductivity of $Si/Si_{0.7}Ge_{0.3}$ superlattices are predicted to increase with increasing period length and to be above the value of an alloy with the same Ge composition (see Fig. 6.2). These findings are in qualitative agreement with experimental data [147]. The predicted thermal conductivity dependence on period length is indicative of incoherent phonon transport, expected because the disordered alloy layer removes the perfect sample periodicity, thereby preventing the formation of coherent Bloch phonons. The predicted thermal conductivity of each $Si/Si_{0.7}Ge_{0.3}$ superlattice with perfect interfaces is within the prediction uncertainty of the corresponding structure containing interfacial species mixing. This result is due to the internal $Si/Si_{0.7}Ge_{0.3}$ interfaces containing disorder even before the introduction of interfacial species mixing.

The thermal conductivity of Si/Ge superlattices is predicted to depend strongly

on the interface quality. For Si/Ge superlattices with perfect interfaces, the predicted thermal conductivity decreases with increasing period length before reaching a constant value (see Fig. 6.3), a trend similar to that predicted by a LD model under the assumption of coherent phonon transport [159]. When interfacial species mixing is added to the model, however, the thermal conductivity is predicted to increase with increasing period length, a trend indicative of incoherent phonon transport. Because the phonon coherence is removed by deviations from perfect interface quality, it is suggested that the experimental observation [125] of decreasing Si/Ge superlattice thermal conductivity with increasing period length is not due to coherent phonon-effects. In all cases, the thermal conductivity of Si/Ge superlattices is predicted to be greater than that of the $Si_{0.5}Ge_{0.5}$ alloy, a relationship opposite to that observed experimentally. This discrepancy, as well as the experimentally observed thermal conductivity dependence on period length, is suggested to be due to additional phonon scattering at strain-induced defects absent from the MD model.

Due to the predicted sensitivity of the Si/Ge superlattice thermal conductivity on interfacial species mixing, the assumption of coherent phonon transport made in LD models may not be justified. Instead, BTE-based models, which assume incoherent phonon transport, may be more appropriate for modeling thermal transport in superlattices. The *a priori* specification of the nature of the phonon scattering within the superlattice layers and at the internal interfaces required by the BTE-based models, however, is still a limitation for their use in guiding the design of superlattices for low thermal conductivity. Given an accurate interatomic potential, it is believed that MD simulations can provide the required input (e.g., phonon relaxation times and phonon transmission coefficients) for the BTE-based models [86, 87, 116, 179].

CHAPTER VII

Complex superlattice unit cell designs for reduced thermal conductivity

7.1 Introduction

The effect of unit cell design on the thermal conductivity of semiconductor superlattices has been systemically examined in only a few of the experimental and theoretical studies reviewed in Section 6.1.1. In each of these studies, the thermal conductivity dependence on period length was examined for superlattices that contained two layers in the unit cell. Because only a limited number of superlattice designs have been considered, it is likely that the thermoelectric performance potential of superlattices has yet to be fully realized.

In this chapter, MD simulations are used to explore the link between the superlattice unit cell design and the thermal conductivity tensor, and in doing so explore new concepts for the unit cell design. For comparison, the in-plane and cross-plane thermal conductivities for superlattices with two layers of equal thickness in the unit cell are predicted (Section 7.4) and theoretical bounds for the superlattice thermal conductivity are calculated (Section 7.3). With the goal of minimizing the cross-plane thermal conductivity, complex unit cell designs consisting of more than two layers in the unit cell are then examined. It is found that significant reductions ($\sim$17%) in

the cross-plane thermal conductivity are possible over the superlattices with only two layers in the unit cell.

7.2 Superlattice model

The link between the unit cell design and the superlattice thermal conductivity is examined for LJ superlattices. The superlattices contain no defects (i.e., no interfacial species mixing) and are built on face centered cubic lattice sites. The superlattices are comprised of two species, A and B, that differ only in mass. Mass ratios of two and five, spanning a typical range for real superlattices (e.g., the mass ratio between Ge and Si is 2.6), are examined. The atomic interactions are modeled using the LJ 12-6 potential [see Eq. (2.9)]. The simple form of the LJ potential allows for faster simulations than those performed using the SW potential and thus a more thorough examination of the unit cell design space can be made.

The superlattice unit cell is specified using the format: $L_{A,1} \times L_{B,1} \times L_{A,2} \times L_{B,2}$, where L_A and L_B are the thicknesses of individual layers in monolayers. For example, the unit cell for the $1 \times 1 \times 2 \times 2$ superlattice has a repeating sequence of one monolayer of A, one monolayer of B, two monolayers of A, and two monolayers of B. The period length for this case is then $L = 1 + 1 + 2 + 2 = 6$ monolayers. The 3×3 superlattice is shown in Fig. 7.1.

All of the thermal conductivity predictions are made at zero-pressure and a temperature of 40 K, a moderate temperature for LJ argon (melting occurs at 87 K). The cross-plane thermal conductivity is predicted using the direct method. This method is preferred over the Green-Kubo method because of the difficultly of obtaining convergence of the cross-plane HCACF integral for superlattices with complex unit cell designs (see Section 2.5). The Green-Kubo method is used, however, for all predic-

107
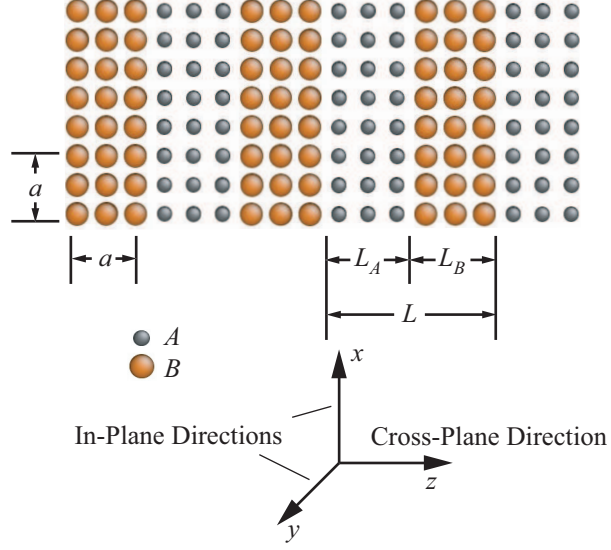
Figure 7.1: Superlattice with cross-plane and in-plane directions labeled. This superlattice is the 3×3 structure, indicating that $L_A = L_B = 3$ monolayers and a period length of $L = 6$ monolayers. Reprinted with permission from Ref. [29], Copyright 2008 American Physical Society.

tions of the in-plane thermal conductivity, for which application of the direct method is impractical due to the large simulation cell sizes that would be required to remove the finite size-effects. The zero-pressure lattice constant at a temperature of 40 K is 5.3697 Å [80] for both superlattice species. This lattice constant corresponds to a thickness of two monolayers (see Fig. 7.1). Because there is no lattice mismatch between the species, the superlattices have zero strain.

7.3   Theoretical bounds on the thermal conductivity

The theoretical upper bound to the superlattice thermal conductivity design space is given by the diffusive limit, reached when the superlattice layer thicknesses are much greater than the phonon mean free paths of the corresponding bulk species. The in-plane and cross-plane thermal conductivities at the diffusive limit, $k_{IP,DL}$ and

$k_{CP,DL}$, are

$$k_{IP,DL} = \frac{t_A k_A + t_B k_B}{t_A + t_B} \tag{7.1}$$

$$k_{CP,DL} = \frac{t_A + t_B}{t_A k_A^{-1} + t_B k_B^{-1} + 2R_{A/B}}, \tag{7.2}$$

where k_A and k_B are the bulk species thermal conductivities, and $R_{A/B}$ is the A/B thermal boundary resistance. The thermal conductivity of bulk species A at a temperature of 40 K was previously predicted using the Green-Kubo method to be 0.467 W/m-K [80]. The thermal conductivity of bulk species B is $m_R^{-1/2}$ times the value for species A. Because an upper limit on the superlattice thermal conductivity is sought, it is assumed for the sake of this calculation that the A/B thermal boundary resistance is negligible compared to the thermal conduction resistance of the individual layers (i.e., t_A/k_A).

A possible lower bound for the superlattice thermal conductivity may be the alloy limit [83]. As mentioned in Sections 6.1.1 and 6.3.3, superlattice thermal conductivities below that of an alloy with similar composition have been measured experimentally [125, 141, 142, 145, 148]. It has been suggested, however, that such results are related to defects generated by the strain associated with lattice mismatch between the superlattice species (e.g., misfit dislocations) [156]. Because the superlattices modeled here have perfect interfaces and no lattice mismatch, one objective of this chapter will be to determine if proper design of the superlattice unit cell alone can lead to thermal conductivities at or below the alloy limit. The alloy thermal conductivity is predicted using the Green-Kubo method and a 256-atom cubic simulation cell. The atoms are located at face centered cubic lattice sites with masses randomly assigned according to a desired species ratio x, given by

$$x \equiv \frac{N_B}{N} = \frac{N - N_A}{N}, \tag{7.3}$$

109

where N is the total number of atoms, and N_A and N_B are the number of atoms of species A and B. The superlattice thermal conductivity will be compared to the thermal conductivity of an alloy with the same species ratio (e.g., the $L_A = L_B$ superlattices are compared to an alloy with $x = 0.5$).

Cahill *et al.* proposed a model for a minimum thermal conductivity, reached when all phonons have a mean free path equal to half of their wavelength [180]. This minimum thermal conductivity, referred to here as the high scatter limit, corresponds to a system with no long-range order. Not surprisingly, the thermal conductivities predicted by this model are in reasonable agreement with experimentally measured thermal conductivities of amorphous materials [180]. Assuming isotropic and linear phonon dispersion curves (i.e., the Debye approxiamtion), classical phonon distributions, and harmonic specific heats, the thermal conductivity at the high-scatter limit, k_{HS}, is

$$k_{HS} = \frac{3}{2}\left(\frac{\pi}{6}\right)^{1/3} k_\mathrm{B} n_v^{2/3} v_{ac}. \tag{7.4}$$

Because the acoustic phonon group velocity for the amorphous LJ phase is not available, this velocity is estimated by scaling the crystalline group velocities [see Eq. (2.29)] by a factor of 0.8 (a typical value for the ratio of the amorphous to crystalline acoustic group velocities for Si and Ge [180, 181]). The superlattice thermal conductivity is compared to the high-scatter limit by calculating v_{ac} for a monatomic crystal that has the same mass density as the superlattice.

7.4 $L_A = L_B$ superlattices

The predicted cross-plane and in-plane thermal conductivities for the $m_R = 2$, $L_A = L_B$ superlattices are shown in Fig. 7.2. The superlattice thermal conductivities are between the alloy and diffusive limits. The thermal conductivity at the high-

scatter limit is 0.102 W/m-K, a value that is below both the superlattice and alloy thermal conductivities. Starting from the diffusive limit, the cross-plane thermal conductivity initially decreases with decreasing period length due to increasing interface density, behavior indicative of incoherent phonon transport. There is a minimum at a period length of $L = 4$ monolayers, beyond which the cross-plane thermal conductivity increases with further decrease in the period length. This minimum indicates a transition from incoherent to coherent phonon transport. In order to examine the statistical significance of this minimum, ten independent simulations of the 2×2 superlattice were run. The results indicate that the prediction is highly repeatable, with an average cross-plane thermal conductivity of 0.197 W/m-K and a standard deviation of 4%. Using the kinetic theory expression for the thermal conductivity [Eq. (5.6)] and assuming that only the acoustic phonon modes contribute significantly to the phonon transport, the phonon mode-averaged mean free path in the superlattices near the minimum is estimated to be ∼5-6 monolayers, a value slightly greater than the period length at the minimum. These results are in agreement with the predictions of Chen *et al.* who found that a minimum exists for LJ $L_A = L_B$ superlattices when the species have no lattice mismatch and that the transition from incoherent to coherent phonon transport occurs when the phonon mean free path becomes greater than or equal to the superlattice period length [31]. A similar dependence between the cross-plane thermal conductivity and the period length is observed for the $m_R = 5$, $L_A = L_B$ superlattices (see Fig. 2.6). The minimum in the cross-plane thermal conductivity has been observed experimentally [148] and predicted using LD calculations [165] and MD simulations [31].

The predicted in-plane to cross-plane thermal conductivity ratio is shown in Fig. 7.3 for the $m_R = 2$ and $m_R = 5$, $L_A = L_B$ superlattices along with corresponding
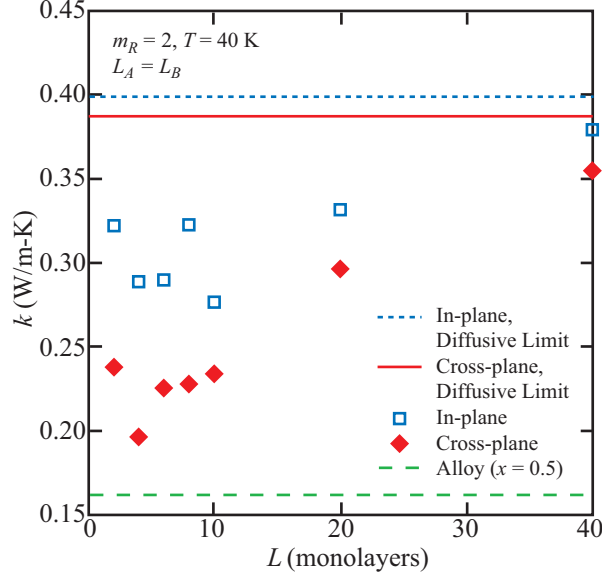
Figure 7.2: Thermal conductivity of the $m_R = 2$, $L_A = L_B$ superlattices in the cross-plane and in-plane directions plotted as a function of period length ($L = L_A + L_B$). The thermal conductivity at the diffusive and alloy limits are also provided for comparison. The thermal conductivity at the high-scatter limit (not shown in figure) is 0.102 W/m-K. Reprinted with permission from Ref. [29], Copyright 2008 American Physical Society.

diffusive-limit values. The thermal conductivity ratio is always greater than the value at the diffusive limit. The maximum in-plane to cross-plane thermal conductivity ratios are ∼1.4 and ∼ 3.6 for the $m_R = 2$ and $m_R = 5$ superlattices, and occur for superlattices with period lengths of four and six monolayers. These period lengths correspond to the region where the phonon transport transitions between the coherent and incoherent regimes.

The thermal conductivity ratios predicted here are lower than values observed experimentally [182] and predicted theoretically [166, 169, 183] for superlattices with similar mass ratios. Yang *et al.* experimentally measured a thermal conductivity ratio of five to six for a Si/Ge superlattice [182]. Using a LD model, Yang and Chen predicted thermal conductivity ratios of five for GaAs/AlAs superlattices [166]. Daly *et al.* predicted thermal conductivity ratios of two to three for model GaAs/AlAs
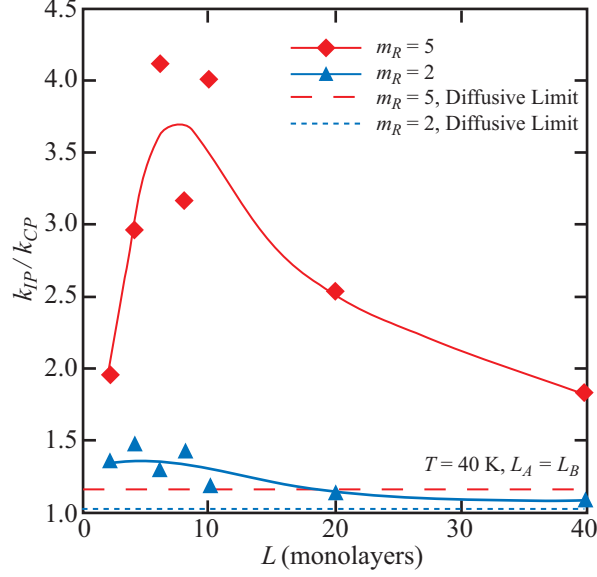
Figure 7.3: In-plane to cross-plane thermal conductivity ratio (k_{IP}/k_{CP}) for the $L_A = L_B$ super-lattices plotted as a function of period length ($L = L_A + L_B$). Solid lines have been added to guide the eye. Reprinted with permission from Ref. [29], Copyright 2008 American Physical Society.

superlattices with perfect interfaces [169, 183]. The lack of strain within the superlattices modeled here (i.e., there is no lattice mismatch) may lead to the smaller thermal conductivity ratios. It is noted that the thermal conductivity ratios predicted here and measured [182] or predicted by others [166, 169, 183] are well below the value of ~30 measured experimentally for layered WSe$_2$ crystals [184, 185].

7.5   Complex unit cell designs

In this section, the effect of unit cell design on the cross-plane thermal conductivity is further explored for the $m_R = 2$ superlattices. Superlattices with $L_A + L_B$ equal to four or ten monolayers, two alloy superlattices, and unit cells with complex designs are considered. Three of these designs are shown in Fig. 7.4. The two alloy superlattices have five layers of an alloy with $x = 0.5$ and five layers of either A or B. Alloy superlattices are considered because similar structures are currently used

113
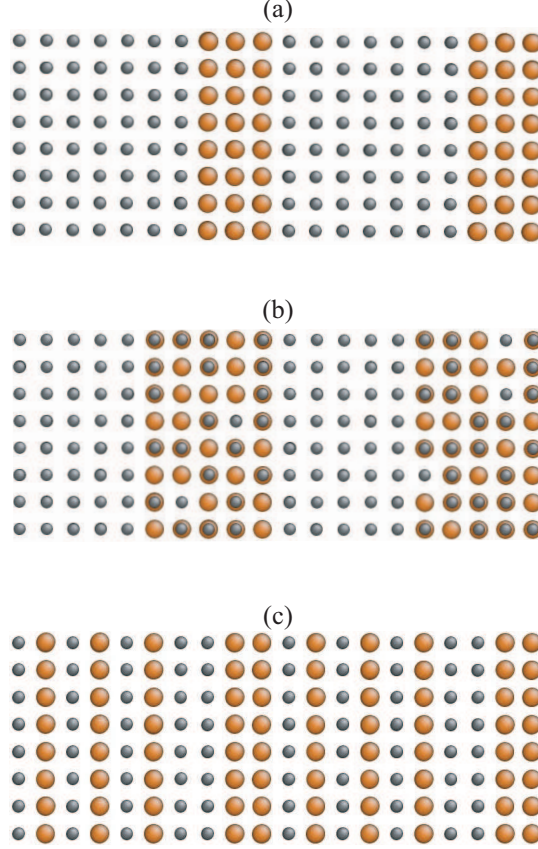
Figure 7.4: Sample superlattice unit cell designs: (a) a 7×3 superlattice (one case in the $L_A + L_B = 10$ series), (b) a superlattice with an alloy layer, and (c) complex design IX [i.e., the $(1 \times 1)_3 \times 2 \times 2$ superlattice, see Table 7.1]. Reprinted with permission from Ref. [29], Copyright 2008 American Physical Society.

in application (e.g., $Si/Si_{1-x}Ge_x$ superlattices [186]). The complex unit cell designs and their labels are listed in Table 7.1. The inclusion of unit cells with more than two layers of varying thicknesses was inspired by earlier work done in the area of phononic crystals [187]. Because the minimum cross-plane thermal conductivity for the $L_A = L_B$ superlattices was observed for the 2×2 superlattice (see Fig. 7.2), the focus of the complex designs is placed on superlattices that have layer thicknesses of one, two, and three monolayers.

Two classes of complex unit cell designs are considered. In the first class (complex designs I through III), the unit cell contains no ordered subcells and has a period

Table 7.1: Complex superlattice unit cell designs and their cross-plane thermal conductivities. All of these structures have $m_R = 2$. Note that a shortened notation is introduced for some of the complex designs. With this notation, the $(1 \times 1)_2 \times 2 \times 2$ superlattice is identical to the $(1 \times 1 \times 1 \times 1 \times 2 \times 2)$ superlattice. For comparison, the thermal conductivity of an alloy with equal amounts of A and B ($x = 0.5$) is 0.162 W/m-K.

	Label	Unit Cell Design	L (monolayers)	x	k_{CP} (W/m-K)
Class I	I	$1 \times 2 \times 2 \times 1 \times 1 \times 3$	10	0.600	0.191
	II	$2 \times 1 \times 3 \times 3 \times 2 \times 3$	14	0.500	0.199
	III	$2 \times 3 \times 1 \times 3 \times 2 \times 1 \times 1 \times 1 \times 3 \times 1$	18	0.500	0.204
Class II	IV	$1 \times 1 \times 2 \times 2$	6	0.500	0.171
	V	$1 \times 1 \times (2 \times 2)_2$	10	0.500	0.171
	VI	$1 \times 1 \times (2 \times 2)_3$	14	0.500	0.167
	VII	$1 \times 1 \times (2 \times 2)_4$	18	0.500	0.163
	VIII	$(1 \times 1)_2 \times 2 \times 2$	8	0.500	0.174
	IX	$1 \times 1 \times 1 \times 2 \times 1 \times 2$	8	0.625	0.179
	X	$1 \times 1 \times 2 \times 1 \times 2 \times 1$	8	0.375	0.168
	XI	$(1 \times 1)_3 \times 2 \times 2$	10	0.500	0.164
	XII	$(1 \times 1)_5 \times 2 \times 2$	14	0.500	0.180

length greater than the phonon mean free path ($\sim$5-6 monolayers, see Section 7.4). The phonon transport in these structures is thus incoherent and the cross-plane thermal conductivity may be reduced by phonon scattering at interfaces. In the second class (complex designs IV through XII), the unit cell is a 1×1 or 2×2 superlattice with disruptions spaced on the order of the phonon mean free path (e.g., the 1×1 subcell in design VII is a disruption in what would otherwise be a 2×2 superlattice). Because of phonon scattering at these disruptions, the phonon mean free paths and thermal conductivities may be below the values that would exist in the 1×1 and 2×2 superlattices. It is noted that a third class of designs exists in which the unit cell contains many layers with no ordered subcells but has a period length less than or equal to the phonon mean free path. Within this class, the phonon transport is coherent and the phonon dispersion may be tuned to reduce the phonon group velocity, leading to low thermal conductivity. This class of designs cannot be examined here, however, because the transition between the regimes of coherent to incoherent phonon transport, which provides an estimate for the mean free path, occurs at a
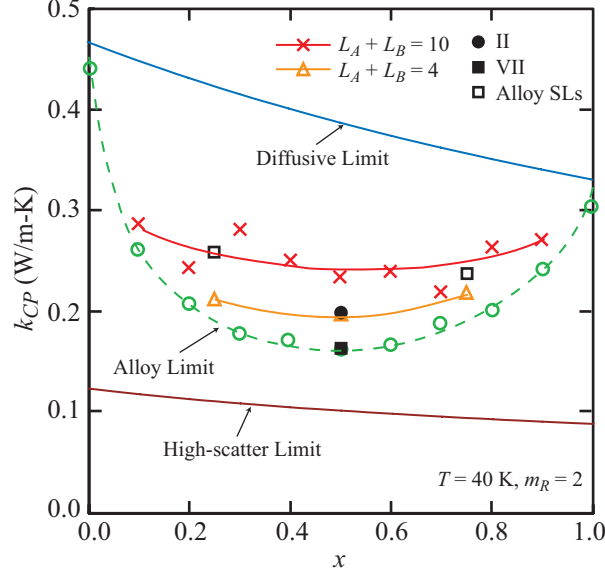
Figure 7.5: Cross-plane thermal conductivity (k_{CP}) design space for the $m_R = 2$ superlattices. The complex unit cell designs are defined in Table 7.1. Reprinted with permission from Ref. [29], Copyright 2008 American Physical Society.

small period length, leaving little room for design.[1]

The results for some of these superlattices are plotted against the sample species ratio (x) in Fig. 7.5. Note that only complex designs II and VII are plotted in Fig. 7.5 (the cross-plane thermal conductivities for all of the considered complex unit cell designs are provided in Table 7.1). As with the $L_A = L_B$ structures, the predicted cross-plane thermal conductivities are above the high-scatter limit and below the diffusive limit. The cross-plane thermal conductivities of the $L_A + L_B = 4$ and $L_A + L_B = 10$ superlattices are not strongly dependent on the ratio of L_A to L_B. The thermal conductivities of the alloy superlattices follow the trend of the $L_A + L_B = 10$ superlattices even though the alloy layers have a larger thermal conduction resistance than the bulk A or B layers. This result is due to the reduction in the thermal boundary resistance of the superlattice interfaces (i.e., the acoustic mismatch between

---

[1]To explore this class of designs, one may consider lower temperatures, which would increase the average phonon mean free path and shift the location of the minimum thermal conductivity to a superlattice with a larger period length.

116

the superlattice species is less in the alloy superlattices than in the $A|B$ superlattices). Complex design II has a cross-plane thermal conductivity of 0.199 W/m-K, a value that is within the measurement uncertainty of the value for the 2×2 superlattice (0.197 W/m-K). Complex design VII, however, has a cross-plane thermal conductivity of 0.163 W/m-K, a value that is in the vicinity of the alloy limit and $\sim 17\%$ less than that of the minimum observed for the $L_A = L_B$ superlattices.

From the results shown in Table II, disordered, multilayer unit cells with lengths larger than the phonon mean free path (complex designs I through III) are found to be ineffective in reducing the cross-plane thermal conductivity below the value for the 2×2 superlattice. The results indicate, however, that the complex designs with unit cells that are 1×1 or 2×2 superlattices with disruptions (complex designs IV through XII) all have cross-plane thermal conductivities below the value for the 2×2 superlattice. None of these designs, however, have a thermal conductivity below the alloy limit. It is noted that due to measurement uncertainty no clear trend in the cross-plane thermal conductivity within complex designs IV through XII can be resolved.

The low thermal conductivities observed for complex designs IV through XII are attributed to reductions in both the phonon group velocities and phonon mean free paths in the regime where the phonon transport has both coherent and incoherent qualities. Because the phonon transport is coherent in the 1×1 and 2×2 superlattices, the phonon group velocities are reduced compared to those of the bulk materials [159, 161, 162, 164, 167]. The thermal conductivity is then further reduced by adding disruptions to these structures. These disruptions decrease the phonon mean free path below the value that would exist for the normal 1×1 and 2×2 superlattices while maintaining the low group velocities associated with those structures.

117

7.6 Summary

Molecular dynamics simulations were used to explore the link between the unit cell design and the thermal conductivity tensor for LJ superlattices with species that differ in mass by ratios of two and five. For the $L_A = L_B$ superlattices, a minimum is predicted in the cross-plane thermal conductivity for superlattices with period lengths corresponding to the transition between coherent and incoherent phonon transport regimes. This finding is in agreement with previous theoretical predictions and some experimental observations. A maximum in the in-plane to cross-plane thermal conductivity ratio was also observed near this transition.

Complex unit cell designs (characterized by having more than two layers in the unit cell) were explored to see if the cross-plane thermal conductivity could be reduced below the minimum observed for the $L_A = L_B$ superlattices. Two different classes of complex unit cell designs were considered. In the first class, the unit cell contains many layers with no ordered subcells and has a length greater than the phonon mean free path. These designs were found to be ineffective in reducing the cross-plane thermal conductivity. In the second class of complex designs, the unit cell contained 1×1 or 2×2 subcells with disruptions spaced on the order of the phonon mean free path. Several of these complex designs were found to have cross-plane thermal conductivities as low as the alloy limit, 17% below the minimum value for the $L_A = L_B$ superlattices. This finding provides a new design concept for fabricating superlattices with potentially very low thermal conductivity, required in thermoelectric applications.

CHAPTER VIII

Conclusion

8.1 Contributions

The impediment to thermal transport resulting from phonon scattering at solid-solid interfaces is a significant challenge associated with the design of advanced technological devices such as quantum cascade lasers and CMOS transistors. Further improvements in the design of these devices and the continued miniaturization of microelectronics require a detailed understanding of thermal transport at the phonon-level. This understanding will also allow for improvements in the design of nanostructured semiconductors (e.g., superlattices) with low thermal conductivity, and thus, the potential for high ZT.

In this thesis, thermal transport across semiconductor interfaces, thin films, and superlattices was examined using MD simulation and harmonic LD calculations. Molecular dynamics simulation naturally account for the combined effects of diffusive and ballistic phonon transport, an advantage over modeling techniques rooted in the Fourier law, which assume only diffusive transport. This method also requires no specification of the phonon properties *a priori*, an advantage over modeling techniques rooted in the BTE. Lattice dynamics calculations of the phonon frequencies, group velocities, and transmission coefficients allowed the details of the thermal transport

to be resolved at the phonon mode-level.

The work presented in this thesis has made the following contributions towards the understanding of phonon transport across semiconductor interfaces, thin films, and superlattices:

- *Deviations from the bulk phonon distribution near an interface.* The accuracies of two theoretical expressions for thermal boundary resistance were assessed in Chapter IV by comparing their predictions to independent predictions from MD simulations. In one expression (R_E), the phonon distributions are assumed to follow the equilibrium distribution, while in the other expression (R_{NE}), the phonons are assumed to have nonequilibrium, but bulk-like distributions. These expressions were evaluated using LD-predicted phonon properties. At temperatures where the phonon scattering is elastic, R_E is in good agreement with the corresponding MD-predicted values for a Si/Ge interface and a series of Si/heavy-Si interfaces with mass ratios greater than two. When applied to a system containing no interface, however, R_E is erroneously nonzero. While R_{NE} is zero for a system containing no interface, it is 40-60% less than the corresponding MD-predicted values for the Si/Ge interface and the Si/heavy-Si interfaces. This inaccuracy was attributed to deviations from the bulk phonon distributions that result from the phonon creation and annihilation processes that are associated with the phonon-interface scattering. Prior to this work, this inaccuracy has been masked by the many sources of uncertainty when comparing theoretical predictions to experimental measurements.

- *Phonon mode-dependent transition from ballistic to diffusive transport in thin films.* The thickness-dependence of the thermal resistance of Ge/Si/Ge and

Si/Ge/Si thin film structures was examined in Chapter V using MD simulations and theoretical calculations. When the film thickness is between 2 nm and 30 nm, the thermal resistances are thickness-independent for the Ge/Si/Ge structures and increase with increasing film thickness for the Si/Ge/Si structures. These results were attributed to phonon transport that is ballistic in the Ge/Si/Ge structures and more diffusive in the Si/Ge/Si structures. The standard approach of comparing the mode-averaged phonon mean free path to the film thickness was found to be incapable of predicting this difference between the structures. The correct prediction was made, however, when the frequency-dependence of the phonon mean free paths was considered (see Fig. 5.6). This finding suggests that the mode-specific details of the phonon transport need to be retained in order to develop reliable models for nanoscale thermal transport.

- *Sensitivity of the superlattice thermal conductivity to interface quality.* Realistic superlattices contain defects due to interfacial species mixing, epitaxial layer roughening, and misfit dislocations. As a step towards understanding how these deviations from perfect sample quality affect phonon transport in superlattices, MD simulations were used in Chapter VI to examine the effect of interfacial species mixing on the thermal conductivity of $Si/Si_{1-x}Ge_x$ superlattices. Adding species mixing to an otherwise perfectly periodic Si/Ge superlattice was found to remove the phonon coherence, leading to an order of magnitude decrease in the thermal conductivity and altering its dependence on period length. The extreme sensitivity of the Si/Ge superlattice thermal conductivity to interfacial species mixing suggests that the assumption of coherent phonon transport made in LD-based models may not be justified.

The work presented in this thesis has also made a contribution in the available strategies for designing superlattices with low thermal conductivity:

- *Identification of a new concept for superlattice design.* Previous experimental and theoretical studies of thermal transport in superlattices have only considered superlattices with two layers in the unit cell (i.e., an A/B/A/B/A/B... structure). In Chapter VII, the link between the supperlattice unit cell design and the thermal conductivity tensor was explored for LJ superlattices using MD simulations. A new class of complex, multilayered unit cell designs was found to reduce the cross-plane thermal conductivity by 17% compared to the minimum value predicted for superlattices with only two layers in the unit cell. The low thermal conductivities were attributed to reductions in both the phonon group velocities and phonon mean free paths in the regime where the phonon transport has both coherent and incoherent qualities. The identification of this new concept for superlattice unit cell design suggests that the thermoelectric performance potential of superlattices has yet to be fully realized.

8.2 Suggestions for future study

Five suggestions for future study are:

- To improve the accuracy of the models for predicting thermal boundary resistance, a method for predicting the nonequilibrium phonon distributions near an interface should be developed. In theory, these distributions can be obtained by solving the BTE while incorporating the interface scattering processes into the collision term. Proper formulation of these processes is nontrivial and will be crucial in order to obtain meaningful results. The procedure used to solve the BTE may also be complicated by the potential inaccuracy of the relaxation time

approximation near the interface. Under this approximation, only the phonon mode of interest is assumed to be out of equilibrium [79], which is reasonable for systems that are not far from equilibrium [89] but questionable near the interface due to the abrupt temperature drop. If such inaccuracy exists, a variational approach will be required to solve the BTE [79].

- As discussed in Section 4.4.1, the Si/Ge thermal boundary resistance is predicted to decrease with increasing temperature above a temperature of 500 K. This trend is attributed to the effects of inelastic phonon scattering at the interface, which increases the available channels for thermal conductance. Future study should focus on attaining an understanding of these effects so that a model for predicting thermal boundary resistance at all temperatures can be developed. One method for probing these effects is based on the nonequilibrium Green's function [188]. To date, however, calculations using this method have only been performed for one-dimensional systems due to computational expense [92, 94, 189]. Nevertheless, it is likely that some insight can be gained from these one-dimensional systems that will be useful in developing models for inelastic scattering at an interface.

- The accuracy of any MD- or LD-predicted property is limited by the accuracy of the interatomic potential function. While *ab initio* approaches for modeling the atomic interactions are computationally expensive, they are becoming more tractable as processing power increases and methods for improved scalability are developed [36, 37]. Future study should take advantage of the tremendous predictive power associated with *ab initio* approaches to allow accurate comparison between theoretically predicted and experimentally measured thermal transport

properties.

- The nature of phonon transport across a single interface is much different than that across a system containing two interfaces (i.e., a thin film structure) or infinitely many interfaces (i.e., a bulk superlattice). For example, interfacial species mixing was found to have little effect on the thermal boundary resistance of the Si/heavy-Si interfaces but strongly influenced the thermal conductivity of the Si/Ge superlattices (see Figs. 4.4 and 6.3). The structures encountered in many applications (e.g., quantum cascade lasers and light-emitting diodes [1–3]), however, often contain more than one or two interfaces but too few interfaces to have the thermal transprot properties of a superlattice. To develop models for predicting the thermal transport in these structures, the transition in the nature of the phonon transport between structures containing small and large numbers of interfaces should be studied. Of particular interest will be identifying the number of interfaces required for the structure's thermal transport properties to be well-approximated by those of a bulk superlattice.

- In Chapter VII, a new class of superlattice unit cell designs was identified and found to have thermal conductivities below the minimum value predicted for superlattices with only two layers in the unit cell. This finding should be validated experimentally. A sample unit cell for this validation is

$$A/B/A/B/A/B/A/B/C. \tag{8.1}$$

The A/B portion of the unit cell is a small period superlattice fragment in which the phonon transport is coherent, and thus, has a low average phonon group velocity. This superlattice fragment must be of high quality due to the sensitivity of the phonon coherence to deviations from perfect sample quality

(see Chapter VI). The C portion of the unit cell is a disruption that is added to reduce the phonon mean free paths below the value associated with a bulk A/B superlattice. One suggested material system for this validation is GaAs- and AlAs-based superlattices due to the small (0.25%) lattice mismatch between GaAs and AlAs, which allows the fabrication of high-quality samples. Another suggestion is to use a Si/Ge superlattice for the A/B portion of the unit cell and a $Si_{0.5}Ge_{0.5}$ alloy for the disruption, which may allow some of the strain energy associated with the lattice mismatch between Si and Ge to be relieved.

APPENDICES

APPENDIX A

Explanation for the strong oscillations in the heat current autocorrelation function

Strong oscillations exist in the LJ superlattice HCACF when the heat current definition given by Eq. (2.13) is applied. The cross-plane HCACF for the $m_R = 2$, 3×3 LJ superlattice is shown in the inset of Fig. A.1(a) as an example. Similar oscillations have been observed in studies of diamond-structured materials [62], monolayer superlattices [66], complex silica structures [67], metal organic framework-5 [63], germanium clathrate structures [64], CaF_2 and UO_2 [65], and carbon nanotubes [68]. It has been previously suggested that these oscillations are related to zero-wavevector optical phonon modes [66]. Here, a criterion based in LD calculations that can predict the specific phonon modes that create these oscillations is derived and tested.

Applying the chain rule to Eq. (2.13) leads to

$$\mathbf{S}_1 = \sum_i \frac{d\mathbf{r}(i)}{dt} e_i + \sum_i \mathbf{r}(i) \frac{de_i}{dt}. \tag{A.1}$$

Defining the first and second terms on the right hand side of Eq. (A.1) as $\mathbf{S}_u(t)$ and $\mathbf{S}_k(t)$, terms, the HCACF can be written as

$$
\begin{aligned}
\langle \mathbf{S}_1(t) \cdot \mathbf{S}_1(0) \rangle \quad = \quad & \langle \mathbf{S}_k(t) \cdot \mathbf{S}_k(0) \rangle \tag{A.2} \\
& + \quad 2\langle \mathbf{S}_k(t) \cdot \mathbf{S}_u(0) \rangle + \langle \mathbf{S}_u(t) \cdot \mathbf{S}_u(0) \rangle,
\end{aligned}
$$
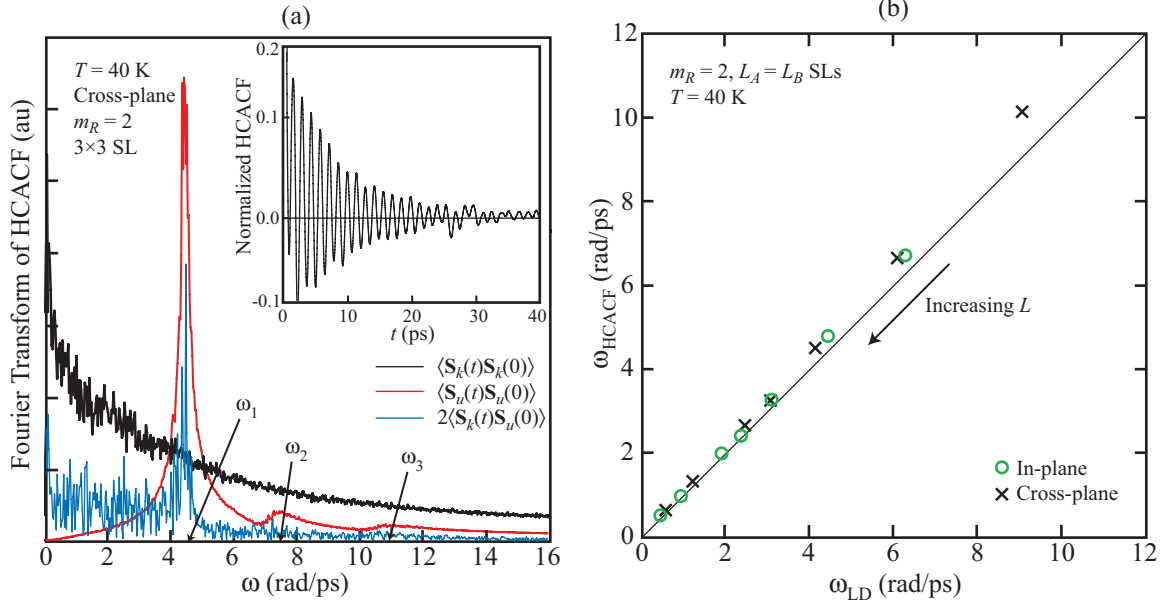
Figure A.1: (a) Inset: Cross-plane HCACF for the $m_R = 2$, 3×3 LJ superlattice obtained using the definition of the heat current given by Eq. (2.13). Body: Power spectrum of the Fourier transform of the decomposed HCACF [see Eq. (A.3)] shown in the inset. (b) Primary peak in the Fourier transform of the HCACF plotted against the peak predicted from the LD calculation for all of the $L_A = L_B$ LJ superlattices in both the in-plane and cross-plane directions. Reprinted with permission from Ref. [29], Copyright 2008 American Physical Society.

where there are individual contributions to the HCACF resulting from $\mathbf{S}_u(t)$, $\mathbf{S}_k(t)$, and their cross terms. The power spectrum of the Fourier transform of these quantities is shown in Fig. A.1(a) for the $m_R = 2$, 3×3 LJ superlattice (the same structure whose HCACF is shown in the inset). It is clear that the oscillations in the HCACF are primarily due to the autocorrelation of the $\mathbf{S}_u(t)$ term.

In a solid, the position of an atom can be written as

$$\mathbf{r}(i,t) = \mathbf{r}_o(i) + \mathbf{u}(i,t). \tag{A.3}$$

Under the harmonic approximation, $\mathbf{u}(i,t)$ is given by [88]

$$\mathbf{u}(i,t) = \mathbf{u}(jk,t) = \frac{1}{N^{1/2}} \sum_{\boldsymbol{\kappa},\nu} \mathbf{U}(j,\boldsymbol{\kappa},\nu) \tilde{Q}(\boldsymbol{\kappa},\nu,t) \exp\{i[\boldsymbol{\kappa} \cdot \mathbf{r}(jk)]\}. \tag{A.4}$$

Here, the summation is over all phonon modes, N is the number of atoms in the

system, atom i is the jth atom in the kth unit cell, and $\tilde{Q}(\boldsymbol{\kappa}, \nu, t)$ is the normal mode coordinate, given by [60]

$$\tilde{Q}(\boldsymbol{\kappa}, \nu, t) = Q(\boldsymbol{\kappa}, \nu) \exp[-i\omega(\boldsymbol{\kappa}, \nu)t], \tag{A.5}$$

where $Q(\boldsymbol{\kappa}, \nu)$ is the normal mode amplitude. Equations (A.3) and (A.4) can be used with the definition of $\mathbf{S}_u(t)$ to obtain

$$\mathbf{S}_u(t) = \frac{1}{N^{1/2}} \sum_{\boldsymbol{\kappa}, \nu} \sum_{j,k} e_{jk} \mathbf{U}(j, \boldsymbol{\kappa}, \nu) \frac{d\tilde{Q}(\boldsymbol{\kappa}, \nu, t)}{dt} \exp\{i[\boldsymbol{\kappa} \cdot \mathbf{r}(jk)]\}, \tag{A.6}$$

where the summations are over all atoms and phonon modes. Because

$$\sum_k \exp\{i[\boldsymbol{\kappa} \cdot \mathbf{r}(jk)]\} = 0 \tag{A.7}$$

for all phonon modes with nonzero wave vector, only phonon modes with zero wave vector will significantly contribute to the summation in Eq. (A.6). Therefore, Eq. (A.6) can be approximated as

$$\mathbf{S}_u(t) \approx \frac{N_{uc}}{N^{1/2}} \sum_{\nu} \sum_j \bar{e}_j \mathbf{U}(j, \nu) \frac{d\tilde{Q}(\nu, t)}{dt}, \tag{A.8}$$

where the dependence on $\boldsymbol{\kappa}$ has been dropped because the summation is now restricted to modes with zero wave vector, $\bar{e}_j$ is the average energy of all of the jth atoms in each unit cell, and N_{uc} is the number of unit cells.

Substituting the time derivative of Eq. (A.5) into Eq. (A.8) and taking the auto-correlation of the result gives

$$\langle \mathbf{S}_u(t) \cdot \mathbf{S}_u(0) \rangle = \frac{N_{uc}^2}{N} \sum_{\nu} \omega^2(\nu) Q^2(\nu) \left[\sum_j \bar{e}_j \mathbf{U}(j, \nu) \right]^2 \cos[\omega(\nu)t]. \tag{A.9}$$

For a classical system, the expectation value of the square of the phonon normal mode coordinate is [88]

$$\langle |\tilde{Q}(\boldsymbol{\kappa}, \nu, t)|^2 \rangle = \frac{k_{\mathrm{B}}T}{\omega^2(\nu)}. \tag{A.10}$$

This quantity is a factor of two smaller than the square of the phonon normal mode amplitude, i.e.,

$$Q^2(\nu) = \frac{\langle |\tilde{Q}(\boldsymbol{\kappa}, \nu, t)|^2 \rangle}{2}. \tag{A.11}$$

Combining Eqs. (A.9)-(A.11) gives

$$\langle \mathbf{S}_u(t) \cdot \mathbf{S}_u(0) \rangle = \frac{k_{\mathrm{B}} T N_{uc}^2}{N} \sum_{\nu} \left[\sum_j \bar{e}_j \mathbf{U}(j, \nu) \right]^2 \cos[\omega(\nu)t]. \tag{A.12}$$

Equation (A.12) is a sum of oscillatory functions corresponding to optical phonon modes with zero wave vector. The summation over j can be used as a criterion for when a peak should exist in the Fourier transform of the HCACF. That is, when

$$\left[\sum_j \bar{e}_j \mathbf{U}(j, \nu) \right]^2 \neq 0, \tag{A.13}$$

the Fourier transform of the HCACF will have a peak at $\omega(\nu)$. The relative peak amplitudes should also be related to the magnitude of the term on the left hand side of Eq. (A.13).

Using the quasi-harmonic approximation,[1] the zero wave vector phonon mode polarizations and frequencies have been calculated for all of the $L_A = L_B$ LJ superlattices considered in Chapter VII, and Eq. (A.13) has been evaluated to predict the frequency peaks in the Fourier transform of the HCACF. For the $m_R = 2$, 3×3 LJ superlattice, a strong peak is predicted for $\omega_1 = 4.15$ rad/ps, a value 8% lower than the dominant peak frequency of $\omega_1 = 4.49$ rad/ps [see Fig. A.1(a)]. Two additional peaks are predicted for $\omega_2 = 6.80$ rad/ps and $\omega_3 = 9.77$ rad/ps. The values of the term on the left hand side of Eq. (A.13) for these peaks are 16 and 31 times less than the value for the primary peak. These weak secondary and tertiary peaks can also be observed in Fig. A.1(a) at frequencies of $\omega_2 = 7.5$ rad/ps and $\omega_3 = 10.9$ rad/ps.

---

[1] In the quasi-harmonic approximation, the crystal anharmonicity is assumed to affect only the thermal expansion of the crystal [88]. The calculations are performed using the methodology that is presented in Chapter III with zero-pressure lattice constants at a finite temperature rather than at zero-temperature.

The primary peaks in the Fourier transform of the cross-plane and in-plane HCACFs (ω_{HCACF}) for all of the $m_R = 2$, $L_A = L_B$ LJ superlattices are compared to values predicted by the LD calculation (ω_{LD}) in Fig. A.1(b). The maximum difference between the predicted and observed peak frequencies is 11% for the $m_R = 2$, 1×1 LJ superlattice in the cross-plane direction. The source of this error is believed to be the lack of anharmonic terms in the LD calculations. To prove this point, a simulation was run at a temperature of 10 K for the $m_R = 2$, 3×3 LJ superlattice, and the prediction accuracy of the primary cross-plane peak improved from 8% to 1%.

The procedure outlined in this appendix was also successful in predicting the phonon modes that lead to the oscillations in the HCACF reported for several complex silica structures [67]. Because all of the other studies [62–66, 68] that have observed similar oscillations in the HCACF used the heat current definition given by Eq. (2.13), it is believed that the peaks observed in those studies are also related to the autocorrelation of the $\mathbf{S}_u(t)$ term and can be predicted using the procedure outlined here or omitted by choosing the $\mathbf{S}_2$ heat current definition [Eq. (2.14)].

APPENDIX B

Length-dependent thermal conductivity model

In this appendix, a model to describe the length dependence of the thermal conductivity is derived. This model is then used to develop a metric for determining the sample lengths required to generate accurate bulk thermal conductivity predictions using the direct method and the linear extrapolation procedure (see Section 2.6.4).

The derivation begins with the expression for the thermal conductivity of a crystal obtained by solving the BTE under the relaxation time approximation. This expression is [38,79]

$$k = \sum_{\boldsymbol{\kappa}} \sum_{\nu} c_{ph} v_z^2 \tau, \tag{B.1}$$

where the summations are over all modes, and the volumetric specific heat of each mode, c_{ph}, is equal to $c_{ph} = k_{\mathrm{B}}/V$ in the classical limit. The summation over the wave vectors in Eq. (B.1) can be converted to an integral over the first Brillouin zone when the system contains enough phonon modes to fully resolve the Brillouin zone. This condition is met in the direct method simulation cell because it is larger than the cells found to generate size-independent thermal conductivity predictions with the Green-Kubo method (see Tables 2.3 and 2.4), in which the primary source of size-dependence is the Brillouin zone resolution. In the classical limit, the thermal

conductivity can therefore be written as

$$k = \frac{1}{8\pi^3} \sum_\nu \int k_\text{B} v_z^2 \tau d\boldsymbol{\kappa}.$$

(B.2)

In the direct method, the dependence of the thermal conductivity on sample length arises due to phonon scattering at the sample boundaries. This effect can be modeled using the Matthiessen rule, which combines the relaxation times associated with intrinsic phonon scattering and phonon-boundary scattering under the assumption that they are independent. Possible sources of intrinsic phonon scattering are phonon-phonon scattering, phonon-electron scattering, and phonon scattering at defects and internal interfaces [38, 79]. Here, however, it is assumed that the crystal contains no defects, free electrons, or internal interfaces. The relaxation time associated with the intrinsic phonon scattering is thus equal to the relaxation time associated with phonon-phonon scattering, τ_p, and the effective relaxation time is [79]

$$\frac{1}{\tau} = \frac{1}{\tau_p} + \frac{1}{\tau_b}.$$

(B.3)

Here, τ_b is the mode-dependent relaxation time associated with phonon-boundary scattering, which is assumed to be equal to the average time between boundary scattering events in the absence of intrinsic scattering, i.e.,

$$\tau_b = \frac{L_S}{2|v_{g,z}|},$$

(B.4)

where L_S is the sample length. Substituting Eqs. (B.3) and (B.4) into Eq. (B.2) yields

$$k(L_S) = \frac{1}{8\pi^3} \sum_\nu \int k_\text{B} v_{g,z}^2 \tau_p \left[1 + \frac{2|v_{g,z}|\tau_p}{L_S} \right]^{-1} d\boldsymbol{\kappa}.$$

(B.5)

For convenience, Eq. (B.5) is converted from Cartesian coordinates to spherical co-

ordinates, resulting in

$$k(L_S) = \frac{1}{8\pi^3} \sum_\nu \int_0^{\kappa_{BZ}(\theta,\phi)} \int_0^{2\pi} \int_0^\pi k_\mathrm{B} |\mathbf{v}_g \cos\theta|^2 \tau_p \left[1 + \frac{2|\mathbf{v}_g \cos\theta|\tau_p}{L_S} \right]^{-1} \kappa^2 \sin\theta d\theta d\phi d\kappa,$$

(B.6)

where $\kappa = |\boldsymbol{\kappa}|$, and $\kappa_{BZ}(\theta, \phi)$ is the magnitude of the wave vector at the first Brillouin zone boundary along the θ, ϕ-direction.

To simplify Eq. (B.6), it is assumed that the optical modes make negligible contribution to the thermal conductivity. In addition, the Debye approximation is made in which the dispersion curves for all of the acoustic phonons are given by $\omega = v_{ac}\kappa$, where v_{ac} is a representative group velocity of the acoustic phonons. This approximation results in a spherical Brillouin zone. Under these assumptions, Eq. (B.6) can be written as

$$k(L_S) = \frac{3}{8\pi^3} \int_0^{\omega_D} \int_0^{2\pi} \int_0^\pi \frac{k_\mathrm{B}\omega^2 \cos^2\theta}{v_{ac}} \left[1 + \frac{2|\mathbf{v}_g \cos\theta|\tau_p}{L_S} \right]^{-1} \sin\theta d\theta d\phi d\omega, \quad \text{(B.7)}$$

where the integral over κ has been transformed to an integral over ω. The upper limit of the integral over frequency, ω_D, is the Debye frequency, which is [88]

$$\omega_D = v_{ac} \left(\frac{6\pi^2}{\Omega} \right)^{1/3}, \quad \text{(B.8)}$$

where Ω is the volume of the primitive cell.

It is assumed that τ_p follows the form derived by Callaway for long-wavelength phonons, which is [123]

$$\tau_p = \frac{A}{\omega^2}, \quad \text{(B.9)}$$

where the proportionality constant A is found from the bulk thermal conductivity to be

$$A = \frac{2\pi^2 v_{ac} k_\infty}{k_\mathrm{B}\omega_D}. \quad \text{(B.10)}$$

Substituting Eqs. (B.9) and (B.10) and integrating over θ, ϕ, and ω yields

$$\frac{k(l)}{k_\infty} = \frac{6}{7} + \frac{3}{14}l - \frac{3}{7}l^2 + \frac{3}{7}l^3 \ln\left(1 + \frac{1}{l}\right) - \frac{6}{7\sqrt{l}}\arctan\left(\sqrt{l}\right),$$ (B.11)

where l is a non-dimensional length defined as

$$l = \frac{3k_{\mathrm{B}}v_{ac}L_S}{2k_\infty\Omega}.$$ (B.12)

In the limit of $L_S \to \infty$, the right hand side of Eq. (B.11) approaches unity and thus, $k \to k_\infty$. Using this model for the length-dependent thermal conductivity, the accuracy of the linear extrapolation procedure is now explored. The estimated bulk thermal conductivity from the linear extrapolation procedure (k_∞^{est}) is obtained by dropping the second- and higher-order terms from Eq. (2.27), resulting in

$$\frac{k_\infty^{est}(l)}{k_\infty} = \frac{\dfrac{1}{k_\infty}}{\dfrac{1}{k} + \dfrac{\partial\left(\dfrac{1}{k}\right)}{\partial\left(\dfrac{1}{l}\right)}\left(\dfrac{-1}{l}\right)}.$$ (B.13)

The thermal conductivity [Eq. (B.11)] and the bulk thermal conductivity estimated using the linear extrapolation method [Eq. (B.13)] are plotted in Fig. B.1 as a function of the normalized sample length. Both thermal conductivities converge towards the bulk value as the sample length increases. It is found that $k(l)$ is within 10% of the bulk value for a normalized sample length of $l = 166$, while a normalized sample length of $l = 36$ is required to obtain the same level of converge when the linear extrapolation procedure is used. Based on this result, the error introduced by truncating Eq. (2.27) after the first-order term is expected to be less than 10% when when $l > 36$, and thus,

$$L_S > \frac{24k_\infty\Omega}{k_{\mathrm{B}}v_{ac}}.$$ (B.14)

135
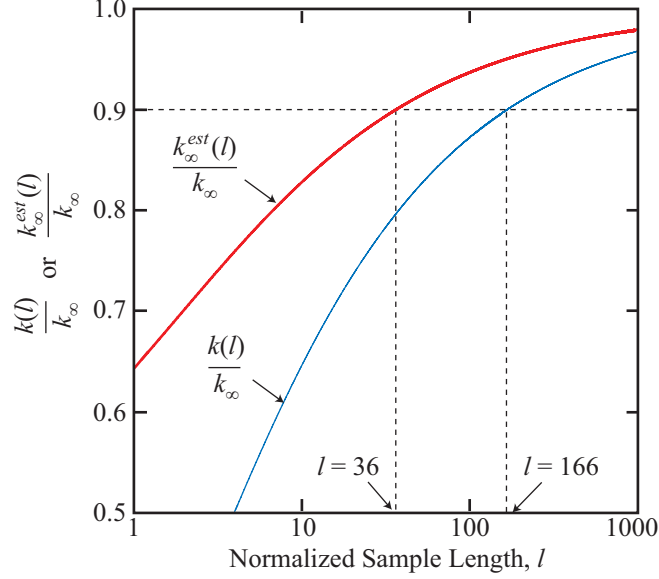
Figure B.1: Length-dependence of the thermal conductivity [Eq. (B.11)] and the bulk thermal conductivity estimated using the linear extrapolation procedure [Eq. (B.13)].

The assumptions underlying Eq. (B.11) are reasonable for single-element crystals with face-centered cubic or diamond lattices (e.g., Ar, Si, and Ge). For example, optical modes contribute less than 10% to the thermal conductivity of SW Si [75] and do not exist in crystals with a monatomic primitive cell such as Ar. The dependence of the phonon-phonon relaxation time on frequency given by Eq. (B.9) is in good agreement with anharmonic LD-predicted relaxation times for SW Si and SW Ge for phonons with frequencies less than 10-20 rad/ps [75].

BIBLIOGRAPHY

BIBLIOGRAPHY

[1] D. Roberts and G. Triplett. Tuning nonlinear susceptibility in strained AlGaAs/InGaAs quantum cascade lasers. *Solid-State Electronics*, 52:1669–1673, 2008.

[2] Y.-L. Li, Y.-R. Huang, and Y.-H. Lai. Efficiency droop behaviors of InGaN/GaN multiple-quantum-well light-emitting diodes with varying quantum well thickness. *Applied Physics Letters*, 91:181113, 2007.

[3] M. Wienold, M. P. Semtsiv, I. Bayrakli, W. T. Masselink, M. Ziegler, K. Kennedy, and R. Hogg. Optical and thermal characteristics of narrow-ridge quantum-cascade lasers. *Journal of Applied Physics*, 103:083113, 2008.

[4] S. Lombardo, J. H. Stathis, B. P. Linder, K. L. Pey, F. Palumbo, and C. H. Tung. Dielectric breakdown mechanisms in gate oxides. *Journal of Applied Physics*, 98:121301, 2005.

[5] D. G. Cahill, W. K. Ford, K. E. Goodson, G. D. Mahan, A. Mujumdar, H. J. Maris, R. Merlin, and S. R. Phillpot. Nanoscale thermal transport. *Journal of Applied Physics*, 93:793–818, 2003.

[6] International Technology Roadmap for Semiconductors, ITRS, 2008, update, http://www.itrs.net.

[7] Y. S. Ju and K. E. Goodson. Phonon scattering in silicon films with thicknesses of order 100 nm. *Applied Physics Letters*, 74:3005–3007, 1999.

[8] M. S. Love and A. C. Anderson. Estimate of phonon thermal transport in amorphous materials above 50 K. *Physical Review B*, 42:1845–1847, 1990.

[9] E. T. Swartz and R. O. Pohl. Thermal boundary resistance. *Review of Modern Physics*, 61:605–668, 1989.

[10] R. A. Escobar and C. H. Amon. Infuence of phonon dispersion on transient thermal response of silicon-on-insulator transistors under self-heating conditions. *Journal of Heat Transfer*, 129:790–797, 2007.

[11] N. Vichare, P. Rodgers, V. Eveloy, and M. G. Pecht. *In Situ* temperature measurement of a notebook computer - a case study in health and usage monitoring of electronics. *Proceedings of IEEE Transactions on Device and Materials Reliability*, 4:658–663, 2004.

[12] J. P. Reifenberg, D. L. Kencke, and K. E. Goodson. The impact of thermal boundary resistance in phase-change memory devices. *IEEE Electron Device Letters*, 2008:1112–1114, 2008.

[13] D. B. Aubertine and P. C. McIntyre. Influence of Ge concentration and compressive biaxial stress on interdiffusion in Si-rich SiGe alloy heterostructures. *Journal of Applied Physics*, 97:013531, 2005.

[14] G. Chen, M. S. Dresselhaus, G. Dresselhaus, J.-P. Fleurial, and T. Caillat. Recent developments in thermoelectric materials. *International Materials Review*, 48:45–66, 2003.

[15] H. Bottner, G. Chen, and R. Venkatasubramanian. Aspects of thin-film superlattice thermo-electric materials, devices, and applications. *MRS Bulletin*, 31:211–216, 2006.

[16] M. S. Dresselhaus, G. Chen, M. Y. Tang, R. G. Yang, H. Lee, D. Z. Wang, Z. F. Ren, J.-P. Fleurial, and P. Gogna. New directions for low-dimensional thermoelectric materials. *Advanced Materials*, 19:1043–1053, 2007.

[17] C. Wood. Materials for thermoelectric energy conversion. *Reports on Progress in Physics*, 51:459–539, 1988.

[18] A. J. Minnich, M. S. Dresselhaus, Z. F. Ren, and G. Chen. Bulk nanostructured thermoelectric materials: current research and future prospects. *Energy and Environmental Science*, 2:466–479, 2009.

[19] J. P. Dismukes, L. Ekstrom, E. F. Steigmeier, I. Kudman, and D. S. Beers. Thermal and electrical properties of heavily doped Ge-Si alloys up to 1300 K. *Journal of Applied Physics*, 35:2899–2907, 1964.

[20] F. J. DiSalvo. Thermoelectric cooling and power generation. *Science*, 285:703–706, 1999.

[21] R. Venkatasubramanian, E. Sivola, T. Colpitts, and B. O'Brien. Thin-film thermoelectric devices with high room-temperature figures of merit. *Nature*, 413:597–602, 2001.

[22] D. Kraemer, L. Hu, A. Muto, X. Chen, G. Chen, and M. Chiesa. Photovoltaic-thermoelectric hybrid systems: A general optimization methodology. *Applied Physics Letters*, 92:243503, 2008.

[23] J. Yang. Potential applications of thermoelectric waste heat recovery in the automotive industry. In *Proceedings of the 2005 International Conference on Thermoelectrics*. IEEE, 2005.

[24] G. W. Crabtree and N. S. Lewis. Solar energy conversion. *Physics Today*, March 2007:37–42, 2007.

[25] A. I. Hochbaum, R. Chen, R. D. Delgado, W. Liang, E. C. Garnett, M. Najarian, A. Majumdar, and P. Yang. Enhanced thermoelectric performance of rough silicon nanowires. *Nature*, 451:163–163, 2008.

[26] E. S. Landry and A. J. H. McGaughey. Thermal boundary resistance predictions from molecular dynamics simulations and theoretical calculations. *Physical Review B*, 80:165304, 2009.

[27] E. S. Landry and A. J. H. McGaughey. Effect of film thickness on the thermal resistance of confined semiconductor thin films. To appear in *Journal of Applied Physics*, 2009.

[28] E. S. Landry and A. J. H. McGaughey. Effect of interfacial species mixing on phonon transport in semiconductor superlattices. *Physical Review B*, 79:075316, 2009.

[29] E. S. Landry, M. I. Hussein, and A. J. H. McGaughey. Complex superlattice unit cell designs for reduced thermal conductivity. *Physical Review B*, 77:184302, 2008.

[30] P. K. Schelling, S. R. Phillpot, and P. Keblinski. Comparison of atomic-level simulation methods for computing thermal conductivity. *Physical Review B*, 65:144306, 2002.

[31] Y. Chen, D. Li, J. R. Lukes, Z. Ni, and M. Chen. Minimum superlattice thermal conductivity from molecular dynamics. *Physical Review B*, 72:174302, 2005.

[32] J. R. Lukes, D. Y. Li, X.-G. Liang, and C.-L. Tien. Molecular dynamics study of solid thin-film thermal conductivity. *Journal of Heat Transfer*, 122:536–543, 2000.

[33] K. Kang and W. Cai. Brittle and ductile fracture of semiconductor nanowires - molecular dynamics simulations. *Philosophical Magazine*, 87:11–21, 2007.

[34] M. Klein and W. Shinoda. Large-scale molecular dynamics simulations of self-assembling systems. *Science*, 321:798–800, 2008.

[35] E. S. Landry, S. Mikkilineni, M. Paharia, and A. J. H. McGaughey. Droplet evaporation: A molecular dynamics investigation. *Journal of Applied Physics*, 102:124301, 2007.

[36] N. de Koker. Thermal conductivity of MgO periclase from equilibrium first principles molecular dynamics. *Physical Review Letters*, 103:125902, 2009.

[37] D. A. Broido, M. Malorny, G. Birner, and N. Mingo. Intrinsic lattice thermal conductivity of semiconductors from first principles. *Applied Physics Letters*, 91:231922, 2007.

[38] J. M. Ziman. *Electrons and Phonons*. Oxford University Press, New York, 2001.

[39] Y. H. Lee, R. Biswas, C. M. Soukoulis, C. Z. Wang, C. T. Chan, and K. M. Ho. Molecular-dynamics simulation of thermal conductivity in amorphous silicon. *Physical Review B*, 43:6573–6580, 1991.

[40] S. Volz, J. B. Saulnier, G. Chen, and P. Beauchamp. Computation of thermal conductivity of Si/Ge superlattices by molecular dynamics techniques. *Microelectronics Journal*, 31:815–819, 2000.

[41] Y. L. Li, L. Porter, and S. Yip. Atomistic modeling of finite-temperature properties of crystalline β-SiC: II. Thermal conductivity and effects of point defects. *Journal of Nuclear Materials*, 255:139–152, 1998.

[42] J. R. Lukes and H. Zhong. Thermal conductivity of individual single-wall carbon nanotubes. *Journal of Heat Transfer*, 129:705, 2007.

[43] J. E. Turney, E. S. Landry, A. J. H. McGaughey, and C. H. Amon. Predicting phonon properties and thermal conductivity from anharmonic lattice dynamics calculations and molecular dynamics simulations. *Physical Review B*, 79:064301, 2009.

[44] M. P. Allen and D. J. Tildesley. *Computer Simulation of Liquids*. Oxford Science Publications, Oxford, 1987.

[45] R. P. Feynman. Forces in molecules. *Physical Review*, 56:340–343, 1939.

[46] D. Frenkel and B. Smit. *Understanding Molecular Simulation: From Algorithms to Applications*. Academic Press, San Diego, 2002.

[47] H. J. C. Berendsen, J. P. M. Postma, W. F. van Gunsteren, A. DiNola, and J. R. Haak. Molecular dynamics with coupling to an external bath. *Journal of Chemical Physics*, 81:3684, 1984.

[48] F. H. Stillinger and T. A. Weber. Computer simulation of local order in condensed phases of silicon. *Physical Review B*, 31:5262–5271, 1985.

[49] K. Ding and H. C. Andersen. Molecular-dynamics simulation of amorphous germanium. *Physical Review B*, 34:6987–6991, 1986.

[50] M. Laradji, D. P. Landau, and B. Dunweg. Structural properties of $Si_{1-x}Ge_x$ alloys: A Monte Carlo simulation with the Stillinger-Weber potential. *Physical Review B*, 51:4894–4902, 1995.

[51] C. Kittel. *Introduction to Solid State Physics*. Wiley, New York, 1996.

[52] N. W. Ashcroft and N. D. Mermin. *Solid State Physics*. Sauders College Publishing, Fort Worth, 1976.

[53] H. Zhao and J. B. Freund. Lattice-dynamical calculation of phonon scattering at ideal Si-Ge interfaces. *Journal of Applied Physics*, 97:024903, 2005.

[54] P. K. Schelling and S. R. Phillpot. Multiscale simulation of phonon transport in superlattices. *Journal of Applied Physics*, 93:5377–5387, 2003.

[55] A. Bodapati, P. K. Schelling, S. R. Phillpot, and P. Keblinski. Vibrations and thermal transport in nanocrystalline silicon. *Physical Review B*, 74:245207, 2006.

[56] B. Becker, P. K. Schelling, and S. R. Phillpot. Interfacial phonon scattering in semiconductor nanowires by molecular-dynamics simulation. *Journal of Applied Physics*, 99:123715, 2006.

[57] L. J. Porter, J. F. Justo, and S. Yip. The importance of Grüneisen parameters in developing interatomic potentials. *Journal of Applied Physics*, 82:5378–5381, 1997.

[58] D. A. McQuarrie. *Statistical Mechanics*. University Science Books, Sausalito, 2000.

[59] A. J. H. McGaughey and M. Kaviany. Phonon transport in molecular dynamics simulations: Formulation and thermal conductivity prediction. In G. A. Greene, Y. I. Cho, J. P. Hartnett, and A. Bar-Cohen, editors, *Advances in Heat Transfer, Volume 39*, pages 169–255. Elsevier, 2006.

[60] A. J. C. Ladd, B. Moran, and W. G. Hoover. Lattice thermal conductivity: A comparison of molecular dynamics and anharmonic lattice dynamics. *Physical Review B*, 34:5058, 1986.

[61] J. Li. *Modeling Microstructural Effects on Deformation Resistance and Thermal Conductivity*. Ph.D. Thesis, Massachusetts Institute of Technology, Cambridge, MA, 2000.

[62] J. Che, T. Cagin, W. Deng, and W. A. Goddard III. Thermal conductivity of diamond and related materials from molecular dynamics simulations. *Journal of Chemical Physics*, 113:6888–6900, 2000.

[63] B. L. Huang, A. J. H. McGaughey, and M. Kaviany. Thermal conductivity of metal-organic framework 5 (MOF-5): Part I. Molecular dynamics simulations. *Int. J. Heat Mass Transfer*, 50:393–404, 2007.

[64] J. Dong, O. F. Sankey, and C. W. Myles. Theoretical study of the lattice thermal conductivity in Ge framework semiconductors. *Phys. Rev. Lett.*, 86:2361–2364, 2001.

[65] P. J. D. Lindan and M. J. Gillan. A molecular dynamics study of the thermal conductivity of CaF_2 and UO_2. *J. Phys.: Condens. Matter*, 3:3929–3939, 1991.

[66] A. J. H. McGaughey, M. I. Hussein, E. S. Landry, M. Kaviany, and G. M. Hulbert. Phonon band structure and thermal transport correlation in a layered diatomic crystal. *Physical Review B*, 74:104304, 2006.

[67] A. J. H. McGaughey and M. Kaviany. Thermal conductivity decomposition and analysis using molecular dynamics simulations. Part II. Complex silica structures. *International Journal of Heat and Mass Transfer*, 47:1799–1816, 2004.

[68] Z. Yao, J-S Wang, B. Li, and G-R Liu. Thermal conduction of carbon nanotubes using molecular dynamics. *Phys. Rev. B*, 71:085417, 2005.

[69] Y. Chen. Local stress and heat flux in atomistic systems involving three-body forces. *Journal of Chemical Physics*, 124:054113, 2006.

[70] A. J. H. McGaughey and M. Kaviany. Thermal conductivity decomposition and analysis using molecular dynamics simulations. Part I. Lennard-Jones argon. *International Journal of Heat and Mass Transfer*, 47:1783–1798, 2004.

[71] H. Kaburaki, J. Li, S. Yip, and H. Kimizuka. Dynamical thermal conductivity of argon crystal. *Journal of Applied Physics*, 102:043514, 2007.

[72] F. P. Incropera and D. P. DeWitt. *Fundamentals of Heat and Mass Transfer*. John Wiley and Sons, Inc., Hoboken, NJ, 2002.

[73] Y. Chen, D. Li, J. Yang, Y. Wu, J. R. Lukes, and A. Majumdar. Molecular dynamics study of the lattice thermal conductivity of Kr/Ar superlattice nanowires. *Physica B*, 349:270–280, 2004.

[74] T. Ikeshoji and B. Hafskjold. Non-equilibrium molecular dynamics calculation of heat conduction in liquid and through liquid-gas interface. *Molecular Physics*, 81:251–261, 1994.

[75] This calculation is performed using anharmonic LD-predicted phonon relaxation times provided by Joseph Turney (Carnegie Mellon) using the methodology described in Refs. [43] and [89].

[76] B. Ni, T. Watanabe, and S. R. Phillpot. Thermal transport in polyethylene and at polyethylene-diamond interfaces investigated using molecular dynamics simulation. *Journal of Physics: Condensed Matter*, 21:084219, 2009.

[77] S.-C. Wang, X.-G. Liang, X.-H. Xu, and T. Ohara. Thermal conductivity of silicon nanowire by nonequilibrium molecular dynamics simulations. *Journal of Applied Physics*, 105:014316, 2009.

[78] N. Papanikolaou. Lattice thermal conductivity of SiC nanowires. *Journal of Physics: Condensed Matter*, 20:135201, 2008.

[79] G. P. Srivastava. *The Physics of Phonons*. Adam Hilger, Bristol, 1990.

[80] A. J. H. McGaughey. *Phonon Transport in Molecular Dynamics Simulations: Formulation and Thermal Conductivity Prediction*. Ph.D. Thesis, University of Michigan, Ann Arbor, MI, 2004.

[81] D. J. Quesnel, D. S. Rimai, and L. P. DeMejo. Elastic compliances and stiffnesses of the fcc Lennard-Jones solid. *Physical Review B*, 48:6795–6807, 1993.

[82] E. R. Cowley. Lattice dynamics of silicon with empirical many-body potentials. *Physical Review Letters*, 60:2379–2381, 1988.

[83] W. Kim, R. Wang, and A. Majumdar. Nanostructuring expands thermal limits. *Nano Today*, 2:40–47, 2007.

[84] X. W. Zhou, S. Aubry, R. E. Jones, A. Greenstein, and P. K. Schelling. Towards more accurate molecular dynamics calculation of thermal conductivity: Case study of GaN bulk crystals. *Physical Review B*, 79:115201, 2009.

[85] J. Shiomi and S. Maruyama. Diffusive-ballistic heat conduction of carbon nanotubes and nanographene ribbons. *International Journal of Thermophysics*, 2008.

[86] P. K. Schelling, S. R. Phillpot, and P. Keblinski. Phonon wave-packet dynamics at semiconductor interfaces by molecular-dynamics simulations. *Applied Physics Letters*, 80:2484, 2002.

[87] A. J. H. McGaughey and M. Kaviany. Quantitative validation of the Boltzmann transport equation phonon thermal conductivity model under the single-mode relaxation time approximation. *Physical Review B*, 69:094303, 2004.

[88] M. T. Dove. *Introduction to Lattice Dynamics*. Cambridge University Press, Cambridge, 1993.

[89] J. E. Turney, A. J. H. McGaughey, and C. H. Amon. Assessing the applicability of quantum corrections to classical thermal conductivity predictions. *Physical Review B*, 79:224305, 2009.

[90] P. Giannozzi, S. de Gironcoli, P. Pavone, and S. Baroni. *Ab initio* calculation of phonon dispersions in semiconductors. *Physical Review B*, 43:7231–7242, 1991.

[91] G. Nilsson and G. Nelin. Phonon dispersion relations in Ge at 80 K. *Physical Review B*, 3:364–369, 1971.

[92] J.-S. Wang, J. Wang, and J. T. Lu. Quantum thermal transport in nanostructures. *European Physical Journal B*, 62:381–404, 2008.

[93] J. Wang and J.-S. Wang. Mode-dependent energy transmission across nanotube junctions calculated with a lattice dynamics approach. *Physical Review B*, 74:054303, 2006.

[94] J. Wang and J.-S. Wang. Characteristics of phonon transmission across epitaxial interfaces: a lattice dynamics study. *Journal of Physics: Condensed Matter*, 19:236211, 2007.

[95] S. Pettersson and G. D. Mahan. Theory of the thermal boundary resistance between dissimilar lattices. *Physical Review B*, 42:7386–7390, 1990.

[96] W. A. Little. The transport of heat between dissimilar solids at low temperatures. *Canadian Journal of Physics*, 37:334–349, 1959.

[97] R. J. Stoner and H. J. Maris. Kapitza conductance and heat flow between solids at temperatures from 50 to 300 K. *Physical Review B*, 48:16373–16387, 1993.

[98] A. Majumdar and P. Reddy. Role of electron-phonon coupling in thermal conductance of metal-nonmetal interfaces. *Applied Physics Letters*, 84:4768–4770, 2004.

[99] H.-K Lyeo and D. G. Cahill. Thermal conductance of interfaces between highly dissimilar materials. *Physical Review B*, 73:144301, 2006.

[100] M. L. Huberman and A. W. Overhauser. Electronic Kapitza conductance at a diamond-Pb interface. *Physical Review B*, 50:2865–2873, 1994.

[101] A. V. Sergeev. Electronic Kapitza conductance due to inelastic electron-boundary scattering. *Physical Review B*, 58:R10199–R10202, 1998.

[102] G. D. Mahan. Kapitza thermal resistance between a metal and a nonmetal. *Physical Review B*, 79:075408, 2009.

[103] T. Beechem, S. Graham, P. Hopkins, and P. Norris. Role of interface disorder on the thermal boundary conductance using a virtual crystal approach. *Applied Physics Letters*, 90:054104, 2007.

[104] P. E. Hopkins, P. M. Norris, R. J. Stevens, T. E. Beechem, and S. Graham. Influence of interfacial mixing on thermal boundary conductance across a chromium/silicon interface. *Journal of Heat Transfer*, 130:062402, 2008.

[105] P. E. Hopkins, P. M. Norris, and R. J. Stevens. Influence of inelastic scattering at metal-dielectric interfaces. *Journal of Heat Transfer*, 130:022401, 2008.

[106] P. E. Hopkins and P. M. Norris. Relative contributions of inelastic and elastic diffuse phonon scattering to thermal boundary conductance across solid interfaces. *Journal of Heat Transfer*, 131:022402, 2009.

[107] R. S. Prasher and P. E. Phelan. A scattering-mediated acoustic mismatch model for the prediction of thermal boundary resistance. *Journal of Heat Transfer*, 123:105–112, 2001.

[108] R. M. Costescu, M. A. Wall, and D. G. Cahill. Thermal conductance of epitaxial interfaces. *Physical Review B*, 67:054302, 2003.

[109] R. J. Stevens, A. N. Smith, and P. M. Norris. Measurment of thermal boundary conductance of a series of metal-dielectric interfaces by the transient thermoreflectance technique. *Journal of Heat Transfer*, 127:315–322, 2005.

[110] P. Reddy, K. Castelino, and A. Majumdar. Diffuse mismatch model of thermal boundary conductance using exact phonon dispersion. *Applied Physics Letters*, 2005:211908, 2005.

[111] N. S. Snyder. Heat transport through helium II: Kapitza conductance. *Cryogenics*, 10:89, 1970.

[112] R. J. Stoner, H. J. Maris, T. R. Anthony, and W. F. Banholzer. Measurements of the Kapitza conductance between diamond and several metals. *Physical Review Letters*, 68:1563–1566, 1992.

[113] P. E. Hopkins. Multiple phonon processes contributing to inelastic scattering during thermal boundary conductance at solid interfaces. *Journal of Applied Physics*, 106:013528, 2009.

[114] L. G. C. Rego and G. Kirczenow. Quantized thermal conductance of dielectric quantum wires. *Physical Review Letters*, 1998:232–235, 1998.

[115] N. Mingo and D. A. Broido. Carbon nanotube ballistic thermal conductance and its limits. *Physical Review Letters*, 95:096105, 2005.

[116] C. Kimmer, S. Aubry, A. Skye, and P. K. Schelling. Scattering of phonons from a high-energy grain boundary in silicon: Dependence on angle of incidence. *Physical Review B*, 75:144105, 2007.

[117] S. Aubry, C. J. Kimmer, A. Skye, and P. K. Schelling. Comparison of theoretical and simulation-based predictions of grain-boundary Kapitza conductance in silicon. *Physical Review B*, 78:064112, 2008.

[118] G. Chen. Thermal conductivity and ballistic-phonon transport in the cross-plane direction of superlattices. *Physical Review B*, 57:14958–14973, 1998.

[119] D. A. Young and H. J. Maris. Lattice-dynamical calculation of the Kapitza resistance between fcc lattices. *Physical Review B*, 40:3685, 1989.

[120] S. Simons. On the thermal contact resistance between insulators. *Journal of Physics C: Solid State Physics*, 7:4048–4052, 1974.

[121] G. Chen. Diffusion-transmission interface condition for electron and phonon transport. *Applied Physics Letters*, 82:991–993, 2003.

[122] www.gnu.org/software/gsl/.

[123] J. Callaway. Model for lattice thermal conductivity at low temperatures. *Physical Review*, 113:1046–1051, 1959.

[124] G. Theodorou. The Si/Ge interface: structure, energy and interdiffusion. In E. Kasper and K. Lyutovich, editors, *Properties of Silicon Germanium and SiGe:Carbon*, pages 91–93. IN-SPEC, The Institution of Electrical Engineers, 2000.

[125] T. Borca-Tasciuc, W. Liu, J. Liu, T. Zeng, D. W. Song, C. D. Moore, G. Chen, K. L. Wang, M. S. Goorsky, T. Radetic, R. Gronsky, T. Koga, and M. S. Dresselhaus. Thermal conductivity of symmetrically strained Si/Ge superlattices. *Superlattices and Microstructures*, 28:199–206, 2000.

[126] R. J. Stevens, L. V. Zhigilei, and P. M. Norris. Effects of temperature and disorder on thermal boundary conductance at solid-solid interfaces: Nonequilibrium molecular dynamics simulations. *International Journal of Heat and Mass Transfer*, 50:3977–3989, 2007.

[127] J. C. Lambropoulos, M. R. Jolly, C. A. Amsden, S. E. Gilman, M. J. Sinicropi, D. Diakomihalis, and S. D. Jacobs. Thermal conductivity of dielectric thin films. *Journal of Applied Physics*, 66:4230–4242, 1989.

[128] M. Asheghi, M. N. Touzelbaev, K. E. Goodson, Y. K. Leung, and S. S. Wong. Temperature-dependent thermal conductivity of single-crystal silicon layers in SOI substrates. *Journal of Heat Transfer*, 120:30–36, 1998.

[129] A. D. McConnell and K. E. Goodson. Thermal conduction in silicon micro- and nanostructures. *Annual Review of Heat Transfer*, 14:129–168, 2005.

[130] G. Chen and T. Zeng. Nonequilibrium phonon and electron transport in heterostructures and superlattices. *Microscale Thermophysical Engineering*, 5:71–78, 2001.

[131] C. V. D. R. Anderson and K. K. Tamma. An overview of advances in heat conduction models and approaches for prediction of thermal conductivity in thin dielectric films. *International Journal of Numerical Methods for Heat and Fluid Flow*, 14:12–65, 2004.

[132] J. Zou, X. Lange, and C. Richardson. Lattice thermal conductivity of nanoscale AlN/GaN/AlN heterostructures: Effects of partial phonon spatial confinement. *Journal of Applied Physics*, 100:104309, 2006.

[133] X. Lu and J. Chu. Lattice thermal conductivity in a Si/Ge/Si heterostructure. *Journal of Applied Physics*, 101:114323, 2007.

[134] P. Chantrenne and J. L. Barrat. Finite size effects in determination of thermal conductivities: Comparing molecular dynamics results with simple models. *Journal of Heat Transfer*, 126:577–585, 2004.

[135] X. L. Feng. Molecular dynamics simulation of thermal conductivity of nanoscale thin silicon films. *Nanoscale and Microscale Thermophysical Engineering*, 7:153–161, 2003.

[136] Z. Huang, Z. Tang, J. Yu, and S. Bai. Thermal conductivity of amorphous and crystalline thin films by molecular dynamics simulations. *Physica B*, 404:1790–1793, 2009.

[137] Z. Tang and N. R. Aluru. Calculation of thermodynamic and mechanical properties of silicon nanostructures using the local phonon density of states. *Physical Review B*, 74:235441, 2006.

[138] D. P. Sellan, J. E. Turney, A. J. H. McGaughey, and C. H. Amon. In preparation.

[139] R. A. Escobar, S. S. Ghai, M. S. Jhon, and C. H. Amon. Multi-length and time scale thermal transport using the lattice Boltzmann method with application to electronics cooling. *International Journal of Heat and Mass Transfer*, 49:97–107, 2006.

[140] G. Chen. Particularities of heat conduction in nanostructures. *Journal of Nanoparticle Research*, 2:199–204, 2000.

[141] W. S. Capinski, H. J. Maris, T. Ruf, M. Cardona, K. Ploog, and D. S. Katzer. Thermal-conductivity measurements of GaAs/AlAs superlattices using a picosecond optical pump-and-probe technique. *Physical Review B*, 59:8105–8113, 1999.

[142] S. Chakraborty, C. A. Kleint, A. Heinrich, C. M. Schneider, and J. Schumann. Thermal conductivity in strain symmetrized Si/Ge superlattices on Si(111). *Applied Physics Letters*, 83:4184–4186, 2003.

[143] J. C. Caylor, K. Coonley, J. Stuart, T. Colpitts, and R. Venkatasubramanian. Enhanced thermoelectric performance in PbTe-based superlattice structures from reduction of lattice thermal conductivity. *Appl. Phys. Lett.*, 87:023105, 2005.

[144] Y. Ezzahri, S. Dilhaire, S. Grauby, J. M. Rampnoux, W. Claeys, Y. Zhang, G. Zeng, and A. Shakouri. Study of thermomechanical properties of Si/SiGe superlattices using femtosecond transient thermoreflectance technique. *Applied Physics Letters*, 87:103506, 2005.

[145] T. Borca-Tasciuc, D. W. Song, J. R. Meyer, I. Vurgaftman, M. J. Yang, B. Z. Nosho, L. J. Whitman, H. Lee, R. U. Martinelli, G. W. Turner, M. J. Manfra, and G. Chen. Thermal conductivity of $AlAs_{0.07}Sb_{0.93}$ and $Al_{0.9}Ga_{0.1}As_{0.07}Sb_{0.93}$ alloys and $(AlAs)_1/(AlSb)_{11}$ digital-alloy superlattices. *Journal of Applied Physics*, 92:4994–4998, 2002.

[146] S. T. Huxtable, A. R. Abramson, C.-L. Tien, A. Majumdar, C. LaBounty, X. Fan, G. Zeng, J. E. Bowers, A. Shakouri, and E. T. Croke. Thermal conductivity of Si/SiGe and SiGe/SiGe superlattices. *Applied Physics Letters*, 80:1737–1739, 2002.

[147] S. T. Huxtable. *Heat Transport in Superlattices and Nanowire Arrays*. Ph.D. Thesis, University of California, Berkeley, Berkeley, CA, 2002.

[148] R. Venkatasubramanian. Lattice thermal conductivity reduction and phonon localization behavior in superlattice structures. *Physical Review B*, 61:3091–3097, 2000.

[149] T. Yao. Thermal properties of AlAs/GaAs superlattices. *Applied Physics Letters*, 51:1798–1800, 1987.

[150] S. M. Lee, D. G. Cahill, and R. Venkatasubramanian. Thermal conductivity of Si-Ge superlattices. *Applied Physics Letters*, 70:2957–2959, 1997.

[151] M. N. Touzelbaev, P. Zhou, R. Venkatasubramanian, and K. E. Goodson. Thermal characterization of Bi_2Te_3/Sb_2Te_3 superlattices. *Journal of Applied Physics*, 90:763–767, 2001.

[152] J.-Y. Duquesne. Thermal conductivity of semiconductor superlattices: Experimental study of interface scattering. *Physical Review B*, 79:153304, 2009.

[153] Y. K. Koh, Y. Cao, D. G. Cahill, and D. Jena. Heat transport mechanisms in superlattices. *Advanced Functional Materials*, 19:610–615, 2009.

[154] Z. Chen, J. Yang, P. Zhuang, M. Chen, J. Zhu, and Y. Chen. Thermal conductivity measurement of InGaAs/InGaAsP superlattice thin films. *Chinese Science Bulletin*, 51:2931–2936, 2009.

[155] C.-K. Liu, C.-K. Yu, H.-C. Chien, S.-L. Kuo, C.-Y. Hsu, M.-J. Dai, G.-L. Luo, S.-C. Huang, and M.-J. Huang. Thermal conductivity of Si/SiGe superlattice films. *Journal of Applied Physics*, 104:114301, 2008.

[156] W. Kim, J. Zide, A. Gossard, D. Klenov, S. Stemmer, A. Shakouri, and A. Majumdar. Thermal conductivity reduction and thermoelectric figure of merit increase by embedding nanoparticles in crystalline seminconductors. *Physical Review Letters*, 96:045901, 2006.

[157] G. Chen and M. Neagu. Thermal conductivity and heat transfer in superlattices. *Applied Physics Letters*, 71:2761–2763, 1997.

[158] A. Pattamatta and C. K. Madnia. Modeling heat transfer in Bi_2Te_3-Sb_2Te_3 nanostructures. *International Journal of Heat and Mass Transfer*, 52:860–869, 2009.

[159] D. A. Broido and T. L. Reinecke. Lattice thermal conductivity of superlattice structures. *Physical Review B*, 70:081310, 2004.

[160] S. F. Ren, W. Cheng, and G. Chen. Lattice dynamics investigations of phonon thermal conductivity of Si/Ge superlattices with rough interfaces. *Journal of Applied Physics*, 100:103505, 2006.

[161] S. Tamura, Y. Tanaka, and H. J. Maris. Phonon group velocity and thermal conduction in superlattices. *Physical Review B*, 60:2627–2630, 1999.

[162] B. Yang and G. Chen. Lattice dynamics study of anisotropric heat conduction in superlattices. *Microscale Thermophysical Engineering*, 5:107–116, 2001.

[163] P. Hyldgaard and G. D. Mahan. Phonon superlattice transport. *Physical Review B*, 56:10754–10757, 1997.

[164] A. A. Kiselev, K. W. Kim, and M. A. Stroscio. Thermal conductivity of Si/Ge superlattices: A realistic model with a diatomic unit cell. *Physical Review B*, 62:6896–6899, 2000.

[165] M. V. Simkin and G. D. Mahan. Minimum thermal conductivity of superlattices. *Physical Review Letters*, 84:927–930, 2000.

[166] B. Yang and G. Chen. Partially coherent phonon heat conduction in superlattices. *Physical Review B*, 67:195311, 2003.

[167] W. E. Bies, R. J. Radtke, and H. Ehrenreich. Phonon dispersion effects and the thermal conductivity reduction in GaAs/AlAs superlattices. *Journal of Applied Physics*, 88:1498–1503, 2000.

[168] A. Ward and D. A. Broido. Intrinsic lattice thermal conductivity of Si/Ge and GaAs/AlAs superlattices. *Physical Review B*, 77:245328, 2008.

[169] B. C. Daly, H. J. Maris, K. Imamura, and S. Tamura. Molecular dynamics calculation of the thermal conductivity of superlattices. *Physical Review B*, 66:024301, 2002.

[170] K. Imamura, Y. Tanaka, N. Nishiguchi, S. Tamura, and H. J. Maris. Lattice thermal conductivity in superlattices: Molecular dynamics calculations with a heat reservoir method. *Journal of Physics: Condensed Matter*, 15:8679–8690, 2003.

[171] A. A. Abramson, C.-L. Tien, and A. Majumdar. Interface and strain effects on the thermal conductivity of heterostructures: A molecular dynamics study. *Journal of Heat Transfer*, 124:963–970, 2002.

[172] S. Srinivasan and R. S. Miller. On parallel nonequilibrium molecular dynamics simulations of heat conduction in heterogeneous materials with three-body potentials: Si/Ge superlattice. *Numerical Heat Transfer, Part B*, 52:297–321, 2007.

[173] V. Samvedi and V. Tomar. Role of heat flow direction, monolayer film thickness, and periodicity in controlling thermal conductivtiy of a Si-Ge superlattice system. *Journal of Applied Physics*, 105:013541, 2009.

[174] D. E. Jesson. Strain-induced morphological evolution of SiGe thin films. In E. Kasper and K. Lyutovich, editors, *Properties of Silicon Germanium and SiGe:Carbon*, pages 91–93. INSPEC, The Institution of Electrical Engineers, 2000.

[175] R. Hull. Equilibrium theories of misfit dislocation networks in the SiGe/Si system. In E. Kasper and K. Lyutovich, editors, *Properties of Silicon Germanium and SiGe:Carbon*, pages 91–93. INSPEC, The Institution of Electrical Engineers, 2000.

[176] D. R. Lide, editor. *CRC Handbook of Chemistry and Physics, Internet Version 2007, (87th Edition), http://www.hbcpnetbase.com*. Taylor and Francis, Boca Raton, FL, 2007.

[177] A. Skye and P. K. Schelling. Thermal resistivity of Si-Ge alloys by molecular-dynamics simulation. *Journal of Applied Physics*, 103:113524, 2008.

[178] Y. Ezzahri, S. Grauby, J. M. Rampnoux, H. Michel, G. Pernot, W. Claeys, S. Dilhaire, C. Rossignol, G. Zeng, and A. Shakouri. Coherent phonons in Si/SiGe superlattices. *Physical Review B*, 75:195309, 2007.

[179] A. S. Henry and G. Chen. Spectral phonon transport properties of silicon based on molecular dynamics simulations and lattice dynamics. *Journal of Computational and Theoretical Nanoscience*, 5:1–12, 2008.

[180] D. G. Cahill, S. K. Watson, and R. O. Pohl. Lower limit to the thermal conductivity of disordered crystals. *Physical Review B*, 46:6131–6140, 1992.

[181] M. G. Holland. Analysis of lattice thermal conductivity. *Physical Review*, 132:2461–2471, 1963.

[182] B. Yang, W. L. Liu, J. L. Liu, K. L. Wang, and G. Chen. Measurements of anisotropic thermoelectric properties in superlattices. *Applied Physics Letters*, 81:3588–3590, 2002.

[183] B. C. Daly, H. J. Maris, Y. Tanaka, and S. Tamura. Molecular dynamics calculation of the in-plane thermal conductivity of GaAs/AlAs superlattices. *Physical Review B*, 67:033308, 2003.

[184] A. Mavrokefalos. In-plane thermal conductivity of disordered layered WSe_2 and $(W)_x(WSe_2)_y$ superlattice films. *Appl. Phys. Lett.*, 91:171912, 2007.

[185] C. Chiritescu, D. G. Cahill, N. Nguyen, D. Johnson, A. Bodapati, P. Keblinski, and P. Zschack. Ultralow thermal conductivity in disordered, layered WSe_2 crystals. *Science*, 315:351–353, 2007.

[186] D. J. Paul. Si/SiGe heterostructures: from material and physics to devices and circuits. *Semiconductor Science and Technology*, 19:R75–R108, 2004.

[187] M. I. Hussein, K. Hamza, G. M. Hulbert, and K. Saitou. Multi-objective evolutionary optimization of periodic layered materials for desired wave dispersion characteristics. *Structural and Multidisciplinary Optimization*, 31:60–75, 2006.

[188] W. Zhang, T. S. Fisher, and N. Mingo. Simulation of interfacial phonon transport in Si-Ge heterostructures using an atomistic Green's function method. *Journal of Heat Transfer*, 129:483, 2007.

[189] N. Mingo. Anharmonic phonon flow through molecular-sized junctions. *Physical Review B*, 74:125402, 2006.